Novel technologies and configurations of superconducting magnets for MRI

TOPICAL REVIEW

Novel technologies and configurations of superconducting magnets for MRI

Yuri Lvovsky[1], Ernst Wolfgang Stautner[2] and Tao Zhang[2,3]

[1] General Electric Healthcare, 3001 West Radio Drive, Florence, SC 29501, USA
[2] General Electric Global Research, Electromagnetics and Superconductivity Lab, One Research Circle, Niskayuna, NY 12309, USA

E-mail: yuri.lvovsky@med.ge.com and stautner@ge.com

Abstract

A review of non-traditional approaches and emerging trends in superconducting magnets for MRI is presented. Novel technologies and concepts have arisen in response to new clinical imaging needs, changes in market cost structure, and the realities of newly developing markets. Among key trends are an increasing emphasis on patient comfort and the need for 'greener' magnets with reduced helium usage. The paper starts with a brief overview of the well-optimized conventional MR magnet technology that presently firmly occupies the dominant position in the imaging market up to 9.4 T. Non-traditional magnet geometries, with an emphasis on openness, are reviewed. The prospects of MgB_2 and high-temperature superconductors for MRI applications are discussed. In many cases the introduction of novel technologies into a cost-conscious commercial market will be stimulated by growing needs for advanced customized procedures, and specialty scanners such as orthopedic or head imagers can lead the way due to the intrinsic advantages in their design. A review of ultrahigh-field MR is presented, including the largest 11.7 T Iseult magnet. Advanced cryogenics approaches with an emphasis on low-volume helium systems, including hermetically sealed self-contained cryostats requiring no user intervention, as well as future non-traditional non-helium cryogenics, are presented.

(Some figures may appear in colour only in the online journal)

Contents

---

[3] Current address: AllTech Medical Systems, Chengdu, People's Republic of China.

1

1. Introduction

Magnetic resonance imaging, MRI, which started with the development of the key imaging principles in the 1970s and quickly expanded from resistive and permanent magnets to the first superconducting imagers in the early 1980s, represents the largest industrial application for superconducting magnets at the beginning of second century of superconductivity. MRI has rapidly become a major imaging tool, both in clinical diagnostics and medical research. The continuous improvements in image quality brought about by technological advances in hardware, including magnets, coupled with novel imaging techniques and MR applications, have yielded an unprecedented non-invasive insight into the structures of soft tissues, functional responses and real-time dynamic images, and enabled radical changes in modern diagnostics and treatment. The continuing global growth of superconducting MR scanners (figure 1) is a testimony to the underlying technological advances that have taken place over the past decades.

The MRI industry has shaped its volume production offerings in response to the needs of the clinical diagnostics market. The highly competitive commercial environment has maintained an emphasis on cost-effective solutions; and key technologies have by now been developed and established by each manufacturer. These well-proven technologies have cost and risk advantages over the more complex novel solutions, and are often selected as a basis for new MRI magnet designs, albeit often incrementally improved or expanded to meet the new challenges set by more stringent requirements.

Many novel ideas are being introduced through research concepts and prototypes, but each new technology or advanced concept has to clear the high threshold of acceptance of a cost-conscious commercial market. That happens when (a) the market trends and priorities change (such as access and feature differentiation in a rapidly globalizing market; or high emphasis on patient comfort due to demographic changes), (b) when the suggested technology enables drastic improvements in cost, performance or scanner utilization (e.g. helium recondensing technology), or (c) when the change in commodities availability and cost creates a long-term impact on the magnet cost structure.

An illustrative example is the rising cost of helium, which is likely to impact future developments of new cryogenic configurations as well as the application of non-NbTi superconductors. During 2009, most helium suppliers announced price increases of 20%–30% in response to continued increased costs of raw material, energy, and distribution. The price of pure helium will continue to increase as production costs, including the price of crude helium, increase and helium reserves are rapidly depleted, as indicated in figures 2(a) and (b). The average cost of liquid helium
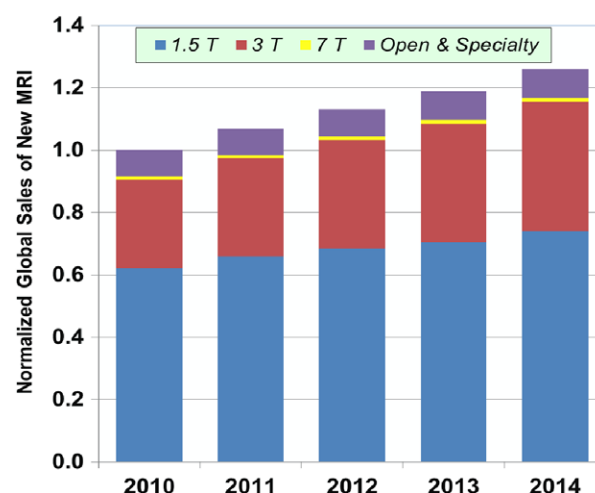

Figure 1. World market sales growth of superconducting MRI scanners relative to 2010 (newly installed per year, includes 2013–4 projections). Data indicate a total growth of ∼25% by 2014, with over 3000 units installed annually.

in North America is currently around $6 l^{-1} and represents the lower end of the price range; Europe with $10 l^{-1} is somewhat in the middle, whereas Latin America and Asia occupy the highest band range of $13–15 l^{-1}. The issue is becoming increasingly important since more MRI units are being shipped to newly emerging markets where liquid helium refills at the customer site are required.

With few exceptions, the superconducting magnets presently used by the MRI industry in clinical and high-field research scanners have horizontal cylindrical cryostats with annular patient bores, and helium vessels with bath-cooled coils that use cost-driven NbTi superconductors. Novel technologies and approaches arise, both within and outside the MR industry, that offer alternatives in each of the three areas: (a) non-traditional magnet topologies; (b) advanced cryogenic solutions, (c) new superconductors. Many of these approaches, with different levels of development, readiness and cost, can be a potential response to changing demands of the diagnostic imaging market.

This paper presents a review of emerging trends and approaches in MRI magnet technology. While the selection of technologies is inevitably influenced by the authors' individual views and experiences, our emphasis has been on novel alternatives, rather than on attempting a crystal ball prediction over which ones will eventually survive the rigorous scrutiny of industry acceptance. The selection of technological trends in this review, however, does not provide a forecast of which future products and applications will appear in accordance with the roadmaps of established and emerging manufacturers. To a large degree, those will be shaped by the mosaic of a competitive MR market. But whatever direction chosen, the emerging novel technologies will serve as critical tools to address the challenges of the ever-changing field of MRI.
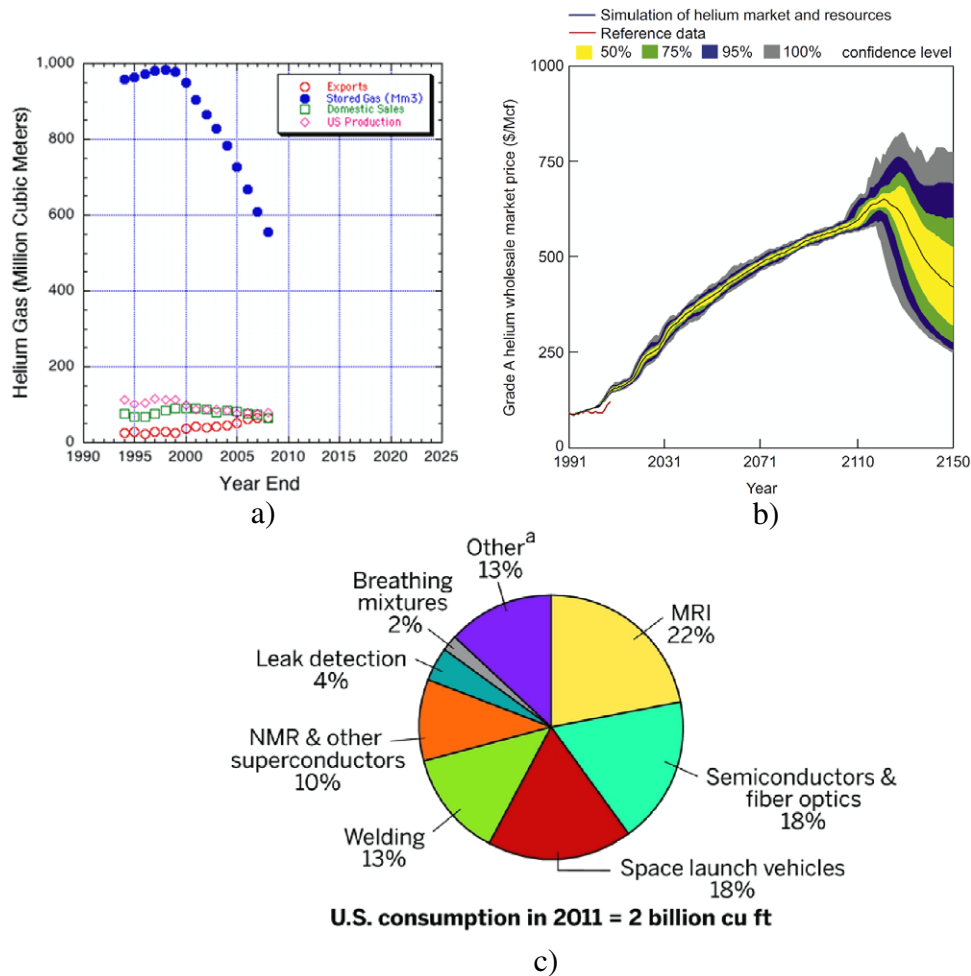
Figure 2. Helium storage, production and consumption. (a) Helium storage and production dynamics (Pfotenhauer 2012). (b) Monte Carlo simulation of the helium wholesale price increase with various confidence levels; price variations are mainly due to production costs and the imbalance between demand and supply (Cai *et al* (2010), Copyright 2010 Elsevier). (c) US helium consumption in 2011; NMR and MRI consume the biggest share of the pie. Reisch (2013) reproduced with permission from C&EN, Copyright 2013 ACS.

2. Mainstream MRI magnets

2.1. Basic cylindrical design—an overview

MR imaging is based on nuclear magnetic resonance (NMR) principles and discerns tissues by the characteristics of the signal emitted by their nuclei (usually protons) in a strong magnetic field when subjected to resonant RF excitation. In the background magnetic field B_0 created by the magnet, protons in the body tissues tend to align with the field, creating a net magnetic moment proportional to B_0. When an RF pulse of resonant frequency is sent by the RF coil located in magnet bore, the magnetized protons absorb energy. The net magnetization vector of the tissue, which is now precessing at the Larmor frequency $\omega_0 = \gamma B_0$, where $\gamma = 2\pi \cdot 42.576$ MHz T^{-1} is the proton gyromagnetic ratio, relaxes back. The relaxation characteristics vary for different tissues, a feature that is used to create image contrast. A receiver coil picks up the resonant signal emitted by the rotating magnetization vector, which is used in image reconstruction. A set of resistive gradient coils is inserted

inside the bore of the superconducting magnet, in order to provide spatial encoding. Three gradient coils X, Y and Z are pulsed intermittently; they superimpose linearly varying fields on the uniform background B_z produced by the magnet, creating linear variations of the resonant frequency ω_0 across the field-of-view (FOV). A fast Fourier transform, FFT, is then used to convert the received RF signal into an image.

Thus, together with the magnet, the RF body coil and the gradient coil assembly represent the three major subsystems that comprise the resonance module of the MR scanner. These three subsystems compete for the same annular space that also provides maximum accommodation and comfort for the patient (figure 3). The need for high-performance gradient and RF subsystems, as well as magnetic shims and covers, translates a patient bore with 60 or 70 cm diameter into a typical warm bore diameter of the main magnet of 85–92 cm.

A conventional cylindrical whole body MRI scanner has a length varying from 1.25 to over 2.0 m; the shorter length challenges and tradeoffs are discussed in section 3.1. There are many conflicting requirements that need to be satisfied in the design of MRI magnets (Lvovsky and Jarvis
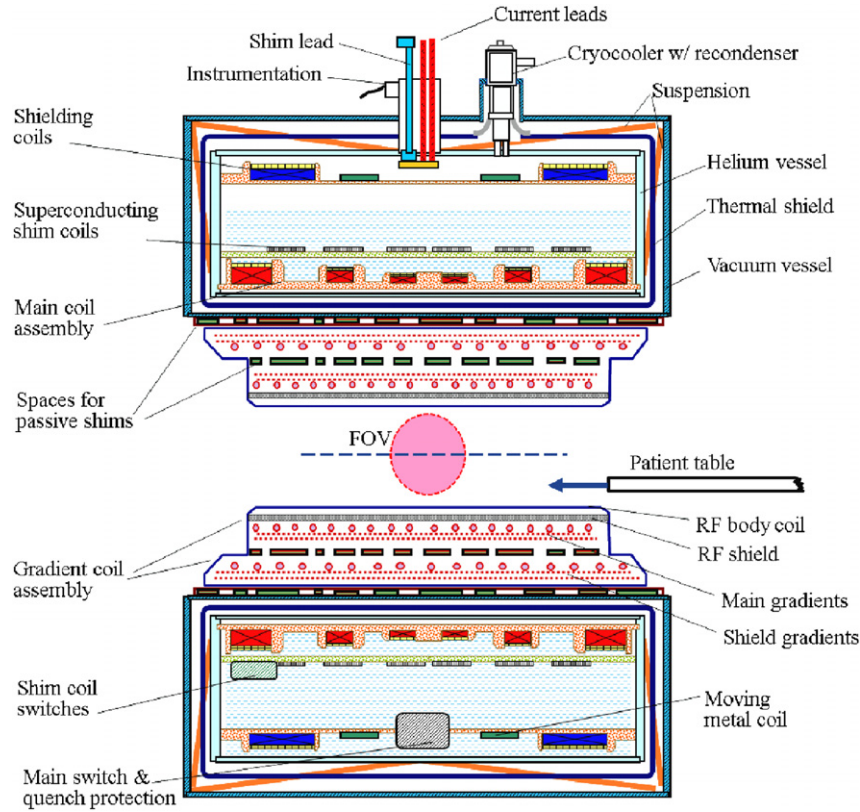
Figure 3. Cross-section of a traditional cylindrical MRI scanner and its components (multi-coil design).

2005). One of the key requirements for a whole body (WB) scanner is stringent homogeneity, typically less than 10 ppm peak-to-peak, which has to be attained over a large volume ∼50 cm DSV (diameter of spherical volume). Poor magnetic field homogeneities interfere with the linear gradient fields generated by the gradient coils and thus distort the position information within the scan volume and degrade the image quality. Among the three different types of magnets (permanent, water-cooled resistive and superconducting), only superconducting magnets present a viable choice for mainstream, whole body MRI scanners with field strengths well above 0.5 T. Typical superconducting MRI magnets are composed of multiple solenoidal coils, the choice mainly driven by the cost and risk advantages of such a design, which allows less usage of conductor, good stress and stability control, together with simplicity and reliability of manufacture.

The distribution of the magnetic field in current-free space can be described by the Laplace equation. With regard to the axial component B_z in question, the Laplace equation takes the form:

$$\nabla^2 B_z = 0. \tag{1}$$

In spherical coordinates (r, θ, φ) shown in figure 4, its solution can be expressed by spherical harmonics

$$B_z = \sum_{n=0}^{\infty} \sum_{m=0}^{n} r^n P_n^m(\cos\theta) \, [A_{n,m}\cos(m\varphi) + B_{n,m}\sin(m\varphi)]$$
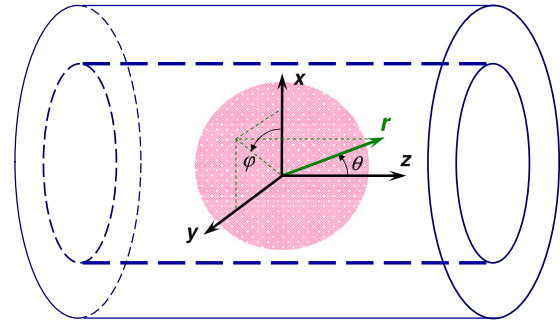
Figure 4. Spherical coordinates used in the harmonics representation of the field of the magnet.

$$+ \sum_{n=0}^{\infty} \sum_{m=0}^{N} \frac{1}{r^{n+1}} \, P_n^m(\cos\theta)$$
$$\times [C_{n,m}\cos(m\varphi) + D_{n,m}\sin(m\varphi)], \tag{2}$$

where P_n^m are associated Legendre polynomials given by

$$P_n^m(u) = (1 - u^2)^{m/2} \frac{(-1)^m}{2^n \cdot n!} \frac{\partial^{n+m}(u^2 - 1)^n}{\partial u^{n+m}}. \tag{3}$$

The first series in (1) represents the magnetic field inside the bore (there $C_{n,m} = D_{n,m} \equiv 0$), while the second series with the singularity at $r \to 0$ describes the fringe field outside the magnet (there $A_{n,m} = B_{n,m} \equiv 0$, and $M_n = C_{n,0}$ represent the external moments of the magnetic system, M_2 being a dipole moment and M_4 a quadrupole moment). For an ideally

aligned axisymmetric set of coils, one has $A_{n,m} \equiv B_{n,m} \equiv C_{n,m} \equiv D_{n,m} \equiv 0$ for $m \neq 0$, so the axial harmonic coefficients $Z_n \equiv A_{n,0}$ are only used with Legendre polynomials of the first kind $P_n \equiv P_n^0$.

The order n represents the zonal harmonics and describes the axial variation of the B_z field, while the degree m represents the tesseral harmonics and describes the variation of the B_z field in what would be the x–y plane in Cartesian coordinates. Equations (2) and (3) provide an important insight into the field homogeneity in terms of different components (harmonics), the formalism that is extensively used in the design and shimming of a high-homogeneity magnet.

Early general guidance was formulated by Williams (1984) regarding the design of an MRI magnet with a homogeneity of the order of 10^{-6} (1 ppm) over 1/3 of the coil bore, with an indication that at least the first eight orders ($n = 8$) must be compensated. In addition, when the coil system is symmetric about the plane $z = 0$, only even orders need be considered. Therefore, in the modern whole body MRI magnet design, with a target peak-to-peak homogeneity $\sim 10^{-5}$ over a maximum imaging FOV of half the ID of the coil, only the zonal harmonics with $n = 2, 4, 6, 8, 10$ are typically compensated. The design of a range of magnets was also detailed by Garrett to compensate the zonal harmonics up to a designated order (Garrett 1951, 1967). For example, a six-coil system would null all harmonic impurities up to $n = 12$. The impact of the number of compensated harmonics on the FOV size and amount of superconductor is illustrated in Lvovsky and Jarvis (2005).

Because of its large dipole moment, an MRI magnet produces a strong fringe field extending several meters from the magnet isocenter. This may adversely affect the electronic equipment, and requires a careful consideration of magnet siting. It may also present a patient safety hazard in the adjacent facilities. Therefore it is now a common approach to shield the magnets to control the fringe field footprint. The criterion established in the competitive MR industry has the 0.5 mT line fully confined within the MR scanning room (typical $Z \times R$ dimensions less than 5 m $\times$ 3 m).

Two available approaches are passive and active magnetic shielding. Passive shielding (iron shield) uses ferromagnetic materials at the cylindrical outer shell of the cryostat. (In certain cases, especially with ultrahigh-field research magnets, passive shielding uses steel plates installed into the scanner room walls, floor or ceiling.) However, the passive approach has several potential disadvantages, such as: (1) the shield is designed for one fixed central field level of the magnet; (2) the proximity of the ferromagnetic material makes the homogeneity susceptible to any asymmetry in the shield or variations in its BH curve; (3) the large amount of iron requires control and compensation of B_z variations caused by temperature fluctuations of iron elements; (4) the iron shield increases the total magnet weight by tens of thousands of pounds (Lee 2001). Active shielding is achieved by incorporating a group of coaxial coils of a larger diameter carrying current in the opposite sense to the main coils. The advantages of this approach include the capability of

a single shield design operating at any intermediate central field level without substantial degradation of homogeneity of shielding effectiveness, since the system retains its linear dependence on coil currents; as well as minimal impact on system weight and size as compared with the passive option and thus an increased flexibility in siting. The active shielding, however, increases the superconductor usage nearly doubling the ampere–meters of conductor (Lvovsky and Jarvis 2005); impacts the complexity of the cryostat design, which now has to accommodate the additional shielding coils (Kalafala 1990); and results in larger magnet dimensions and helium volume, therefore contributing significantly to the overall cost of the magnet.

In theory, the required high-homogeneity MRI coil design can be realized in various multiple configurations, each compensating all the harmonics up to a certain order using different numbers of coil pairs, radial and axial positions of each coil, and turns and layers in the coil. In practice, a tradeoff selection is performed amongst different potential designs. The goal is to select the most optimal solution for the intended product, which, besides the homogeneity and fringe field requirements, is subject to additional constraints and limitations, such as magnet dimensions, amount of superconductor, stress and stability of the windings, etc. To arrive at such a solution, optimization techniques are now generally used by all manufacturers, based on an objective function subject to a set of constraints (examples of such design optimization programs can be found e.g. in (Lee 2001, Kalafala 1990, Ogle and Angelo 1991, Crozier and Doddrell 1997, Kakugawa *et al* 1999, Xu *et al* 2000, Jensen 2002, and others)).

No matter how homogeneous the magnet design, the as-built magnet will invariably deviate from the theoretical homogeneity, coming short of the level required for imaging. This is mainly due to the following variations: (a) manufacturing tolerances of the magnet cartridge introduce errors in coil placement; (b) manufacturing tolerances of the superconducting wire itself; (c) the non-isotropic thermal contraction of coil formers and coil windings during cooldown to helium temperature; (d) the large EM force between the windings causing movement of the coils; (e) errors during the winding process; (f) variation in magnetization if ferromagnetic components or shields are involved in the design. All these factors, to a varying degree of sensitivity, contribute to the as-ramped inhomogeneity of every individual magnet. To compensate these unwanted harmonic errors, a magnetic shimming system is included as an integral part of the magnet design.

A passive shimming system uses a set of ferromagnetic pieces strategically distributed on a set of shim trays which are inserted in positions (slots) reserved either on the magnet bore or inside the gradient assembly, thus to a certain degree competing for the radial space with other components of the scanner.

An active magnet shimming system (separate from the low-strength resistive coils for limited patient-specific shimming that may be present inside some gradient coils) relies on a set of dedicated superconducting coils located

inside the magnet. They are designed for a sufficient compensating harmonic strength, in the form of an array of arcs/racetracks with varying azimuthal extent and symmetry and various positions and extents along the Z-axis, and produce a set of associated Legendre functions with predefined n and m as per (2)–(3). The magnitude of the generated harmonics is controlled by the current; typically in excess of ten coils would be built into a separate assembly, with superconducting persistent switches needed to activate and control individual coils, adding significantly to the cost and complexity of the magnet. The advantage of the active shimming approach is its high current-driven capacity. It successfully accommodates large tolerances in the magnet build, whilst avoiding the challenge of excessive mass and force of the passive shim system. However, with an active correction coil assembly located outside the main coils, i.e. far from the FOV, their effectiveness for high-order harmonics ($n \geq 6$) is limited. For that reason, the active shimming system is usually still complemented by a set of passive shims dedicated to high-order harmonics (so-called hybrid shimming system), albeit with a now much reduced ferromagnetic shim mass.

In shimming, and in the other areas of the highly competitive superconducting MRI magnet design, the challenges have been resolved by different manufacturers using different approaches to arrive at products with the stringent performance and quality requirements dictated by its healthcare use (Morrow 2000, Lvovsky and Jarvis 2005, Parizh and Cosmus 2011).

2.2. Multi-coil magnet approach and components

Two distinct coil designs that are used to create highly homogeneous fields are the compensated solenoid and the discrete multi-coil configuration.

The compensated solenoid originated in NMR and was employed early in MRI magnets. A solenoidal coil uniformly wound across the full length of the former is the major component of this design. The inhomogeneity created by its end effect is compensated by an optimized set of coils (compensation coils), wound on the outside of the solenoid (figure 5). The solenoid is often sectioned into several windings with graded superconductors, for structural reinforcement and cost reduction (Liebel 2011). The key advantages of this approach are a low ratio $B_{peak}/B_0 \sim 1$ and better stress control; while a disadvantage is its intrinsically large amount of superconductor and cost. The amount of required compensation grows rapidly when shorter lengths or larger FOVs are pursued (Lvovsky and Jarvis 2005), as does the total amount of conductor and stresses in this design. The use of active shielding faces a significant challenge due to the higher dipole moment of the long solenoid, the increase in stresses and the need to compensate inhomogeneity contributed by the shield coils. Therefore in WB MRI scanners the compensated solenoid design is reserved for high-field research magnets ($B_0 = 7$ T or 9.4 T), where having a low B_{peak}/B_0 ratio is critical for the use of low-cost commercial NbTi conductors. Such magnets are
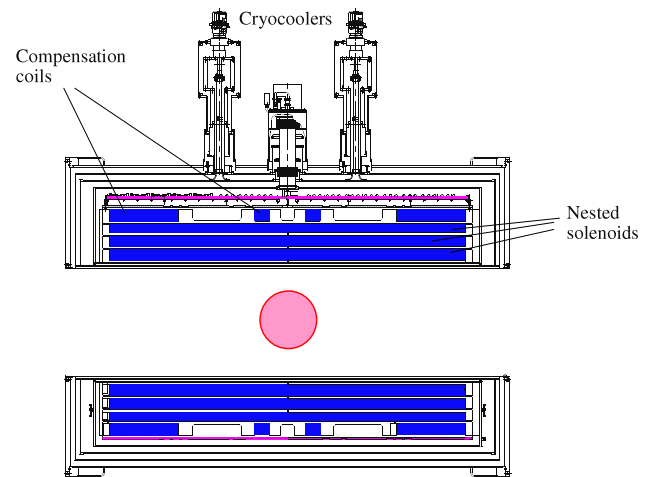

Figure 5. Coil configuration for the compensated solenoid approach (GE 7 T magnet).

longer (length up to 3 m or more) (Liebel 2011) than the clinical 1.5 and 3 T magnets, which use the discrete coil design. Until recently, most were passively shielded with heavy iron plates built into the site structure.

The multi-coil design, on the other hand, places emphasis on a true minimum ampere–meters of superconductor for a given homogeneity, albeit at the expense of higher B_{peak} and stresses. This is the dominant configuration in cylindrical clinical MRI magnets with $B_0 \leq 4$ T. Discrete field-shaping coils are strategically distributed along the bore to compensate each other's zonal harmonics. The number of coils is dictated by the balance between the number of variables (coil positional angles) and the number of harmonics to be compensated (Lvovsky and Jarvis 2005). Secondary variables, such as coil shape and Cu/SC ratio, can help additionally tune B_{peak} and stresses in the coils. Six field-shaping main coils (three coil pairs in a symmetrical magnet, see figure 3) represent a common configuration for an MRI scanner, having up to 10th order harmonics compensated over a FOV with dimensions half those of the magnet bore diameter.

Modern clinical scanners are actively shielded. Sets of shielding coils, coaxial to the field-shaping coils and having opposite current direction, are positioned inside the helium vessel at the outermost radius in order to reduce the fringe field of the magnet. Homogeneity in the multi-coil design, which relies on a balance of harmonics between the coils, is especially sensitive to coil position variations, within a fraction of a millimeter. Intra-coil and inter-coil Lorenz forces are addressed in the structural design of the magnet. A conductor stabilizer usually provides the main support for the intra-coil stresses; sometimes overbind is wound on top of the coils to control hoop stress in the coil.

Whether the coils are in-pocket wound, or modular (i.e. wound and impregnated off-line), the former and its coil interfaces have to accommodate considerable inter-coil forces. For example, the force F_z on the outermost main coil can exceed 0.8 MN in a 1.5 T and 3.5 MN in a 3 T whole body magnet. A key challenge is managing stresses and movements at the coil interfaces. The interface design has to allow transfer
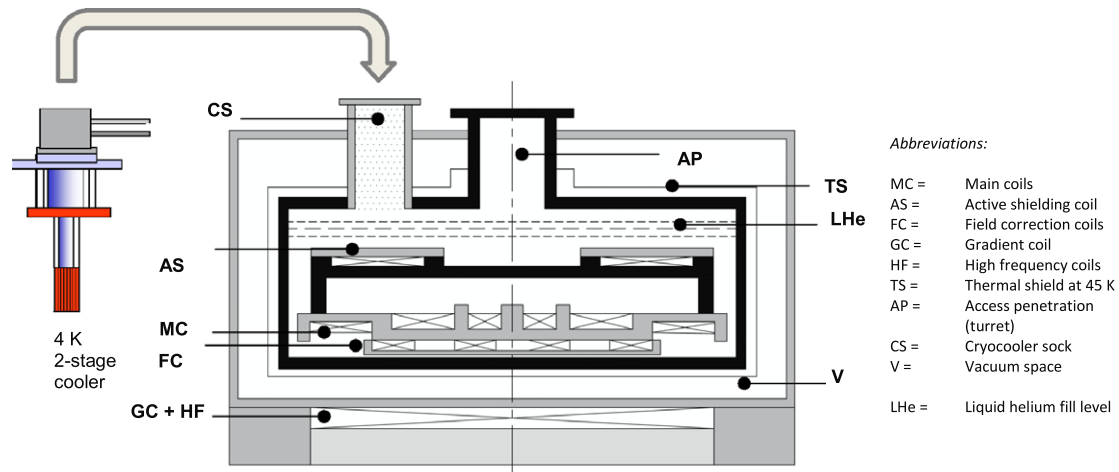
Figure 6. Traditional cryostat for an MRI magnet with a cryocooler sleeve (adapted and modified from Komarek (1995)).

of full inter-coil forces without frictional disturbances that would quench the coil during energization. The main (inner) former can either be designed as a separate component, or incorporated into the helium vessel inner cylinder. Likewise, the shielding coils can use a separate former, or be wound in separate channels and supported off the main former.

If active shimming is employed, a set of correction coils is added. A full set of correction coils includes transverse shim coils and usually requires a dedicated former. If only a limited number of zonal harmonics (Z_1, Z_2) is targeted, correction coils can use the space between the field-shaping coils or be wound on top of them.

In either configuration, the following circuit components are placed within the 4 K envelope (figure 3):

(a) Superconducting joints between coils, each with resistance $\sim 10^{-10}$ Ω or less. They guarantee persistent operation with a long-term drift rate under 0.1 ppm h^{-1}.

(b) Main superconducting switch with an embedded heater. The heater is activated during magnet ramp, and turned off after the magnet is parked to close the persistent circuit.

(c) Quench protection circuit components. These may include resistors, diodes and a quench protection switch that opens during the quench event and diverts current into the quench heaters embedded in the coils. These heaters start secondary normal zones and spread the dissipating stored energy.

(d) Power leads—can be either retractable or permanently embedded.

(e) Superconducting joints and switches are placed in designated low-field areas with an adequate cooling arrangement in order to ensure their stable, reliable performance.

The majority of commercial MRI magnets use a helium bath in which coils and components are immersed; although scanners with conduction-cooled magnets have also been developed (Herd *et al* 1995, Havens 1995, Havens and Smith 1997, Laskaris *et al* 1995, Razeti *et al* 2008, Byrne *et al* 1999).

2.3. Helium bath cryogenics

Figure 6 shows the typical cryogenic infrastructure of a cylindrical MRI magnet. In this example the cryostat has an outer vacuum case (OVC) made of metal, one thermal shield (usually at a temperature of 40–50 K) and the helium vessel, housing the magnet assembly. Top left shows a typical cryocooler in its vertical orientation, ready to fit into the cryocooler sleeve, as indicated.

The liquid helium fill level to keep the magnet superconducting at 4 K is also shown. For a complete fill, typically 1500–2000 l is used. Depending on the temperature gradient that may develop inside the magnet (from bottom to top) and on the superconducting coil design, which defines coil stability, lower fill volumes may be tolerable. The minimum allowable volume may also differ between the ramping process and the subsequent persistent operation of the ramped magnet.

Any advanced/alternative cryogenic concept for MRI applications needs to address all the following operating modes:

- Energy saving pre-cooling of the magnet down to the operating temperature (usually done with liquid nitrogen or a recoverable liquid helium facility).
- Magnet ramp up to full field, preferably with captured boil-off helium gas during ramp.
- Normal operating condition (NOC), see also section 5; self-contained operation.
- NOC with extra heat loads (due to gradient heating) that reduce the cryogenic margin, and ensure no helium loss (zero boil-off/recovery).
- Ramp down.
- Shipping 'ride-through' (from factory to MRI site), optimizing losses to minimize the cost.
- Cooldown to operating temperature or refill at the customer site, with high-efficiency transfer.
- Safe ramp up at the customer site.

- Magnet quench, with an energy dump into a liquid helium bath (see also section 5 for details). Quench gas may be captured in the factory, but normally would be released into the atmosphere through a vent line at the customer site.

Cryocooler technology is constantly progressing. Currently, the dual-stage cryocooler cools the thermal shield thermally linked to its first stage. The second stage is connected to the recondenser which re-liquefies escaping helium gas from the helium vessel (the so-called zero boil-off operation, or ZBO, the technology developed and introduced into products by GE (Chen 1997)).

The cryocooler (GM type 4 K cooler) is usually fitted in a separate cryo-sleeve and does not share the vacuum of the main cryostat. The so-called sock is either evacuated or directly connected to the cryostat helium reservoir and is thus serviceable. The performance of the cryocooler degrades in the field by about 0.13 W yr^{-1}; therefore the cryocooler usually requires replacement after a few years of service, depending on the cryostat background heat load. With the introduction of the Pulse Tube Refrigerator (PTR) with an absence of serviceable parts, this type of cryocooler can be deeply embedded in the cryostructure, taking on even further design roles, as described for example in Stautner (2001, 2002). PTRs are now commercially available, and their reliability keeps improving. With reference to the above cryostat operating modes, the PTR offers further unique advantages not commonly known, namely the ability to drastically shift first and second stage cooling power by changing the mutual flow distributions. This is most beneficial whenever the thermal shield demands more cooling power during cooldown, e.g. at the customer site or when a transient increase of the liquefaction rate is desirable.

Advanced MRI units should also address every aspect of reducing the environmental burden by incorporating green technologies as much as possible. One key aspect herein is the reduced cryogenic liquid helium (LHe) inventory. Another is power consumed by the refrigeration system (mainly by helium compressor), the gradient system and overall electronics. Among others is coil former recycling and lead-free components, to name but a few.

3. Non-traditional configurations

3.1. Quest for openness

3.1.1. Challenges of wide/short bore. With any MRI scanner for human applications, either for whole body or specialty imaging, the key driver that has an influence on the magnet configuration is the patient space. Since the early days of clinical imaging, patient comfort has always been behind the quest for more open scanners.

Besides accommodation of claustrophobic patients, the larger diameter and shorter bore of the whole body scanner enables interventional procedures, such as catheterization, IV and others, when the patient has to be reached inside the scanner. As a result, in the current whole body cylindrical MRI market the trend is developing towards a 70 cm patient bore (PB) as a new standard for high-end scanners, that was previously dominated by a PB = 60 cm. A shorter magnet length is often pursued to allow the patient's head outside the magnet for the majority of procedures.

For the specialty scanners, such as head or extremities, a larger and shorter bore provides better accommodation of specific human anatomy. A smaller size of the magnet and the specifics of the application may provide more opportunities to take advantage of the anatomy (for example, narrow head versus wider shoulders) than the 'universal' WB configurations.

Both with WB and specialty magnets, more effective use of the bore space can be traded for other key parameters, such as field strength B_0, homogeneity, and fringe field in an attempt to optimize the system cost.

The outline of space occupied by the superconducting coils will be further referred to as the coil envelope. In cylindrical magnets the coil envelope is constrained by four boundaries—the inner and outer radii R_{min} and R_{max} plus the two outermost axial Z-positions (often shorter for the shield coils that for the main coils, due to the need to support their outward forces).

Overall, the resonator module contains nested envelopes of different levels (figure 3). The scanner covers delineate its outermost envelope, which directly defines the patient space and comfort. The magnet, or vacuum vessel envelope, is the next inside. Space between the covers and the magnet accommodates: (a) the cover mounting, (b) other scanner components such as the gradient and RF body coil, and (c) their electrical and cooling connections. Because of this space occupied by the gradient and RF coils inside the bore of a cylindrical scanner, the patient bore PB = 600–700 mm translates typically into a magnet bore (MB) diameter of around 900 mm. The performance of both the gradient and the RF coil is highly sensitive to their annular space, therefore the tradeoff between the MB and gradient/RF radial space has an important impact on the optimal MR design.

The coil envelope is incorporated inside the magnet envelope. The space between the two is defined by the cryostat components and coil support elements such as formers. Coil envelope boundaries to a large degree limit the cost and performance in a homogeneous magnet design, and consistent efforts have been applied to minimize this space. The introduction of a zero boil-off cryostat (Chen 1997, 1998) with a helium recondenser brought about a magnet design with a single thermal shield (40–60 K range) instead of two (at ~20 and ~80 K). This resulted in a noticeably reduced cryostat space and shorter magnets. Improvements in the performance of multi-layer insulation (MLI) further reduced the gaps between the magnet and coil envelope. Certain designs allow intrinsically better utilization of the magnet space by coils, for example those with modular off-line coils that have reduced or no former at R_{min}, or cryogenless designs with the elimination of the helium vessel.

In superconducting cylindrical MR magnets, to create a field-of-view (FOV) adequate for whole body imaging, the envelope-constrained coils need to generate a region with $Z_{FOV} \geq 0.40\,R_{min}$; $R_{FOV} \geq 0.45\,R_{min}$ and homogeneity

of 10 ppm peak-to-peak. The coil radii R_{min}, R_{max} and length Z_{max}, fringe field and FOV are key coil envelope and field requirement constraints that affect the amount of superconductor, peak field and stresses, and hence the cost and risk of the design.

Multiple coils have to be strategically placed in the coil envelope to achieve a balanced field of the required uniformity. A targeted FOV defines the maximum order of axial harmonics N that need to be canceled (equivalently, the number of derivatives $d^N B_z/dz^N = 0$), and thus affects the number of discrete coils required, which have to balance out each other's inhomogeneities. (In practice, however, some magnets are designed around homogeneity at field points following a certain profile that may have residual lower order harmonics in an ideal design.)

When the length of the cylindrical envelope is not constrained, the coils will occupy their natural positions, which correspond to the minimum of ampere-turns (Lvovsky and Jarvis 2005). Once the length is shortened beyond the outermost natural position, the amount of conductor and peak field B_{peak} start to increase. The shorter the magnet length, the larger the opening angle $\alpha = \tan^{-1}(R_{min}/Z_{max})$ of the coil envelope, and the bigger the design penalty. Such a dependence is shown in figure 7, where an unconstrained region can be observed at $Z_{max} > 65$ cm, followed by an accelerated increase of V_{cond} and B_{peak} for shorter magnets. Starting at $\alpha \sim 37°$, a negative coil pair appears between the outermost (large) and adjacent (medium) coils, which creates an outward force on the outer coils and requires additional space for the outer flange support. Compressed and moved inward, the outermost coils acquire a high pancake-like aspect ratio. The total number of coils and the number of new negative pairs keep growing—until, at some critical value Z_{max}^*, the solution ceases to exist (from the practical standpoint, the magnet configuration becomes unfeasible well before this point because of unacceptably high B_{peak} and stresses in the coils). The critical envelope length Z_{max}^* (or critical angle α^*) depends on the coil current density J_{eng}: the higher J_{eng}, the larger the critical angle α^*.

A similar 'knee dependence' appears with regards to other parameters. Selecting the right point on the 'knee' is key to optimal magnet design. Such a selection is based on tradeoffs between the magnet length (bore radius, FOV) on one side, and the cost and risk of the design on the other. Moving up the knee beyond the appearance of the first negative pair becomes increasingly difficult, as the outward forces from the growing negative coil on its outermost positive neighbor grow very fast, which requires additional space at the outer flange for structural support of the forces, which negates any achieved shorter length.

Additionally, at that point the conductor length, peak field and coil stresses have increased dramatically, which would translate into a high-cost and high-risk design. All these considerations dictate a practical limitation to the level of openness of cylindrical MRI.

For a given envelope, the magnet cost and risk are directly linked to the selected coil current density J_{eng}, and the operating fraction of the critical current $i_{op} =$

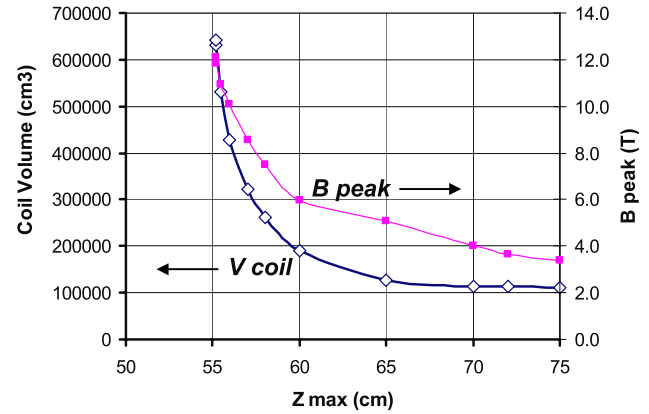**Figure 7.** Sensitivity of the coil volume and peak field to the length of the coil envelope $L_{env} = 2Z_{max}$. Example shown for $B_0 = 1.5$ T, FOV $= 45$ cm $\times$ 45 cm, 5 G line $Z \times R = 4.5$ m $\times$ 2.5 m; $R_{min} = 50$ cm; coil current density $J_{eng} = 15$ kA cm^{-2}.

I_{op}/I_c (B_{peak}). The latter is determined by the cross-section of NbTi, while the first is mostly determined by the copper stabilizer. A sufficient area of copper in the conductor is needed for (a) reacting hoop and axial stresses in the coil, (b) conductor stability and (c) quench protection. The amount of superconductor (Cu/NbTi ratio) is determined by the required stability margin and persistence. While different coil technologies, such as wax or epoxy impregnated may have different stability limits, resulting in different maximum i_{op} values, the persistence limits in commercial MRI NbTi-based conductors with a n-value above 30 usually allow $i_{op} > 0.7$. As the persistence, and to a large degree the stability margin, are mainly influenced by the few inner layers in the coil with the highest B_{peak} (Lvovsky 2009), the use of so-called conductor grading, both between the coils and within the same coil pocket, is often employed for cost and risk savings.

MR scanner configurations other than tubular have been explored, and some are described below. However, none so far can match the wide use in clinical practice of the mainstream WB cylindrical systems. This is mostly due to the universality of their scanning applications; the efficiency with which a cylindrical system generates a large homogeneous FOV; and a well-optimized cost-driven NbTi-based design that has been developed in a highly competitive marketplace.

For specialty scanners, non-traditional topologies may provide additional advantages, with shapes better adapted to specific human anatomy. They may also provide opportunities for smarter utilization of the overall scanner space, including gradient and RF coil placement. The smaller dimensions of specialty scanners with a small bore and small coils result in low intra- and inter-coil stresses. That enables simpler former and cryostat solutions, and may facilitate easier introduction of novel MTS and HTS superconductors.

3.1.2. Split-open configurations. An existing patient-friendly alternative to the described tubular topology, often called the open or split MRI configuration, is the one where the patient space is not constrained inside the solenoidal coils,

Table 3.1. Parameters of commercial WB split-open MRI scanners with superconducting magnets (see figure 11).

Parameter	Signa-SP	OpenSpeed	Panorama 1T	Oasis 1.2T	OpenSky
Manufacturer	GE	GE	Philips	Hitachi	Paramed/ASG
Product introduced	1994	2000	2004	2008	2006
Central field B_0	0.5 T	0.7 T	1.0 T	1.2 T	0.5 T
Field orientation	Horizontal	Vertical	Vertical	Vertical	Horizontal
Geometry	Split bore (2 annuli)	Vertically split gap	Vertically split gap	Vertically split gap	Horizontally split gap
Frame/posts	2 posts, at top and bottom	2 posts 120° apart	2 posts 180° apart	2 posts 180° apart	U-frame, soft iron
Cryostat length/height, (excl. cold head) (cm)	183	183	204	220	240
Cryostat OD (cm)	193	172	223	—	200
Patient gap (cm)	58 gap, 60 patient bore	45	45	45	58
Imageable DSV	>30 cm	40 cm	45 cm	45 cm	26 cm
0.5 mT line (R (m) $\times Z$ (m))	8.1×10.2	4.7×3.8	4.0×2.6	—	4×4
Shielding	Passive	Active	Active	Active	Passive
Shimming	Passive	Passive	Passive	Passive	NdFeB PM shims
Magnet weight (ton)	3.6	8.4	7.0	—	25
Superconductor	Nb_3Sn tape	NbTi wire	NbTi wire	NbTi wire	MgB_2 tape
Operating temperature (K)	~10	4.2	4.2	4.2	18
Cryogenics	Conduction-cooled	Zero boil-off He bath	Zero boil-off He bath	Zero boil-off He bath	Conduction-cooled
Helium volume (l)	None	300	1500	—	None

but rather created between them. The body of the patient enters the scanner between the two poles of the magnet, perpendicularly to the direction of the magnetic field B_0, i.e. to the axis of solenoidal coils. Most open MR scanners have a horizontal gap ΔZ with a vertical field B_0, but there are systems with a vertical gap and a horizontal Z-axis as well. Examples of commercial whole body superconducting MRI scanners with a vertical B_0 orientation are the GE 0.7T OpenSpeed, Philips 1.0T Panorama and Hitachi 1.2T Oasis. Among scanners with a horizontal field orientation are the GE 0.5 T Signa-SP (Nb_3Sn 'double-donut' interventional configuration), or Paramed's 0.5T MgB_2 OpenSky scanner (parameter comparison, see table 3.1).

Split MR magnets can be divided into the following two categories:

Type I—with soft iron frame (yoke) connecting the two poles. The yoke serves as a low-reluctance magnetic connecting path that closes the space outside the poles, thus constraining and channeling the magnetic flux generated by the coils. The superconducting configuration of this type takes its origin in earlier permanent and resistive iron-assisted MRI magnets. There the iron frame has either a C-shape, where the patient table travels along the wide back of C (e.g. 0.35 T Siemens Magnetom C!); or an O-shape, where the patient enters between the two columns on each side of poles (e.g. 0.3 T GE Brivo MR235); or 4 columns. Besides their function for channeling magnetic flux, the columns also serve as structural elements providing mechanical support against the large attractive forces between the poles. In superconducting magnets, the supporting columns also carry cryogenic connections between the two halves of the magnet

(Herd *et al* 1995). Homogeneity in the magnets with the iron yoke is provided by the pole design while the superconducting coils act simply as generators of a magnetomotive force, much like permanent magnet blocks or resistive coils. Control of the fringe field is done by a yoke design that limits the leakage field into the room, so no shielding coils are required. This configuration does not require multiple strategically positioned coil pairs, and a single coil at each pole may be sufficient. In contrast to the type II configuration, precise control of the coil positions in the type I magnets becomes less critical, due to the substantially reduced sensitivity. Paramed's 0.5T MgB_2 OpenSky (magnet by ASG) presents an example of such a configuration. The central field in the type I configurations does not exceed 0.5 T. The effectiveness of the soft iron yoke diminishes at higher fields while its weight grows. The tradeoffs in the type I design include the gap, homogeneity, fringe field and weight of the magnet. To achieve high B_0 with a 45 cm DSV in a whole body gap while sufficiently constraining the leakage field, the frame weight may exceed 20 ton, which impacts the siteability of such a scanner.

Type II split-open magnets represent a much lighter alternative, with no iron frame present. In the absence of a magnetized pole, the superconducting coils are responsible for creating the homogeneous region of the central field B_0. A set of multiple coils is located symmetrically in each half of the split magnet; precise positioning of the coils is critical. In some 'intermediate' designs where the superconducting coils are assisted by ferromagnetic elements (Laskaris and Palmo 1999), the primary role of those would be limited to force management and conductor reduction. Similar to cylindrical
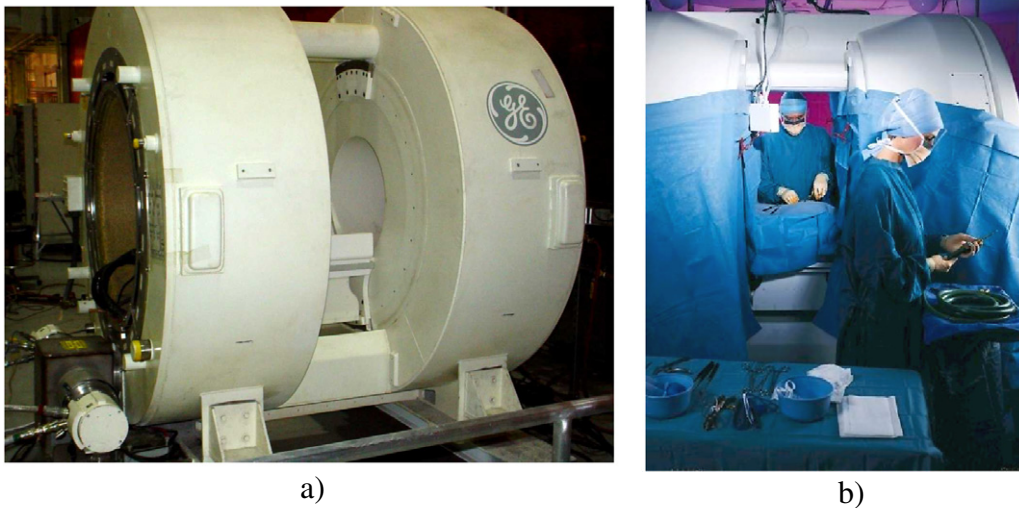
Figure 8. First whole body interventional conduction-cooled Nb_3Sn MR magnet; $B_0 = 0.5$ T. (a) Configuration with a patient bore and surgeon access—magnet without covers; (b) scanner Signa-SP during surgery arrangement.

magnets, in ironless split magnets the magnetic flux returns through the air around the magnet, therefore to keep the 5 G line within the required limits, active shielding coils are required. Large attractive forces between the poles are reacted by posts that represent the cold structure connecting the two halves inside the 4 K region.

Type II WB MRI magnets have been created for field strengths from 0.5 to 1.2 T, although designs up to 2 T have been discussed (Borceto *et al* 2012). The practical limit on the field strength in the type II configuration, as in cylindrical MRI magnets, is dictated by the maximum stresses, conductor stability and the overall cost of the design.

The first split superconducting commercial MRI magnet was designed by GE for interventional Signa-SP scanners and installed in 1994. Since then, a total of 15 have been in operation in different clinics throughout the world. The 0.5 T scanner with horizontal field orientation takes images of the operational area in real time during surgery. It is remarkable that the first whole body split magnet design started with the most challenging topology dictated by its interventional nature for surgical applications (Havens 1995). In addition to the traditional horizontal bore, which accommodates a moving patient table, it had vertical gap in the middle for surgeon access (figure 8). It was also the first cryogen-free conduction-cooled whole body MRI magnet (used two cryocoolers). The superconducting coils are wound from Nb_3Sn tape conductor. This interventional scanner has a patient bore and surgeon gap, which includes space occupied by the gradient coils located in the bore and inside the gap. The magnet weight is 3.6 tons.

A substantial challenge exists when scaling such an interventional topology to 1.0 T and higher. The combination of the full-size bore with an appreciable room-temperature gap for surgeon access imposes a steep penalty on the magnet design, impacting stresses, B_{peak}, and the amount of conductor, hence rapidly increasing the magnet cost. In addition to limitations for the magnet, this topology creates
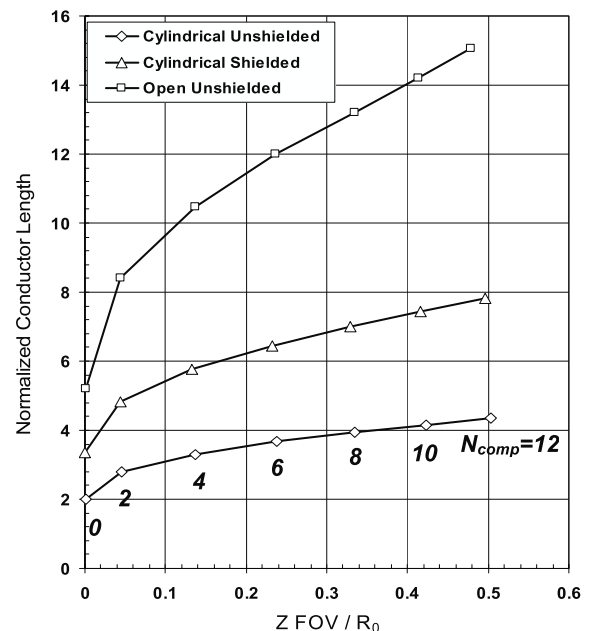

Figure 9. Comparison of the amount of conductor in cylindrical and split-open configurations, as a function of the ratio of FOV-Z to the coil radius, or half-split for the open geometry (Lvovsky and Jarvis 2005). Copyright 2005 IEEE.

a challenge for gradient coil performance, as split cylindrical gradients now have an interruption in the most effective region $|Z| < $ gap/2.

The above limitations became the reason why, in pursuit of image quality comparable to 1.5 T cylindrical imagers, high-field open scanners adopted a pure split geometry without a patient bore. Designs with $B_0 > 0.5$ T are actively shielded, which allows keeping both the weight and fringe field within limits comparable to cylindrical scanners. In each half of the magnet, field-shaping coils are located closest to the gap, while the shielding coils are as far away as

possible, limited by the magnet height. The split geometry of the ironless high-field open design is characterized by the following key features and challenges:

(1) An increased amount of conductor compared with a cylindrical magnet of the same FOV. Figure 9 compares normalized ampere–meters for unshielded cylindrical and split-open configurations (Lvovsky and Jarvis 2005). While the dimensionless comparison in figure 9 is given for a gap having the same size as the bore diameter in a cylindrical scanner; the difference would be smaller for real vertical clinical systems, as a 40–45 cm vertical gap can adequately accommodate human anatomy with its smaller anterior dimensions. The split configuration includes negative polarity coils among the field-shaping coil set;

(2) The need to have two cryostats separated by posts significantly increases the number of cryogenic components and complexity of the assembly compared with the mainstream cylindrical magnets. The two-vessel cryogenics becomes a primary cost driver for split-open magnets. With vertical systems, consideration should be also given to the helium connections between the two vessels and the dynamics of helium levels in them. Helium boil-off in the upper vessel (e.g. during power outage) would start exposing the shielding coil, while the level in the lower vessel would create the risk of fast exposure of the most vulnerable main coils, which are located at the top near the gap.

(3) The significant attractive force between the two halves has to be met by 4 K structural components inside the posts. The two posts carry all the cryogenic and electrical interconnects between the halves. Post locations (either 180° apart, or at an angle) present a tradeoff between system stiffness, on one hand (vibrations impact on image quality), versus openness/interventional access, on the other. Since primary Lorenz forces are acting on individual coils, an adequate coil support structure (formers) has to be designed into each half. Such a structure provides local support for each of the coils while transferring substantial total axial forces to the post supports that connect the two halves. Its design has also to ensure that the out-of-plane coil deflections, a potential source of transverse harmonics $Z_{2,1}$; $Z_{2,2}$ etc, would stay within the maximum allowable limits.

(4) For vertical MRI scanners, fringe field containment within the imaging room of a multi-story hospital presents a particular challenge. Unlike with a horizontal cylindrical magnet, here the small vertical distance to the floors above and below imposes tight limits in the unfavorable Z-direction. Some leverage can be gained by increasing the diameter of shielding coils, each having compensating negative dipole moment

$$M = (\pi/3)I_{\text{op}} \sum_{n_{\text{coil}}} N_n (Ri_n^2 + Ro_n^2 + Ri_n Ro_n), \qquad (4)$$

where I_{op} is operating current, N_n is the total turns in the nth shielding coil, and Ri_n and Ro_n are the inner and outer radii. A conical configuration with a shielding diameter larger than the main diameter lends itself to a improved perception of openness (Lvovsky et al 2003), albeit with an increased overall diameter, impacting interventional access to

the imaging region. When the fringe field constraint along the Z-axis is placed too close to the magnet, multiple shielding coils appear (Lvovsky and Jarvis 2005), driven by need to carefully shape the local field from the shielding coils to conform to the required 0.5 mT line.

(5) Vertical split-type scanners often take advantage of the different human body orientation by employing an ellipsoidal FOV with $FOV_Z < FOV_R$, due to the lesser design penalty for extending the homogeneous region in the radial direction. A large circular area in the coronal XY plane provides coverage from side-to-side and along the body, while the smaller FOV_Z axis is adequate to cover a shorter anterior–posterior, front-to-back anatomy. A shorter FOV_Z also helps in reducing the inter-coil gap, providing a sufficient distance between the coils on each side of the gap and the FOV. Additionally, due to gradients recessed in the poles, the split-open topology places small coils farther away from the patient surface. As a result, FOV-Z in the split-open EM design can be extended to be almost equal to the patient gap.

(6) The shimming system challenges are rooted in the limited space and specifics of the split-type orientation. To provide enough degrees of freedom in the set of compensating spherical harmonics (2–3), the distribution of passive shim elements has to cover a sufficient range of angle θ. While in a cylindrical MRI the shimming positions are distributed along the bore, thus covering $\theta_{\min} < \theta < \pi/2$, the split-open magnet has shim pieces in the poles (recesses), i.e. within an angle $0 < \theta < \theta_{\max}$. Positions with small θ help with higher-order harmonics, but are less efficient for the low orders. The limited distance ΔZ reserved for the shim system by the expanse of the gradient and RF space, imposes limitations on the total shimming capacity, as well as on the maximum Z-dimension of each shim element. Shim magnetization is more challenging compared with cylindrical scanners, where a single shim element positioned along the bore can commonly occupy 10–20 mm or more in the Z-direction, and easily saturates to produce a magnetic moment M_z.

(7) Finally, the split geometry dictates that gradient and RF coil halves are placed in the designated recesses made in each pole. Such a gradient and RF topology, with its limited space affecting patient gap size is intrinsically less effective in producing high strength G_x, G_y, G_z, B_1 fields compared with the traditional annular arrangement of cylindrical scanners. The recess is usually sized to occupy a radial space limited by smaller field-shaping coils only, leaving large coils as close to the gap as possible, in order to reduce the penalty to the magnet design (Lvovsky et al 2003) (figure 10(a)). Conical recess and conical gradient coils (Overweg and Aldefeld 2003) (figure 10(b)) allow improved separation between primary and shield gradients, thus increasing the gradient strength and incurring a gradual progression of space penalties on each subsequently smaller field-shaping coil.

In clinical practice, split-open MRI scanners have to compete with a wider bore and shorter tubular MRI. Even not having full openness of the split magnets, shorter tubular scanners address a substantial portion of claustrophobic concerns. The primary driver is the wider patient bore; expanding the segment of scanners with a 70 cm patient bore
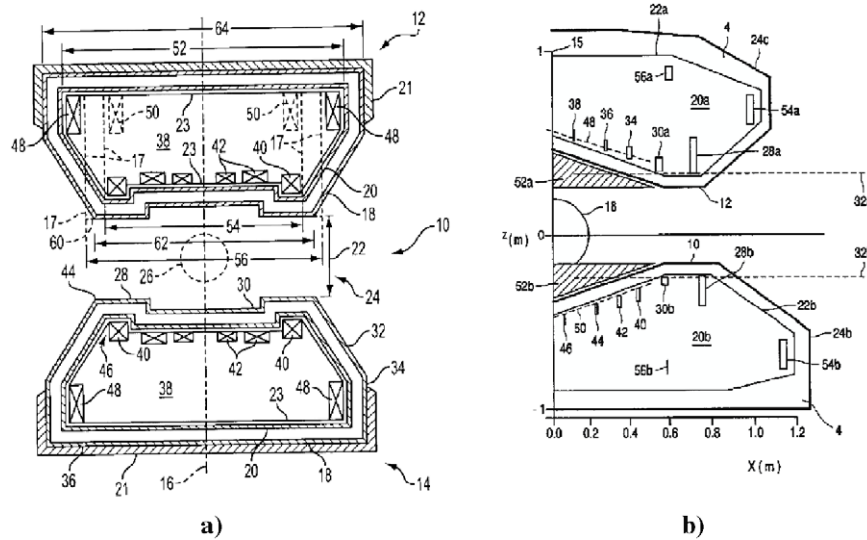
Figure 10. Cylindrical (a) and conical (b) gradient/RF recess in split-open MRI scanners (Lvovsky *et al* 2003, Overweg and Aldefeld 2003).
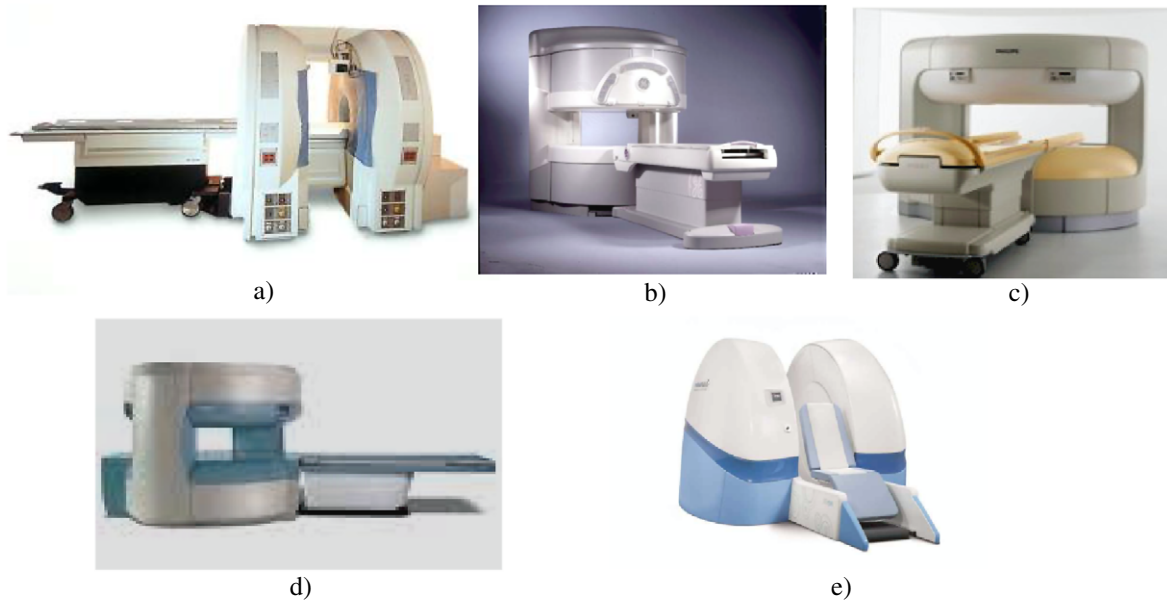

Figure 11. Split-open WB superconducting MRI scanners: (a) 0.5 T Signa-SP interventional (GE); (b) 0.7 T OpenSpeed (GE); (c) 1.0 T Panorama (Philips); (d) 1.2 T Oasis (Hitachi); (e) MgB_2-based 0.5 T OpenSky (Paramed).

becomes a new standard that is replacing the 60 cm segment for clinical installations where customer comfort is paramount (even though the bore has to be traded off for space and hence some performance of gradients). Ultra-short scanners, such as Siemens 125 cm long Espree, improve the openness angle, albeit as mentioned above (figure 7) such a gain in openness has to be weighed against an inevitably smaller FOV and higher magnet cost.

In summary, the present split-open topology for the whole body scanners, albeit attractive for patient openness, is limited to the low-end-B_0 scanners. The intrinsically high cost of the double-vessel configuration undermines its competitiveness with traditional cylindrical scanners. The introduction of high-T_c superconductors in MRI magnets in the future would ease some of the constraints, such as coil stability limits, thus enabling designs with higher B_0 and B_{peak}. However, a long road ahead is required before other limitations such as high stress tolerance, persistence and, most of all, conductor cost could bring new conductors to the level at which the split-open configuration could reach substantially wider application in clinical practice.

3.2. Non-standard geometries

3.2.1. Types of non-traditional topologies. Early after the onset of superconducting MRI magnets, the pursuit of patient
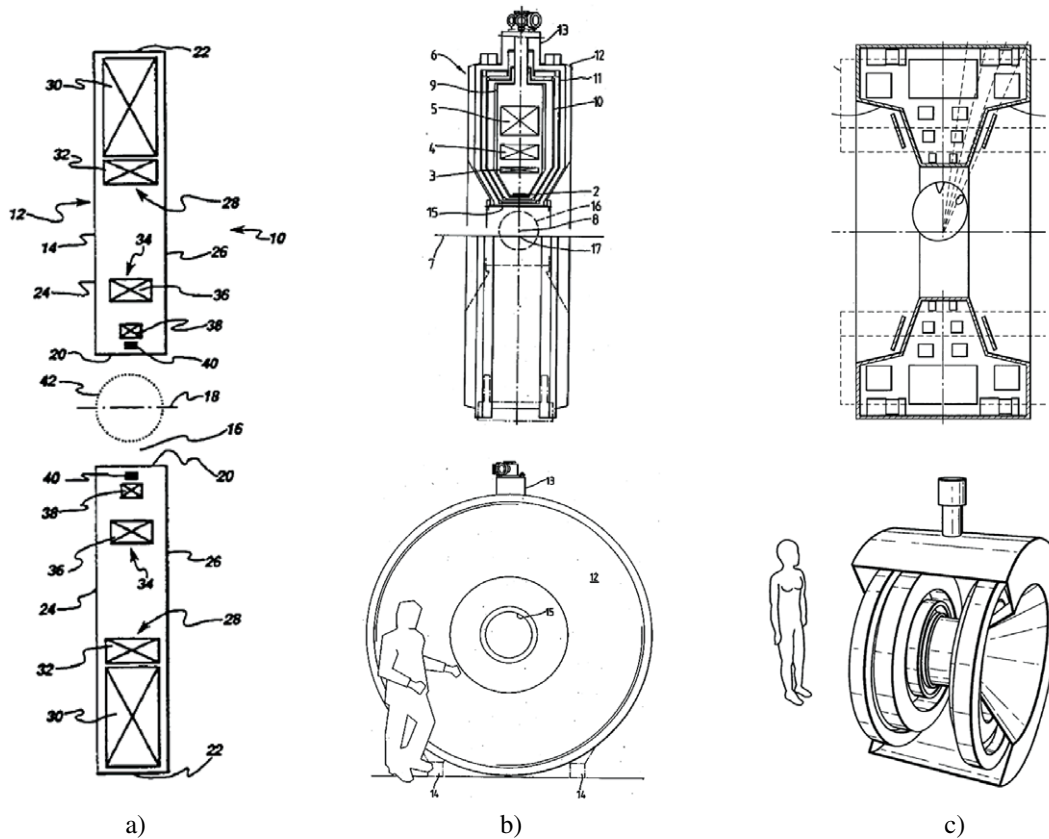
13

Figure 12. Examples illustrating the disk concept: (a) Dorri and Laskaris (1995); (b) McDougall and Bird (1987). (c) McDougall and Hanley (2008).

openness has generated interest in non-tubular geometries. However, within traditional superconducting technologies, limitations and penalties have not justified departure from the tubular imagers for clinical use—other than the split configurations discussed above.

With regard to patient accommodation and location of the imaging FOV, the non-traditional magnet geometries for MR scanners can be classified into the following three general categories:

(a) Magnets with a tubular patient bore where the patient's anatomy is accommodated and the imaging is performed (either the whole body or part of it, such as extremities or head). Departure from a traditional cylindrical magnet towards better openness is done either by substantially shortening the magnet, or moving the FOV off-center or even outside the bore. A disk (pancake) magnet with a bore and a cylindrical magnet with an offset FOV fall under this category.

(b) An external FOV is projected outside the coil envelope. The imaged tissues are positioned outside the cryostat (vacuum vessel) and the presence of the warm bore in the magnet is not necessary. The patient would be lying or positioned at the magnet side.

(c) Patient is inside the magnet, and enhanced openness is achieved in the space between the field generating elements (coils or ferromagnetic yoke). 'Suntan bed' and FOVs between the coils and ferromagnetic frame are attempts to further improve the openness of the 'split' geometry.

Typical configurations and their features are discussed below.

Disk (pancake) magnets

The ultimately short MR magnet would fulfil the elusive goal of a 'CT-like' scanner with a 'disk magnet', where the patient is surrounded by an <1 m short bore. Such configurations have been considered but have not materialized in a product, due to the stiff design and cost penalties of such configurations. The penalties are both for the magnet and the gradients, having disk versus traditional tubular geometry. With an extremely short bore, the coil space would have to fit in an envelope with a 50–70 cm axial wide space. In order to balance the harmonics for a homogeneous FOV, with little freedom now available with regard to Z-location or θ-angle of coils, multiple coils would have to be nested within each other within such envelope. Alternating negative coils are required for harmonic compensation (Dorri and Laskaris 1995), much like in the split-open geometry (Lvovsky *et al* 2003, Overweg and Aldefeld 2003). The amount of conductor generally increases for each nested coil with larger radii that are positioned further from the bore. The required growth of the disk-like cryostat, as well as the increased hoop stress in the outer coils, usually limit designs to small FOVs, small B_0, or both.

This fundamental topology trading—cylindrical coil envelope for disk envelope—essentially means that the axial direction with the multiple main coils distributed along the
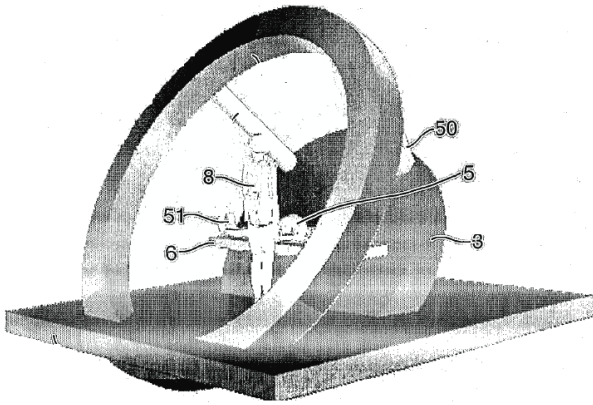
Figure 13. 'Walk-in' disk magnet for interventional applications (McDougall and Hanley 2004).
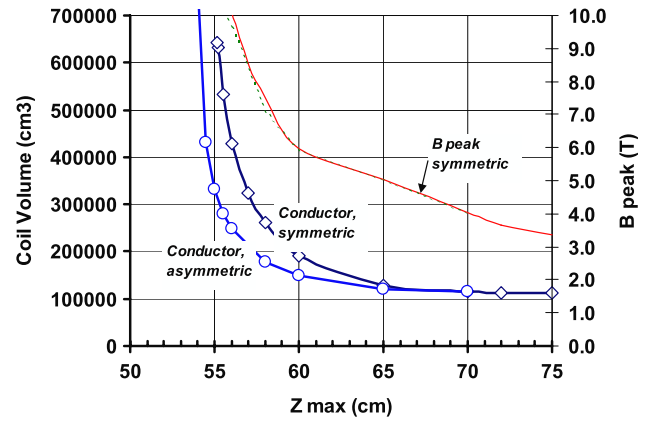

Figure 14. Comparison of optimized conductor and peak field between an asymmetric magnet with a shifted FOV and a traditional symmetric configuration. Z_{max} represents the distance from the FOV center to the outermost coil outer flange (to either end in the symmetric case; to the short end in the asymmetric case).

main former cylinder and limited by the magnet length, is now replaced by a radial direction with field-shaping coils alternating along the radius and limited by the magnet OD (figure 12). A combination or partial use of both directions could lead to an inverted cone-like disk with its axial length smallest at the patient bore, and gradually increasing towards the OD. Additional space gathered in the axial direction at larger radii result in multiple nested coils pairs (McDougall and Hanley 2008), still with a substantial increase of conductor versus a typical whole body cylindrical scanner.

Specialized imagers, e.g. for breast imaging, can take advantage of a smaller bore, and even attempt to project an elliptical FOV outside the assembly (Dorri and Laskaris 1995).

A separate burden such a 'disk' geometry imposes on the space available for gradient and RF coils, as well as on the passive shim system, is that the Z-dimension of the bore is too short (angle α too limited) in the disk topology for traditional gradient and shim solutions. For efficient performance of these subsystems, the design would have to use space near the flanges, which in turn would increase the total width of the disk scanner.

An ultimate example of the disk magnet was proposed by Oxford Instruments in International Patent Application WO2004/097443 (McDougall and Hanley 2004). The magnet is a large ring (about 4 m diameter), which is mounted in the imaging room in the inclined position (figure 13), which allows a 'walk-in' space for the surgeon. Such a configuration faces practical challenges of a low B_0, a small homogeneous region FOV, large hoop stresses and an expansive fringe field footprint, and requires a substantial dedicated clinical space exclusive of other neighboring clinical installations.

Offset field-of-view

The idea of a scanner where the FOV is offset relative to the geometric center of the magnet in order to improve single-sided access has been discussed by many in various embodiments. In the whole body clinical MR magnet, an axial shift of the FOV alone would yield limited benefit that still has to overcome the added cost and complexity of an asymmetric design. For a magnet of a given length L, a FOV offset by ΔZ_{FOV} creates a shorter access length $L_{short} = L/2 -$

ΔZ_{FOV} from one flange but a longer length $L_{long} = L/2 + \Delta Z_{FOV}$ from the other. Figure 14 presents a comparison of such an asymmetric configuration side-by-side with a shorter symmetric magnet that has been shortened from both sides (total length $L - 2\Delta Z_{FOV}$). In this modeling, the amount of conductor has been optimized for each configuration within respective coil envelopes.

When the distance from the magnet flange to the FOV is shortened at one end while keeping the distance at the opposite end constant, the large coil at the short end grows in aspect ratio, and the negative coils start to appear in the short half of the magnet. At the same time, coils in the other, 'long' half remain practically unchanged. In the example of figure 14, large coils at both ends are unconstrained up to about $Z_{max} = 650$ mm. As Z_{max} gets shorter, the conductor and B_{peak} increase rapidly (cf figure 7) only in the coils located in the short half of the asymmetric magnet (while in both short halves of symmetric magnet). Therefore, it is the large coil at the short end that defines the limiting peak field and stress in the asymmetric design. These limiting values are very close to those that occur simultaneously in both large coils in a comparative symmetric design.

While the total conductor increase above the 'unconstrained conductor value' in the symmetric configuration is twice that of the symmetric one, it is the design risk and cost that define the cut-off limit for the shortest access. When comparing asymmetric and symmetric dependences in figure 14, one can note that the asymmetric configuration enables a design with an only 2–3 cm shorter patient access than its symmetric counterpart with the same total conductor, peak field and stresses. However, an asymmetric design has penalties of unbalanced static forces between the main and shielding assemblies, as well as asymmetric fringe field containment and quench protection dynamics.

Although for the example of figure 14 the field-shaping coils were located on the main former, when the envelope is shrunk substantially and coils acquire a pancake aspect ratio, positioning coils in other areas is possible in an attempt
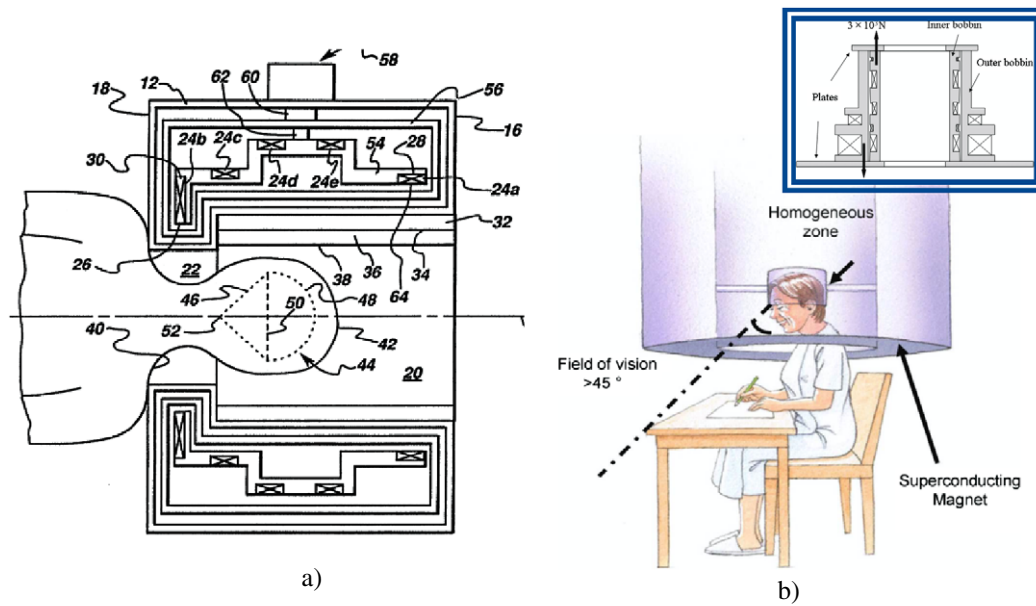
Figure 15. Asymmetric head scanner configurations taking advantage of head/shoulder anatomy: (a) asymmetric envelope with offset FOV (Dorri *et al* 1995a, 1995b); (b) symmetric envelope with offset FOV (Sekino *et al* 2010). Copyright 2010 IEEE.

to better manage stresses and stability of the coils, albeit at the expense of additional conductor length. Discussion of different configurations with an asymmetric FOV center that propose different utilization of the coil envelope space with high aspect ratio coils—multiple formers (Crozier *et al* 2000, Doddrell and Zhao 2007), ferromagnetic elements (McDougall 1987, Crozier and Liu 2008), and others—can be found in various patents and publications. We should note, however, that in the present competitive industry every major MR manufacturer developed a set of efficient optimization tools that allow traversing the whole body magnet envelope and full exploration of coil configuration options, once the design constraints have been set. Generating novel configurations with regard to the number of coils, their location and shape evolved from the art of invention to engineering practice; and the key to the competitive design shifted to the right choice of constraints and tradeoffs between the performance, patient access and cost. While asymmetric configurations with other formers/coil locations than those used in the example in figure 14 may change the exact values from those in figure 14, the overall conclusions on the limitations of an asymmetric design in whole body scanners would still hold.

An offset FOV may become more appealing for specialty, or 'dedicated' imagers, as soon as one can take advantage of non-symmetrical features of the specific human anatomy being imaged, e.g. by departure from the traditional cylindrical envelope (either in terms of magnet coil envelope or magnet–gradient interface space Dorri *et al* 1995a, 1995b, Laskaris and Ogle 1998, Abele *et al* 2011). If, for example, in addition to the shift in FOV, one of the large coils is also moved to a smaller radius, such a geometry suddenly makes asymmetric tradeoffs more appealing both from technical and cost standpoints.

For the head MRI, where the wider shoulders are the defining point, the offset FOV could allow one to minimize part of the bore for shoulder penetration, and either have a narrower part to accommodate the head (Dorri *et al* 1995a, 1995b, van Oort *et al* 1998), or allow better openness during imaging procedures (Sekino *et al* 2010). For orthopedic imagers, an offset FOV in a conical bore could allow better limb access in a shorter magnet, e.g. with different dual access points for upper versus lower extremities (Lvovsky and Jarvis 2009).

In addition to the magnet design, gradient and RF coils have to support the FOV location now shifted away from the center of the bore. The options are either to retain the traditional symmetric gradient/RF coils that are mounted with offset inside the bore, which requires short enough gradient coils (the challenge may arise due to the eddy currents generated in a longer magnet bore by the short gradients that may impact the image quality), or to resort to a non-traditional asymmetric gradient design.

A non-symmetric magnet design, such as the one in figure 15(b), suffers from unbalanced static forces that are now applied to the main coil former—either from the shielding coils or from passive ferromagnetic shielding. While in the symmetric configuration the Lorenz forces acting on individual left and right coils, e.g. from the shielding assembly, are balanced between each other and reacted by the main former that sees zero net force, the non-symmetric configuration requires additional structural support and alignment arrangements to support static net force on the former. Breaking the traditional anti-symmetry between the magnet and gradient coils (by introducing either non-symmetric magnet or gradient design) may result in unbalanced non-zero net torque now applied to the gradient coils, resulting in additional vibration and acoustical challenges for the scanner.
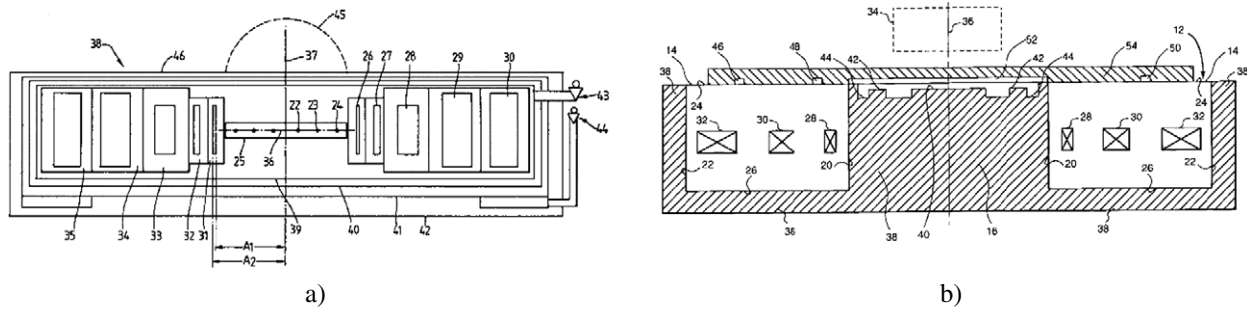
Figure 16. Configurations with (a) a partially projected spherical FOV and iron former ($B_0 = 1$ T, inhomogeneity 100 ppm p/p @ 50 cm DSV (McDougall and Bird 1987)) and (b) a fully projected cylindrical imaging region assisted by a ferromagnetic field-shaping core ($B_0 = 0.5$ T; inhomogeneity 100 ppm p/p @ cylindrical FOV = 20 cm (Z) × 50 cm (R) stand-off 10 cm from magnet top (Laskaris and Ogle 1997)).

All the above-mentioned asymmetric challenges for designs with a shifted FOV manifest themselves on a smaller scale in specialty magnets, due to their smaller dimensions, stresses and stored energy, which in combination with the anatomy-specific benefits makes them primary candidates for introducing such non-traditional designs.

External field-of-view

The ultimate openness corresponds to the patient being outside the scanner, with the homogeneous imaging region projected externally outside the magnet envelope. The apparent difficulty of such a task depends on the projected distance and size of FOV. Both parameters would be smaller and less challenging for specialty imagers that target specific organs of limited size and location. Projecting a FOV of at least 30 cm required for the whole body scanners presents the most difficult quest.

The field generation efficiency inevitably suffers when the field is created away from the coil envelope. Such efficiency is increasingly sensitive when the uniform field is being projected. The difficulty of projecting harmonics $A_{N,M}, B_{N,M}$ rapidly grow with the order N, with the highest efficiency attained for $N = 0$, i.e. for the field magnitude B_0. Therefore, a representative criterion for projection efficiency should include homogeneity characteristics.

Various configurations with projected imaging regions were introduced in the patent literature early on. The field in such 'remote' configurations has sometimes been discussed in terms of B_0, derivatives dB/dz, dB/dx, dB/dy and inflection points. Such descriptions are often indicative of poor homogeneity and small FOV—the challenge quickly accelerates when one, in addition to targeting B_0, attempts to put around an external FOV region with inhomogeneity of order 10 ppm peak-to-peak.

Systematic characterizations of magnetic configurations that generate remote fields were done in a paper by Pulyer and Hrovat (2002). The efficiency of a system of K coils each with N_k turns and current I_k to create B_0 in a remote point in space $\vec{r}_*$ is there described by the criterion:

$$E_{B_0}(\vec{r}_*) = \frac{B_0}{\mu_0 \sum_{k=1}^{K} N_k I_k} \tag{5}$$

which represents the central field magnitude only, normalized by the unit ampere-turn in the system of coils. Different configurations described in Pulyer and Hrovat (2002) by their qualitative field profiles and extrema maps were evaluated according to (5). The conclusion that 'monohedral magnets are not by their nature grossly inefficient' is therefore applied to generating B_0 only, and would need to be revisited for scanners that target high homogeneity over a competitively sized field-of-view.

Natural candidates for FOV projection are configurations that have a coil envelope of large diameter and small axial size, i.e. planar disk magnets. Figure 16 shows examples of embodiments proposed in such patents with a projected FOV (an example of anatomy-specific application for planar scanner with a small bore and partially projected FOV would be a dedicated breast imager). The low projected B_0 and poor homogeneity in these examples, as well the assistance of field-shaping ferromagnetic elements, are indicative of FOV projection limitations within the present NbTi He-based technology. Coil envelope challenges in such a planar geometry are exacerbated by the fact that the external space required for the gradient and RF coils would further take up part of the projected distance.

A different approach is considered in the Oxford Instruments patents (McDougall *et al* 2004, 2008). The system has a primary FOV in the bore of a traditional cylindrical magnet, complemented by a secondary external FOV. Additional FOV is created outside cylindrical magnet by adding 'bolt-on' magnets, either as a single disk or as a symmetric pair of disks mounted on both sides of the main magnet (figure 17). Managing inter-magnet forces, which are unbalanced in the unilateral version, and additional cryogenic circuits are among a few apparent challenges in such 'add-on' arrangements. The smaller secondary areas could be easier to implement, if one intends to use them for pre-polarization purposes that would require much less stringent homogeneity.

Enhanced internal access

Besides an external FOV, improved access has also been attempted in magnet designs where the imaging is performed between field generating elements. These are attempts to enhance internal space openness beyond that of the typical split-pole configuration.

In one example (McDougall *et al* 1992), a superconducting disk magnet with nested coils is complemented by two
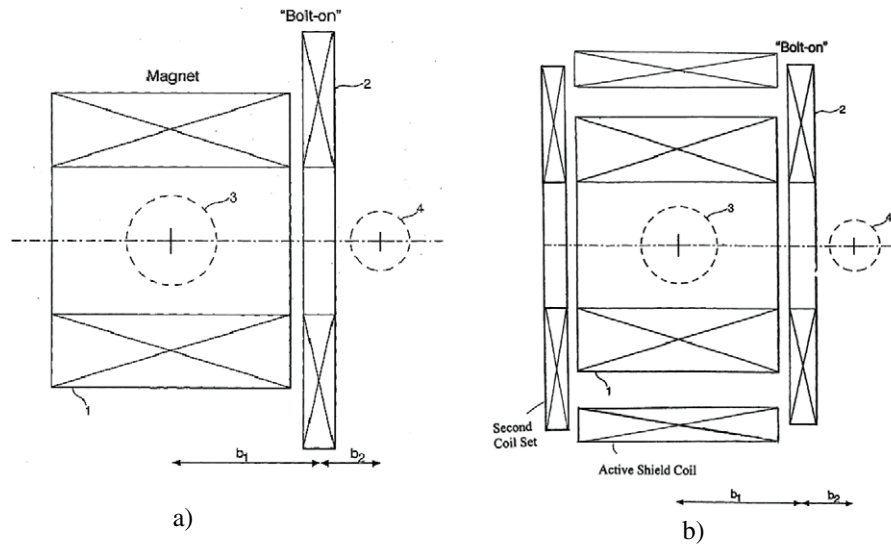
Figure 17. (a) Unilateral configuration (McDougall *et al* 2004) and (b) bi-lateral bolt-on configuration (McDougall *et al* 2008) with secondary external FOV regions.
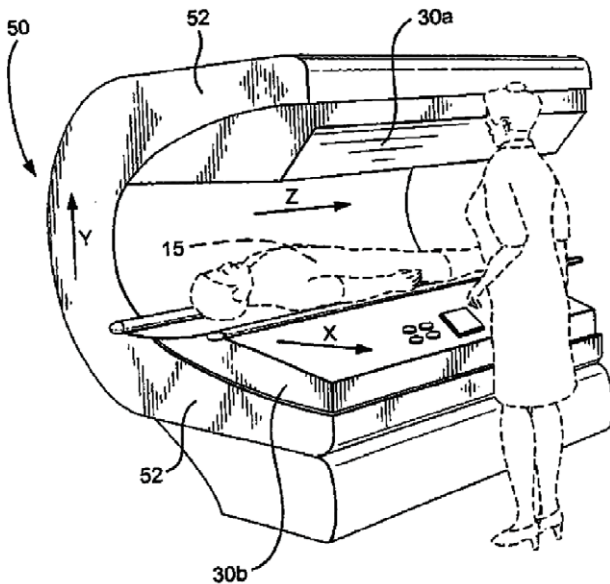

Figure 18. Suntan bed configuration using racetrack coils (Kruip 2004).

iron pole pieces mounted on opposite sides of ferromagnetic walls that provide a closed flux path, so that two symmetric imaging regions are created between the magnet and the walls. As in the previous examples, limited homogeneity (100 ppm p/p at 26 cm DSV) and substantial iron weight are among the drawbacks of such a iron-assisted design.

A different approach is proposed by OMT in the 'suntan bed' configuration illustrated in figure 18 (Kruip 2004). The magnet has two poles that contain racetrack coils, between which the patient is imaged. This is expansion of the present split-pole geometry, extending it in one direction.

Patient comfort during imaging in an elongated FOV that covers the whole body without the moving table comes here at a price of increased complexity and cost of the

design. Those include implications of managing the stresses in non-circular superconducting coils, which would be done either by lowering the operating current ratio I_{op}/I_{c} for a high stability margin to cover larger quench-causing movements in long sections and corners of the racetrack coils, or by adding a substantial coil-restraining structure. The large E_{stored} and magnetic moment have impact on quench and fringe field management, whilst extra superconductor length and the additional restraining structure create cost challenges in such a design.

Considering the limited present success in projecting the magnetic field for more open scanners, the question can be asked whether the traditional two-dimensionality of the axisymmetric coil design over-constrains the potential for openness, and whether a departure into a more complex 3D current topology could help find a better, more open solution. An example of an optimization study with an irregular 3D set of multiple planar coils was presented by Bertora *et al* (2012). Although such non-traditional 3D topologies inevitably create substantial challenges in coil structural support, and the stability and cryogenic arrangements are presently far from practical implementation, their exploration, especially with regard to future superconductors, presents an important direction in the continuing quest for openness.

Advantages of superconductors with higher T_{c}

Introduction of new high-T_{c} or MgB$_2$ superconductors can help overcome some of the challenges existing in non-traditional geometries. Among the features of HTS/MTS that are conducive to the discussed non-traditional designs are:

- Pancake HTS/MTS coils, which lend themselves naturally to the planar geometry of the disk magnets.
- The high stability of HTS and MgB$_2$ conductors considerably reduces the threshold for introducing non-circular coils, such as racetracks etc, by accommodating larger localized wire movements that produce higher
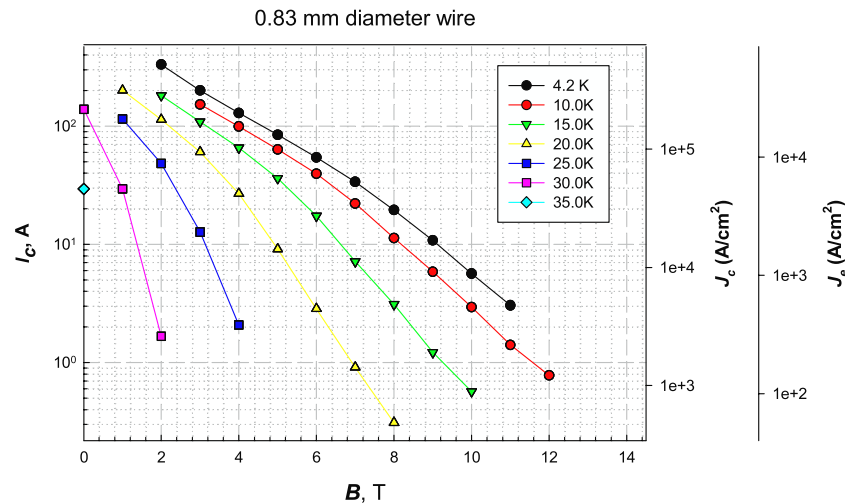
Figure 19. Typical dependence of MgB$_2$ critical parameters on field and temperature. Data for HyperTech multifilament 0.83 mm diameter carbon doped MgB$_2$ strand (Hyper Tech 2010).

frictional heat disturbances. The use of non-circular coils can provide better tailoring to non-standard FOV and envelope geometries (global coil displacements, however, would still require containment dictated by allowable strain limits in new superconductors).

- Higher stability can also eventually lead to reduced cost and complexity of the cryogenic system. Improvements could cover the range from non-helium cryogen-based magnets to convection- and conduction-cooled distributed cryogenic components, contrary to the present pool-boiling helium vessel.

All the above considerations facilitate the argument that the logical first candidates for new superconductors in MR would be specialty, or dedicated scanners, as the introduction threshold is smaller due to the smaller size, lower technical risks and cost, and the advantages of the non-traditional envelope for specific anatomy.

3.3. MgB$_2$ for MRI

3.3.1. Drivers for MgB$_2$ MRI. Superconductivity in magnesium diboride was first discovered in 2001 (Nagamatsu *et al* 2001). Over the past decade, since MgB$_2$ joined the family of superconductors, extensive efforts have been applied towards improvements in its technical parameters and manufacturability. Considerable progress has been achieved in terms of critical current density, upper critical field, and wire piece lengths, in a variety of wire/tape configurations. However, significant challenges—rooted both in technical and cost issues—still have to be resolved before MgB$_2$ can find wide use in commercial applications.

When compared with the existing LTS and HTS superconductors, MgB$_2$ occupies a specific domain in potential future applications. With the critical temperature $T_c \approx 39$ K, MgB$_2$ allows operating superconducting devices at cryogenic temperatures around 20 K. At the same time,

the strong field dependence of the critical current (e.g. see figure 19) limits its use at higher fields to helium temperatures. With the low cost of its chemical components, which points to potentially replacing current superconducting materials, NbTi and Nb$_3$Sn, the two workhorses for high-field and high-energy superconducting magnets, extensive research and material development has been conducted worldwide in universities and laboratories, in applications such as cryo-free accelerator magnets (Musenich *et al* 2008), superconducting wind turbines, for example Terao and Sekino (2012), MRI magnet systems (Mine *et al* 2012, 2013, Li *et al* 2009b, 2009a, Razeti *et al* 2008), fault current limiters (Ye *et al* 2007), for a general overview of applications, also see Tomsic *et al* (2007).

Increasing interest has been shown in MgB$_2$-based MRI magnets (Tomsic *et al* 2007, Hyper Tech 2010, Penco and Grasso 2007, Yao *et al* 2008, Modica *et al* 2007, Li *et al* 2007, Iwasa *et al* 2006) that fall into two categories:

(1) Low-field systems that operate helium-free at temperatures around 20 K. Helium-free MRI systems would improve access to high image quality superconducting MRI in under-served or underdeveloped regions, where the expense associated with liquid helium supply and service is extremely high, and the alternative would be heavy low B_0 permanent-magnet-based systems. A higher operating temperature also helps with the design of conduction-cooled cryo-free MRI magnet. The less costly cryocooler and much simplified cryogenic system can provide great potential savings in magnet construction, especially for the open MRI system that requires two separate cryostats, and other non-traditional topologies. Because MgB$_2$ has a higher temperature margin compared to NbTi or Nb$_3$Sn, MgB$_2$ composite superconductor can be constructed with less stabilizer, which potentially could increase the overall coil engineering current density J_e. Also, due to the highly enhanced heat capacity of materials at temperatures around 20 K versus 4 K, a MgB$_2$ MRI magnet would be extremely stable (practically 'quench-free'—Iwasa 2005), unlike the
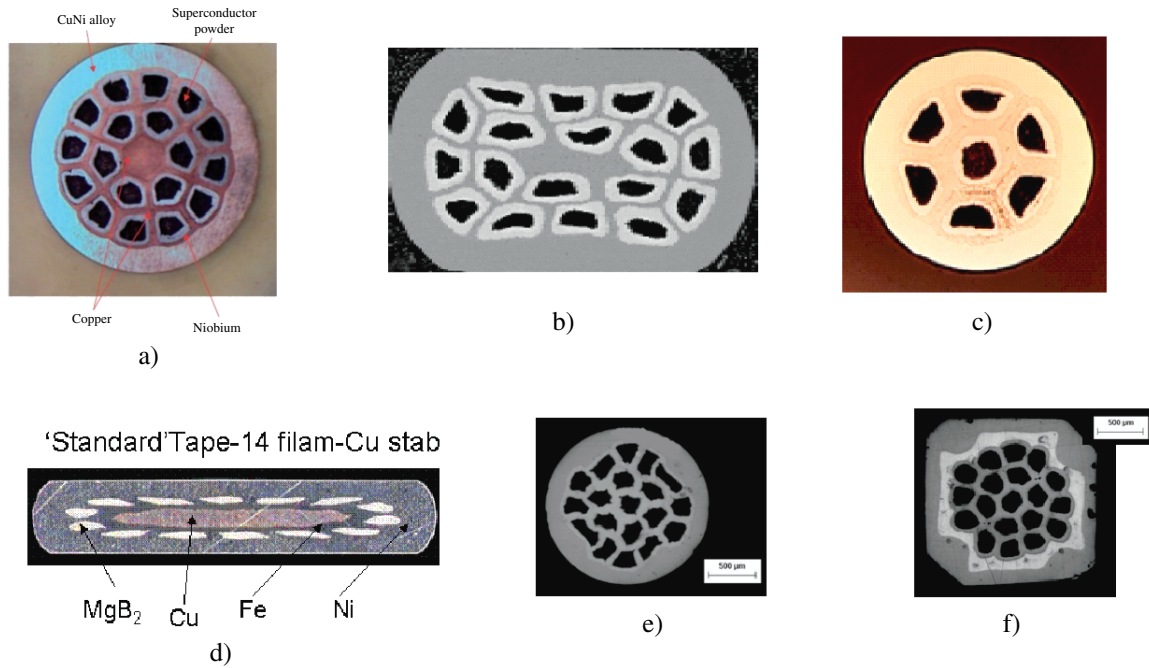
Figure 20. MgB$_2$ wire manufactured in various configurations, HyperTech (see Tomsic *et al* 2007): (a) '18+1' round; (b) 18-filament rectangular; (c) 7-filament round. Reproduced with permission of HyperTech. (d) 14-filament tape; (e) round and (f) square 19-filament wire, Columbus. Reproduced with permission of Columbus Superconductor.

conventional NbTi magnets. The significant drawback of the considered 20 K category is that it is limited to $B_{peak} < 2$ T. Such low B_{peak} limits MgB$_2$ applications to either low-field whole body scanners ($B_0 \sim 0.5$ T), or to the 1.5 T designs with a low B_{peak}/B_0 ratio that require sub-optimal solenoid-like coils and incur a substantial conductor penalty, which can be tolerated only in small size specialty MRI systems, such as orthopedic or head-only scanners;

(2) Higher field MRI magnets operated at 4.2 K. In this category MgB$_2$ faces direct competition from the well-established NbTi conductors and thus has to be both technically and cost competitive. Improvements in the short sample critical current density of MgB$_2$ (J_c recently close to 1.8 kA mm^{-2} at 4.2 K, 5 T for carbon doped wire (Hyper Tech 2010) bring it closer to the 3 kA mm^{-2} value of NbTi, while continuing improvements in conductor design and in powder-in-tube (PIT) manufacturing process are advancing its engineering critical current density $J_{c_{eng}}$. Since the basic material cost of Mg and B is less than that of Nb and Ti, the long-term trend is expected to make costs comparable or less than that of NbTi, once the remaining technical and production challenges are resolved through research and engineering efforts. An additional benefit of MgB$_2$ wire is its much higher quench stability due to the large temperature margin. That has the potential to translate into more aggressive and hence more cost-effective designs. The hope for MgB$_2$ wire is to replace NbTi or Nb$_3$Sn for mid- and high-field whole body MRI magnets (1.5 T, 3.0 T or higher). To achieve that, MgB$_2$ superconducting wires need more time to mature while targeting promising applications. One can recall the fact that NbTi now has a history of development and commercialization of over 50 years (www.superconductors.

org/History.htm) and MgB$_2$ wire can certainly benefit from this experience and lessons.

3.3.2. Conductor developments. Over the past decade, only a few companies have been active in producing MgB$_2$ wires for commercial applications, namely Hyper Tech Research Inc. (Columbus OH), Columbus Superconductors SpA (Genoa, Italy), EDISON SpA (Milano, Italy), Bruker/EAS GmbH (Hanau, Germany) and Grid Logic (MI, USA), as well as Hitachi (Japan) for company-internal use, for experiments at research centers at Karlsruhe Institute of Technology (KIT) (Stutensee, Germany) and MgB$_2$ precursor powder technology at the Leibniz Institute for Solid State and Materials Research (IFW, Dresden, Germany). The latest research, for example, shows that it is not entirely clear yet whether high-purity boron powder, one of the main cost drivers, is required. For Columbus Superconductors, however, boron purity is fundamental. Columbus uses 95% pure boron, but is striving to find reliable sources of industrial quantities of 99% pure boron that are tolerably priced (Grasso 2012).

HyperTech uses a patented process, so-called continuous tube filling and forming (CTFF) (Tomsic 2004). During this process, the powder is dispensed onto a strip of metal as it is formed into a tube, resulting in an overlap-closed tube filled with powder in continuous lengths. The *in situ* technique is primarily used by HyperTech, which involves direct filling of unreacted elemental magnesium and boron powder and subsequent drawing followed by heat treatment to form MgB$_2$ (Tomsic *et al* 2007). A multifilament round '18+1 Nb/Cu/Monel' wire currently offered by HyperTech (figure 20(a)) contains eighteen 76 μm MgB$_2$ filaments, Cu as the monofilament sheath, Nb as chemical barrier and with

a Monel multifilament sheath. This 0.8 mm wire has been produced in piece lengths up to 5 km (Tomsic *et al* 2007). The MgB_2 wire has also been fabricated in a rectangular shape (0.5 mm × 1.0 mm) in various multifilament strand designs.

Typical J_c and $J_{c_{eng}}$ measurements for standard multifilament MgB_2 conductor manufactured at HyperTech indicate $J_c = 0.9$ kA mm^{-2} at 5 T, 4.2 K, and 2.1 kA mm^{-2} at 1 T, 20 K. These numbers translate into corresponding I_c values of 80 and 200 A with a 15% MgB_2 fill factor in the multifilament strand; which produces engineering current densities $J_{c_{eng}}$ of 140 and 320 A mm^{-2}. Increasing the MgB_2 fill factor and boosting $J_{c_{eng}}$ by a factor of three is the key to make MgB_2 competitive with NbTi and bring it into commercial arena. By further improving powder, chemistry and wire architecture by employing an internal magnesium diffusion process a jump in $J_{c_{eng}}$ was recently published (Li *et al* 2012). The latest reported $J_{c_{eng}}$ by HyperTech and Ohio State is now 167 A mm^{-2} but at 10 T and 4 K.

Columbus Superconductors employs an *ex situ* PIT technique, using a Fe barrier against chemical diffusion into MgB_2. Their process involves filling metallic tubes with pre-reacted MgB_2 powder, followed by a drawing process. While the *in situ* technique claims several advantages, such as low cost, a high fill factor, a high-speed, low-temperature reaction process, and relatively easy particle doping, the above *ex situ* process is claimed to be better suited for long conductors and complex multifilament wire geometries. The standard Cu-stabilized MgB_2 tape manufactured at Columbus Superconductors, shown in figure 20(d), has a cross-section of 3.5 × 0.65 mm^2, with a copper core center (15% filling factor), surrounded by the Fe barrier (8%), followed by 14 MgB_2 filaments (10% filling factor), and a Ni sheath. The first long length sample of ~1.53 km was made in 2005. In 2006, the single length had reached 1.75 km, and the critical current increased to 210 A at 1.2 T and 20 K, equivalent to a critical current density of 1×10^5 A cm^{-2} (Penco and Grasso 2007).

In parallel with the efforts to optimize the manufacturing process, intense research activities towards reliable high critical current densities by both the *ex situ* and *in situ* process are being carried out. Some encouraging results are produced by: (a) addition of SiC nanoparticles to boron before reaction with Mg; (b) high-energy ball milling of MgB_2 powder alone; (c) high-energy ball milling together with the addition of SiC or C nanoparticles; and (d) densification of MgB_2 powder that improves its boundary with copper and increases the pinning force (Morawski *et al* 2011).

Columbus Superconductors recently made several manufacturing process improvements that led to better MgB_2 grain connectivity and increased critical current performance. A uniform particle size distribution is an important precursor as well as the availability of industrial quantities of tolerably priced 99% pure boron (Grasso 2012). Further details can also be found in Mine *et al* (2012, 2013).

Continuing on the optimization of the industrial manufacturing process, Flükiger and the Geneva team report on perspectives of a cold high-pressure densification process (CHPD) meant to densify a HyperTech type wire before reaction heat treatment to achieve a better grain connectivity (see Flükiger *et al* 2010).

3.3.3. Challenges remain.
Even though the first commercial MgB_2 MRI system with $B_0 = 0.5$ T, OpenSky is available now from Paramed (see Paramed website 2012), several key challenges have to be met before MgB_2 can move into a wider arena and contest the position now firmly held by NbTi in higher B_0, low-weight ironless persistent designs. The above-mentioned cost target of NbTi in piece lengths at least 1–2 km is the first prerequisite that needs to be tackled through the process developments (presently, it is the complex process, rather than the base materials, that defines the high wire cost). Besides, several technical challenges remain to be conquered:

I_c and n-value. Wire performance for commercial MRI applications has to meet the threshold of $J_{c_{eng}} \sim 300$ A mm^{-2} at 4.2 K, 5 T for high-field applications (250 A mm^{-2} @ 20 K, 2.5 T for low-field magnets). Stringent quality control process with doping and densification should limit the 'fluffiness' and eliminate voids and weak links, yielding consistent MgB_2 density and grain boundaries that will result in highly uniform and repeatable I_c values throughout multi-kilometer piece lengths. No sausaging or other variations can be tolerated, as the n value will be required in the range of 30+ for persistent designs that will pursue a higher I_{op}/I_c ratio, now being freed from stability limitations. Presently, some of the produced wires still exhibit inconsistent, varying n-values that are too low.

Magnetic components. The presence of magnetized components, such as Ni or Fe, in the wire cross-section would create specific challenges in MRI application. In the magnet design, driven by high field homogeneity, the moment distribution $\vec{M}(Z, R)$ throughout the magnet from the magnetized wire has to be accurately characterized and accounted for, especially for light air-core (ironless) magnets that are more sensitive to field variation in the coils. Manufacturing variations in conductor magnetization would impose an additional burden on the limited shimming capacity. Non-magnetic MgB_2 conductor configurations would have advantages in applications for MRI.

Persistent joints. For persistent mode operation with long-term drift <0.1 ppm h^{-1}, the total magnet resistance should be kept $\lesssim 10^{-9}$ Ω. In the magnet design, the largest portion of the resistance value is allocated to the joints; which translates into a resistance of 10^{-10}–10^{-11} Ω for each individual joint in the multi-coil design (Lvovsky and Jarvis 2005). The limit becomes lower if more individual pieces are to be used due to single piece length limitations.

Conventional NbTi-like superconducting joint techniques cannot be applied to MgB_2 conductor because of the brittle nature of MgB_2 filament and, for the 20 K applications, due to high operating temperature. It also has been found that, when heated to high temperature, MgB_2 decomposes into non-superconducting phases, such as MgB_4 and MgB_7 (Liu *et al* 2001, Baranov *et al* 2003, Cook *et al* 2005), so a traditional joint technique employing fusion process is not applicable. A MgB_2 persistent joint is thus considered as the most critical technical challenge for MR applications. Several studies have been conducted to develop such a technique. The first successful MgB_2–NbTi joint was reported in 2005 as having a resistance below 10^{-14} Ω at 4.2 K and

0.1 T (Takahashi *et al* 2006). Later in 2007, ASG claimed the development of the first MgB$_2$–MgB$_2$ joint. Although the joint resistance itself was extremely low (estimated $<10^{-14}$ Ω), the current carrying capacity was rather poor (only 10 A at 20 K, 1 T, or 40 A at 20 K, self-field) (Penco and Grasso 2007). Considering the wire itself carries 210 A at 20 K, 1.2 T, the joint performance has to be much improved to make it applicable. Most recently, Iwasa's group at MIT reported their achievement of making a superconducting joint for MgB$_2$ round wires (Yao *et al* 2009). By using unreacted Mg + 2B powder mixture as the flux, they were joining both reacted and non-reacted multifilament MgB$_2$ wires. The best result achieved by this technique showed $I_c = 200$ A at 10 K, self-field for non-reacted wires. However, for the reacted wires, the joints were not able to carry any current at 10 K, though it did carry 150 A at 4.2 K. Quite recently, the MIT team reported progress on joints using non-doped HyperTech Monofilament wires. By measuring the field decay rate of a small test coil, a joint resistance of less than 10^{-12} Ω was registered (Park *et al* 2012). The challenge remains in transferring the technique from a solitary filament into a process that joins multifilament wires.

Despite significant progress made for MgB$_2$ superconducting joints, none of them has yet demonstrated a reliable repeatable method to meet the technical requirements for MR magnets. Several patents have been filed on this topic (see e.g. Oomen *et al* 2011, Doll and Tomsic 2010, Kodama 2012, Nardelli 2009a, 2009b, Morita *et al* 2005, Aubele *et al* 2010a, 2010b, Tenbrink *et al* 2010). A suitable process still needs to be found that allows joining separate coils during the winding process in the factory environment, which may require joints to undergo thermal treatment alongside a full magnet cartridge with already wound coils.

However, the singular challenge of persistent joints should not hold back the development of MgB$_2$-based MR systems (Mine *et al* 2012, 2013). One alternative to having persistent joints is the use of a flux pumping method to compensate for a slow current decay in the magnet circuit, which as suggested by some studies, can be effective without inducing significant current ripples when the total resistance is low enough ($\sim 10^{-8}$ Ω). When the circuit resistance is even higher, a highly stable external power supply has to be used, with a resistive link added to the switch circuit to filter out the current ripples. Each of the two above alternatives has its associated technical and cost penalties, not discussed here in detail.

Wire handling and winding. The irreversible strain limit ε_{irr} of MgB$_2$ wire has been measured by NIST (Tomsic *et al* 2007). It is found that ε_{irr} increases with the number of filaments in the wire, and therefore reduction of filament size improves the strain tolerance of the conductor. For example, the strain tolerance limit reported is 0.37% for a 7-filament conductor, 0.40% for a 19-filament conductor, and 0.48% for a 37-filament conductor. This limit dictates a strict minimum-bending-diameter requirement for the wire and strongly affects the winding process; ideally one would stay well below this reported limit. Also, for tape shaped conductors, edge-wise bending can easily cause damage

or degradation of performance (Mine *et al* 2012, 2013). Therefore, the coil former and components for wire routing and joints have to be carefully designed to minimize any sharp bending, which may require extra space, and the potential impact on magnet dimensions and patient space needs to be carefully considered. The winding tension has to be controlled carefully during the process so as not to exceed the critical strain limit of the wire.

Stability and quench protection. Stability and quench protection are two critical issues in MRI magnet design and operation. An appropriate stability margin needs to ensure reliable operation of the magnet without quench, and an adequate quench protection is required to prevent permanent magnet damage from overheating, high internal voltage or overstraining. With regard to stability and quench protection, MgB$_2$ shares basic traits that differentiate HTS conductors from their LTS counterparts. The higher temperature margin $T_c - T_{op}$ and increased enthalpy affords good stability against disturbances in the coil, as a relatively high energy is required to initiate a quench. In adiabatic windings, the minimum quench energy MQE that represents bifurcational value required to start a minimum propagating local normal zone (MPZ) in the conductor, is proportional to the expression (Dresner 1995):

$$A \frac{h(T_c) - h(T_{op})}{J_{op}} \sqrt{\frac{k(T_c - T_{op})}{\rho}} \qquad (6)$$

where A and k are the conductor's cross-sectional area and thermal conductivity; T_{op} and T_c are the operating and critical temperatures of MgB$_2$ conductor; h is the enthalpy per unit volume; J_{op} is the operating current density over the conductor cross-section; ρ is the average normal resistivity of conductor matrix. The above dependence underscores the high sensitivity to an increased temperature region (with $h(T) \sim T^4$ at helium temperatures), as well as to the current density in the coil, which is so far lower than that in NbTi windings.

Stenvall *et al* studied details of the stability of multifilamentary MgB$_2$ tape with copper stabilizer. In his study (Stenvall *et al* 2006), a computational model was created to calculate basic stability characteristics, including the minimum propagation zone (MPZ), the minimum quench energy (MQE) and the normal zone propagation velocity at different temperatures (15, 20 and 25 K). According to this study, the MQE of MgB$_2$ tape with varying I_{op}/I_c ratios ranged from ~ 200 to 600 mJ, both for 4.2 and 20 K applications—a substantial increase in stability and hence level of tolerable mechanical disturbances from NbTi magnets having a MQE of the order of 10 mJ.

A large stability margin of MgB$_2$ coils makes many traditional sources of disturbance, such as wire micro-motion, flux jump, and epoxy cracking, unlikely causes of quench. However, the magnet still has to be reliably protected should quench occur due to excessive AC losses, loss of cooling or any other unforeseen event. As always, high stability spells a challenge for the quench protection due to slow normal zone propagation. The velocity of the normal zone front scales as
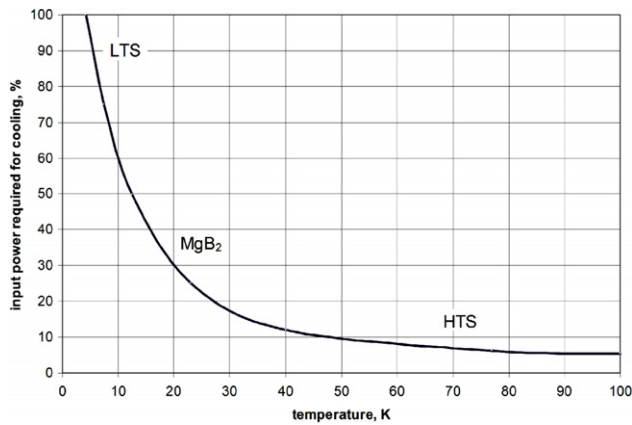
Figure 21. Input cooling power in per cent of requirements at 4.2 K versus temperature (Gieras 2009). Copyright 2009 Springer.

Figure 22. 0.5 T OpenSky MR scanner by Paramed; the conduction-cooled magnet uses MgB_2 conductor. Reproduced with permission of Paramed.

the expression (Wilson 1982):

$$v = \frac{J_{\rm op}}{h(T_{\rm c}) - h(T_{\rm op})} \sqrt{k\rho(T_{\rm c} - T_{\rm op})} \qquad (7)$$

and thus has strong slowdown with higher enthalpy and lower $J_{\rm op}$. With a slowly propagating front, the hot spot temperature in the center of the normal zone can grow uncontrollably (Lvovsky 2002) before the initial zone can be detected and spread by heaters throughout the magnet to evenly dump the large stored energy. The normal zone velocities calculated in Stenvall *et al* (2006) for a standard multifilament MgB_2 strand varied from 5 to 80 cm s^{-1}; an experimental investigation performed by Cavaliere *et al* (Cavaliere and Matrone *et al* 2008) in a conduction-cooled test magnet made of nickel matrix copper-stabilized MgB_2 multifilament tape showed velocities from 40 to 80 mm s^{-1} (depending on the temperature and bias current). Compared with the typical velocities of 10–50 m s^{-1} for NbTi at 4.2 K, such slow normal zone propagation presents a significant challenge for protecting the magnet in the case of quench. In an example of a 0.5 T MgB_2 magnet, it may only take ∼1 s for the conductor hot spot to reach temperatures above 300 K. Both conventional voltage-driven passive protection and active protection techniques should be explored to accelerate the normal zone propagation by activating a set of protection heaters. However, the resistive voltage of the initial normal zone is very low and thus will require special sensitive voltage detection, as well as a sophisticated quench protection circuit design.

3.3.4. Advanced cryogenic cooling technology. For a 20 K low-field MgB_2 magnet, simplified conduction-cooled cryogenic systems can be employed. In this case, the magnet is cooled by a cryocooler requiring a uniform temperature distribution through the magnet winding, and in particular in the radial and axial direction. The thermal interfaces between the cooling source and the coils have to be adequate and materials need to be properly selected and designed to distribute cooling effectively amongst individual coils. A coil former providing strong structural support and ideally

matching the physical and mechanical properties of the wire is essential for this type of cryo-free magnet. The development of a fiberglass-reinforced-polymer (FRP) coil former with a copper filament co-wound with the fiberglass has been reported to increase the thermal conductivity in both the circumferential and axial directions (Stautner *et al* 2009a).

One disadvantage of the conduction-cooled MRI magnet is its limited ride-through capability. When the cooling system is interrupted due to a power outage or regular maintenance/service, the magnet will quickly warm up, since most of the materials exhibit only a very low heat storage capacity at cryogenic temperatures. To prevent the magnet from quenching which would then lead to a long recovery time for subsequent re-cooling and re-ramp, the magnet has to be ramped down during the power outage. In order to extend this ride-through capability, a 'thermal battery' can be used in the magnet cooling system. Iwasa's group at MIT proposed using solid nitrogen as a solid heat capacitor to improve the MgB_2 magnet's ride-through capability (Yao *et al* 2008). However, the hold time offered by solid nitrogen is still significantly less than what may be achieved with an equal volume of liquid cryogen, such as helium and hydrogen. Since MgB_2 is still superconducting at LH_2 temperature around 20 K, using LH_2 in a closed loop heat pipe or thermosiphon system enables a low-field MgB_2 magnet to operate with a reasonable temperature margin as well as a longer ride-through time due to the very large latent heat of hydrogen (see also section 5.5 on hydrogen cryogenics). For example, a small liquid hydrogen reservoir of 0.25 l is necessary to provide 3 h ride-through for a parasitic heat load of 0.6 W. This concept has been successfully demonstrated at GE, but with a closed loop neon thermosiphon system for a BSCCO type magnet (Stautner *et al* 2007). For a high-field MgB_2 MRI magnet operating at 4.2 K, the same cooling principle can be employed, using liquid helium as coolant (Stautner *et al* 2013).

Figure 21 shows the benefit of MgB_2 on the percentage of required input power to work at a target temperature of e.g. 20 K (Gieras 2009).

Figure 23. 0.5 T MgB$_2$ magnet, made by ASG Superconductor for Paramed OpenSky MRI scanner. Reproduced with permission from Modica *et al* (2007). Copyright 2007 IEEE.

Table 3.2. Parameters of the ASG MgB$_2$ magnet used in the Paramed OpenSky MRI system.

Parameter	Unit	Value
Geometry	—	Split-open, horizontal axis
Patient gap	cm	58
Operating temperature	K	18
Central field, B_0	T	0.5
Peak field B_{peak}	T	1.3
5 G line	m × m	4 × 4
Operating current	A	90
I_{op}/I_c	—	23%
Number of coils	—	2
Windings	—	Double pancakes, R&W
Number of DPs, each coil	—	6
Coil ID	m	1.3
Coil OD	m	1.6
Total conductor length	km	18
Superconductor	—	14-filament MgB$_2$ tape
MgB$_2$ tape dimensions	mm × mm	3.6 × 0.65
Inter-turn insulation	—	Glass-epoxy impregnated
MgB$_2$ joints	—	Resistive
Current leads	—	Embedded hybrid, with second stage Bi-2223/Ag
Magnet dimensions	m × m × m	2.0 × 2.0 × 2.4
Magnet weight	ton	25

3.3.5. OpenSky, a 0.5 T MgB$_2$ MRI scanner. The first commercial MgB$_2$-based scanner has been in production by Paramed (Genova, Italy) (figure 22) with a magnet by ASG Superconductors (figure 23).

The magnet uses MgB$_2$ tape from Columbus Super-conductor, and is conduction-cooled and powered by a high-stability DC power supply. Its key design parameters are summarized in table 3.2 (Razeti *et al* 2008, Modica *et al* 2007).

Some choices and limitations in this magnet design reflect the yet unsolved MgB$_2$ challenges discussed above. Non-persistent joints lead to the expense of a high-stability DC power supply; I_c limitations require a lower B_0; the limited *n*-value translates into a low I_{op}/I_c ratio and affects the conductor cost; dimensional positioning accuracy and stress limitations of the MgB$_2$ tape are accommodated in the iron core design, which result in a heavy magnet. These are apparent improvement targets for MgB$_2$ magnets of the next generation of MR scanners.

3.4. HTS application to MRI

3.4.1. HTS challenge. Since the discovery of high-temperature superconductors, a natural expectation has always been that they would be utilized in MR as the largest commercial application. With the early emergence of BSCCO, and now with the development of YBCO-based second generation (2G) conductors, the hope was that HTS

will become an enabling factor that will bring a more efficient, autonomous magnet design with less restrictive cryogenic options, together with drastically improved coil stability.

However, on its way to commercial use, HTS MRI has yet to resolve serious challenges. In many aspects it shares, and often amplifies, the outlined difficulties with MgB$_2$ MRI. The two-pronged challenge is rooted both in high cost (as defined via I_c in $ per kA m), and in yet-unresolved technical issues.

Critical parameters. Whilst having an upper critical field B_{c2} that reaches well above 100 T, high-temperature superconductors are limited by a low irreversibility field B_{irr}, which corresponds to the onset of a dissipative flux flow regime with ineffective pinning and moving vortices that generate heat. The low values of the concave irreversibility line $B_{irr}(T)$ above 70 K do not permit the creation of LN$_2$-cooled MRI with 1 G BSCCO-based conductors (Wilson 2012). That leaves BSCCO with the two MgB$_2$-like choices, i.e. either low-field MRI at 20–40 K, or helium-cooled magnets. The substantially higher B_{irr} of the 2 G YBCO due to its better coupling between CuO$_2$ planes improves its promise in MR.

The critical current density J_c is limited by weak links at the inter-grain boundaries. Whilst a reasonable intra-grain J_c is delivered by flux pinning, the more than an order of magnitude lower local inter-grain J_c can result in an overall lower, and sometimes inconsistent I_c. Precise grain alignment within a few degrees becomes key for a successful

HTS conductor. Sensitivity to grain misalignment has to be overcome by a complex manufacturing process. This is done by controlled deposition on a substrate with an aligned structure, using an involved multi-step process, which increases the conductor cost as it no longer defined just by the component material cost.

Conductor cost. The high cost of HTS is a substantial impediment to its MRI application, especially in whole body MRI where conductor is the major cost contributor. Compared with the present Bi2212 at ~$100 kA^{-1} m^{-1} (at 4.2 K, 12 T), the HTS cost has to be eventually reduced by at least an order of magnitude before it becomes a viable candidate for commercial MR (cf Nb$_3$Sn conductors at $5 kA^{-1} m^{-1} for 4.2 K, 12 T, and especially NbTi at $1.5 kA^{-1} m^{-1} for 4.2 K, 5 T) (Wilson 2012). Unlike in other SC devices (for example, in FCL), where the total cost breakdown of the cryogenic and structural components versus conductor is different, it is difficult to absorb the high-cost burden of HTS in MRI magnets even when it is offset by the savings in cryogenics.

Stress limitation. In contrast to NbTi magnets, where stability constraints impose stress limitations in the magnet design in order to avoid quenches caused by epoxy micro-cracking or coil movements at the interfaces, the high stability of HTS allows the accommodation of unusually large disturbances. However, unlike ductile NbTi, the brittle nature of HTS oxides makes them sensitive to the level of strain in the coil, therefore tight stress control has still to be imposed in HTS coils to avoid I_c degradation. This is done by incorporating structural elements, such as steel strips, either within the conductor matrix or the coil structure. Either approach dilutes J_e in the HTS winding.

Reliable manufacturing. It is critical for the manufacturing process of HTS MRI conductor to dependably produce kilometer lengths with consistent I_c and *n*-value throughout each piece. Continuing improvements in the current advanced manufacturing methods are making progress towards this goal (Selvamanickam *et al* 2011). However, much still remains to be done, especially regarding inconsistency of parameters that can easily cause a magnet to fail due to a single degraded spot.

Persistent joints. HTS faces the same challenge as MgB$_2$ in regard to persistent design. A practical method has yet to be found for persistent joints, considering the brittle nature of the HTS filaments and the potential need to employ a process that may involve heat treatment (W&R) on the joints only during assembly of the already wound HTS coils. Non-persistent design alternatives exist; they are the same as described above for MgB$_2$ magnets and therefore are not repeated here.

Quench protection. The large temperature margin due to the high T_c and high enthalpy of the wire required to propagate a normal zone makes quench detection in HTS particularly challenging. As the normal zone front propagation slows down even further compared with MgB$_2$, while its crest exhibits uncontrollable temperature growth, the danger of damage during quench becomes a serious consideration in the magnet protection. The challenge of timely detection will also increase with advances in J_e in future commercial HTS coils. Additional considerations pertain to conduction-cooled magnets where in some regimes even a low level nonlinear index loss may result in an uncontrollably growing temperature profile that requires timely detection and initiation of protection measures (Lvovsky 2002).

3.4.2. Siemens/OMT—the world's first 0.2 T whole body HTS MRI magnet. The first whole body HTS MRI development was based on a BSCCO-2223 C-shaped prototype magnet. It presents a revealing example of how quickly the technological landscape changes during development, and why market requirements need to be carefully watched in a technology-driven development.

In early 1996, Oxford Magnet Technology (OMT) (now Siemens Magnet Technology) and Oxford Instruments (OI), together with Siemens CT Erlangen, kicked off a project aimed to replace an existing NdFeB, C-shaped 0.2 T MRI magnet with the newly available BSCCO-2223 tape conductor from VAC and NST.[4]

At the time, C-shaped permanent magnets from major MRI manufacturers, such as Hitachi (Airis, 0.3T), Picker (Outlook, 0.23T), GE (SIGNA Profile, 0.2T), and resistive Siemens (Viva, 0.2T) (Kettenbach *et al* 1999) already had a reasonable production volume, resulting in considerable market saturation for low-field applications. The open geometry low-field NdFeB-based MRI systems typically weigh in excess of 10 ton, which limits their siteability. The Siemens Magnetom Open Viva MRI scanner with a 0.2T Oxford OR10 resistive magnet (Byrne *et al* 2001, NCD Medical 2012, Orbitmed 1998) had the following specifications:

- 15 mT m^{-1} power gradients.
- Coils: CP head, CP body/spine with four sizes of insert (37, 43, 49 and 59 in).
- Multi-purpose coils: 16, 21, 35, and 45 cm.

The basic resistive 'Viva' magnet weighed 12 metric tons in its operational configuration; the patient gap was less than 40 cm. The 5 G line extended 8 feet 6 inches in front of the magnet and 7 feet 10 inches in all other directions.

The Viva test bed and technological demonstrator, described in detail in the following, are interesting from a number of perspectives. The project goal was to show the feasibility of MRI-sized HTS coils and their ability to produce the required magnetic field strength. The use of HTS tape, it was claimed, potentially leads to higher fields and would be competitive with NdFeB technology. Furthermore, it gave an excellent opportunity to learn the technical, manufacturing and winding issues associated with HTS tapes.

Selected design options were limited by technological restrictions, many of which still apply today. The low $B_0 = 0.2$ T is limited by the performance of BSCCO in higher fields; the absence of a persistent joint technology forced the use of stabilized power supplies; the heavy iron yoke which is applicable to low B_0 designs, reduces the amount

---

[4] VAC former Vakuumschmelze (now Bruker Energy and Supercon Technologies) and NST Nordic Superconductor Technologies.

Table 3.3. Magnet design details.

Comparison	Siemens coil	Oxford coil
HTS tape manufacturer	VAC BSCCO-2223 Ag	NST BSCCO-2223 Ag
Tape $w \times h$ (mm)	19 filaments, 2.8×0.2	55 filaments, 3.6×0.26
Design criteria for I_c	27 A (77 K, 0 T)	15 A (77 K, 0 T)
Operating current (A)	74	49
Coil[a] I_d; O_d, H (mm)	804, 844, 49	804, 844, 49
Peak field B_{peak} (T)	1 (at winding)	1 (at winding)
Number of turns	660	972
No. of pancake coils	10	12
Conductor length (m)	1700	2500
Type of insulation	Kapton	Nomex and Mylar
Eng. curr. density (A mm^{-2})	50	
Patient access gap (cm)	46	
Pancake coils sandwiched between iron rings (X8Ni9)	1 T parallel, 0.1 T perpendicular to tape	
Max hoop stresses (MPa)	4	

[a] Inner I_d and outer O_d pancake diameter and height H.

Table 3.4. Cryogenic design details.

Comparison	Siemens coil	Oxford coil
Vacuum chamber design	All-welded	O-ring seal
Leybold cryocooler, orientation	Horizontally	Vertically, cold end up
Cooler (heat bus to pancake link)	RGS 120 T, horizontal	RGS 120 T, cold end up
120 A CL heat loads (W)	HTS from RT, 7.2	Brass lead from RT, 5
HTS tape soldered contacts (W)	<0.1	<0.1
HTS tape, @ 0.1 μV cm^{-1} (W)	1.4	1.4
Thermal radiation at 22 K (W)	2.5	2.5
Thermal radiation black holes (W)	1	1
Suspension type/heat load (W)	8 SS rods, 3.8	8 CFC struts, 0.4
Cooling	1 Cu sheet/pancake	1 Cu sheet/pancake
Thermal shield (—)	MLI only	MLI only
Total heat load (W)	16	10.3
Operating T (K)	16	20
Cooldown time (h)	21	24

of superconductor compared with the air-core magnets, as well as relaxes the dimensional requirements for coil and conductor positions in a homogeneous magnet—however, it creates a weight penalty when compared with the air-core NbTi magnets.

The approach of the two poles of the C-magnet was different. The lower pole magnet and cryostat was manufactured and pre-assembled at Siemens (Germany). The magnet for the upper pole was designed and wound in collaboration with OI, while the cryostat design, manufacture and assembly was done at OMT. Both cryostats were then fitted into the existing C-shaped frame.

Tables 3.3 and 3.4 compare magnet and cryogenic design aspects.

Known HTS design issues were the low strength of the BSCCO/Ag conductor of 20 MPa, resulting in a winding tension of 5 N. Besides that, as with every other magnet, the C-shape configuration imposed an additional challenge to keep vibration levels low enough for imaging.

A ΔT of 3 K from the heat bus to the hottest magnet location was tolerable. This was possible by adding extra copper cooling sheets between the individual pancakes and by direct cooler to heat bus contact (see figure 24).
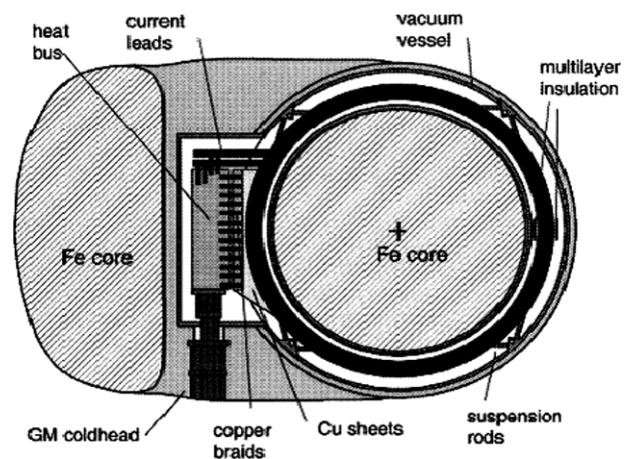

Figure 24. Horizontal cut through cryostat lower pole; cryocooler bolted to heat bus (Steinmeyer *et al* 2002, Byrne *et al* 1999). Reproduced with permission from Byrne *et al* (1999). Copyright 1999 IEEE.

Figure 25 shows both magnet halves assembled and ramped to a field of 0.1934 T ($\pm$20 ppm) over a 36 cm sphere. Because of persistent current limitations caused
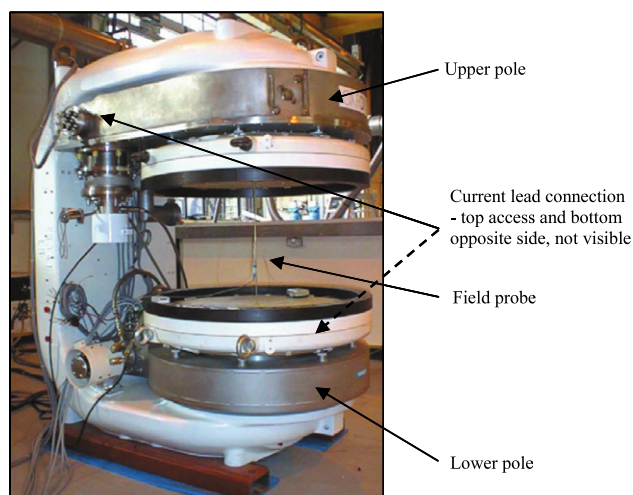
Figure 25. Assembled 0.2 T C-magnet. HTS magnet shown with upper and lower pole, cryostat and attached cryocoolers with motor shielding, upper pole by Oxford Magnet Technology, lower pole by Siemens. Reproduced with permission from Marken (2004). Copyright 2003 Oxford Superconducting Technologies.
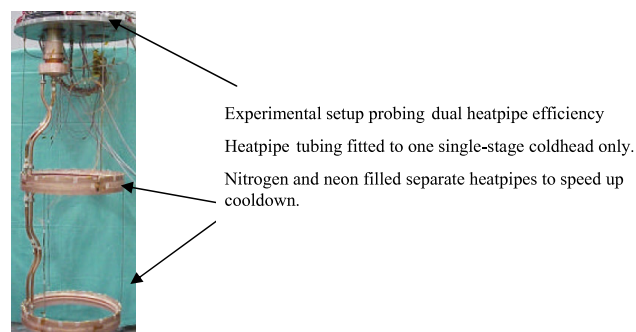

Figure 26. Dual heatpipe technology (Rieger 2004, Oomen *et al* 2006). Reproduced with permission from Rieger (2004). Copyright 2004 IEEE.

by the BSCCO joints, two stable power supply units were required and permanently connected to the current leads. Based on a successful experimental demonstration of feasibility, the program subsequently expanded and involved other companies and research institutions (OST, LANL, SCI Engineering Materials, NREL), aiming to replace BSCCO-2223 with the more cost efficient BSCCO-2212, and at an even later project stage to introduce the next-generation YBCO-based superconductor.

However, by the time the new low-cost BSCCO-2212 tape was available and its performance confirmed by the test results (OST) (Marken *et al* 2004), the commercial perspective was re-assessed due to poor return on investment and the continuing market push towards higher field strengths. Continuous cost improvement in tubular NbTi MRI magnets, with $B_0 = 1.5$ T and higher, undermined the competitiveness of heavy, low-field permanent configurations. The management team agreed to end the project in July 2004, concluding the following:

- A 0.2 T magnet requires 400 kA m of HTS conductor.
- A 0.6 T magnet would require >3000 kA m, based on an existing (similar) design.
- Designs must operate at >26 K for a stable, cost-effective cryogenic solution.
- Target conductor cost must be: $5–$10 kA^{-1} m^{-1} (defined @ 27 K, 0.6 T) to be considered for commercial MRI applications.
- Expected HTS tape cost was estimated as $75 kA^{-1} m^{-1} (at 27 K, 0.6 T).

Further use of optimized cryogenic test beds. Progress on cryogenic cooling of C-shaped pancake coils has recently been reported. The main shortcomings of the previous design, i.e. a long cooldown time from room temperature, the high ΔT across the coil perimeter, as well as previous high vibration

sensitivity, were addressed by introducing dual-stage heatpipe technology (figure 26).

Once a temperature below 77 K is at obtained at cooldown, only the neon heatpipe continues to operate. Employing heatpipe technology reportedly reduced cooldown time by a factor of two.

With the arrival of MgB$_2$ superconductor available in continuous lengths >1000 m, this test bed may offer the opportunity for further use (more information can be found in Rieger (2004), Byrne *et al* (2001), van Hasselt (2007)).

3.4.3. Second generation YBCO MRI conductors—development status and parameters. The discovery of superconductivity in YBCO ceramic in 1987 started considerable research and development activities in that field. The relatively high critical temperature of ~93 K, above the boiling temperature of LN$_2$ of 77 K, opens up possibilities for numerous applications in magnetic, electronic and power technologies. Compared to BSCCO, which represented the first generation of HTS, the requirements for fabricating YBCO conductor are much more stringent. However, YBCO has quickly become the most studied high-temperature superconductor and is believed to hold promise for a broad range of commercialization, mainly due to the following two factors. First, the raw materials cost of YBCO is intrinsically lower than BSCCO due to the absence of a silver matrix. With the improvement in fabrication technology and volume, it potentially enables YBCO to achieve a cost target of ~$10 kA^{-1} m^{-1} (cf copper at $4 kA^{-1} m^{-1}, but limited to lower J_{ave} (Wilson 2012)). Second, despite the lower critical temperature, i.e. ~93 K versus 110 K for Bi-2223, the YBCO in-field current carrying performance is substantially better than that of BSCCO. Therefore a YBCO magnet at a reasonable B_{peak} can be envisioned operating in the 20+K range.

Over the 20 years since its discovery, considerable progress has been made in YBCO coated conductor development and its manufacturing technology. In the earlier stages, the main efforts were focused on improving I_c and the continuous conductor length. In 2008, the 1 km single piece length threshold was crossed, and a record of more than 200 000 A m was established by SuperPower, Inc (Xie
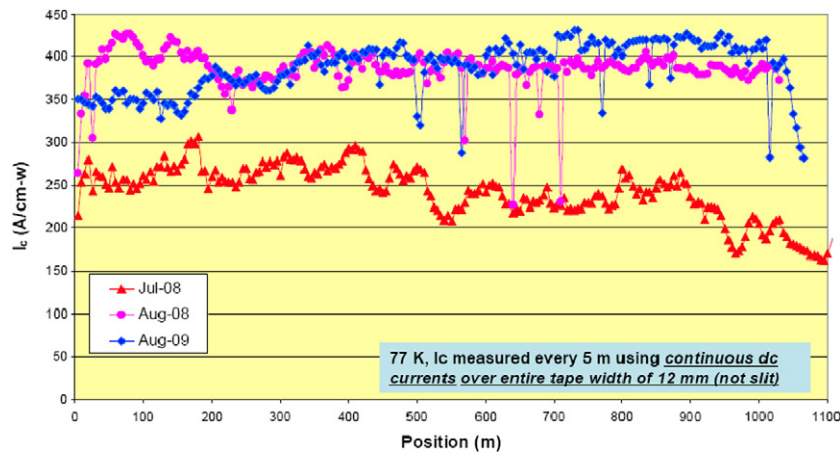
Figure 27. Critical current distribution over the wire length (self-field at 77 K). Reproduced with permission from SuperPower Inc.

et al 2009); presently its wire is produced in kilometer piece lengths. More efforts have also been applied to develop new conductor structures and configurations with improved performance in thermal stability, mechanical properties, ac loss characteristics, etc, as driven by application needs. Recent developments have extended the potential of YBCO to a wider range of applications, including HTS cable, SFCL, superconducting generators and motors, SMES, maglev, magnetic bearings and more.

YBCO conductor manufacturers targeting commercialization-scale applications are SuperPower, Inc (Schenectady, NY) (now taken over by Furukawa), Fujikura, Bruker EHTS, SMI, STI and American Superconductor (Devens, MA). SuperPower fabricates YBCO conductor on biaxially-textured buffers based on ion beam assisted deposition (IBAD) of MgO on a high-strength Hastelloy substrate, followed by YBCO deposition by metal organic chemical vapor deposition (MOCVD) (Selvamanickam *et al* 2009). The key challenge is to achieve high-quality, epitaxial, near-single-crystalline films with uniform properties over kilometer lengths without defects. To meet this challenge, a robust manufacturing process has been established and several kilometer-long YBCO conductors have been produced at SuperPower. Figure 27 shows the I_c along the wire as measured using continuous dc transport current over the entire wire width of 12 mm and using a voltage criterion of 0.2 μV cm^{-1} (Selvamanickam *et al* 2009). In the wire made in July 2008, a minimum I_c of 200 A cm^{-1} was achieved over 945 m. In Aug. 2009, a 1065 m long conductor was made with an I_c of over 320 A cm^{-1} for most of the wire, except for only three locations with minimum I_c of 282 A cm^{-1}. This indicates a significant improvement from the 1030 m long wire made in Aug. 2008, which had a minimum I_c of 227 A cm^{-1}. Nevertheless, in spite of the substantially improved average I_c, its distribution in long conductor lengths still suffers from occasional weak spots, as is evident in figure 27.

In addition to efforts aimed at a continuous increase in I_c over long piece lengths, a multi-pass technique has been employed to fabricate thick films of YBCO. One of the methods adds 5% Zr to the precursor of (GdY) BCO and doubles the number of passes. A higher critical current level,

803 A cm^{-1}, was achieved in films of up to 3.5 μm. So far, such a high-performance manufacturing technique can only be made and repeated over a short length of ∼1 m.

For practical magnet applications, the in-field performance is what really matters, and $B_{peak} = 5$ T can be taken as a typical figure-of-merit for a whole body MRI magnet. Figure 28 shows the characteristic in-field performance for a standard copper-stabilized SmYBCO tape by SuperPower. The I_c drops abruptly with the applied field, except at very low temperatures (for example, at 77 K, the I_c at 3 T is only 4% of that at self-field). With such characteristics, the operating temperature would have to be reduced in MR magnet design, except for the limited low-B_0 niche. That would imply, however, forfeiting the critical benefit of YBCO of being able to operate in liquid nitrogen (65–77 K) with a much simpler and more reliable cryogenic system. Therefore improvement in the in-field performance of YBCO in the liquid nitrogen range is paramount for its use in MR. SuperPower has developed a Zr-doped GdYBCO composition, which exhibits a significant enhancement in I_c (see figure 29). The in-field I_c at 77 K and 1 T is about 2.5 times higher than that of the standard SmYBCO sample and twice as high as GdYBCO (Selvamanickam *et al* 2009). Similar improvements have been achieved for both thin film (0.7 μm) and thick film (∼3 μm) samples. Recent test results showed a consistent improvement of in-field performance by Zr-doping (2× compared to standard SmYBCO composition) over a 610 m long tape.

AMSC takes a different approach, RABiTS/MOD technology, and a 'wide-strip' process to manufacture its YBCO conductor (Li *et al* 2009b, 2009a). The standard product, called 344 superconductor, is a 4 mm wide tape conductor consisting of a NiW metal alloy substrate, a buffer layer, a doped layer of 0.8 μm YBCO and capped with a thin Ag layer, and finally a stabilizer strip (copper, stainless steel or brass). In 2008, AMSC demonstrated a commercial-scale manufacturing process and equipment, producing a 100 m long 344 superconductor with a minimum I_c (77 K, self-field) of 105 A (262 A cm^{-1}) over the entire length. It is projected that I_c will reach 375 A cm^{-1} when thicker (1.4 μm) YBCO film is incorporated. It is also predicted that the final
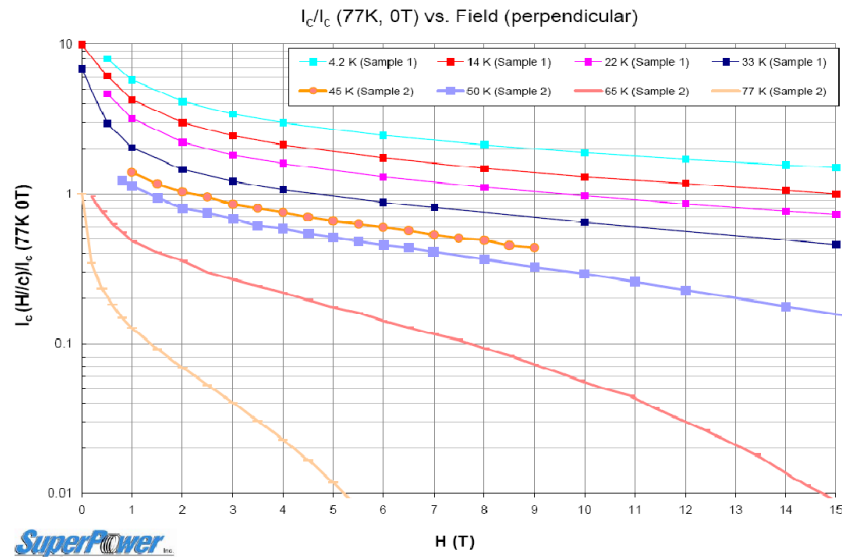
Figure 28. Typical in-field performance for a thin film YBCO tape by SuperPower Inc. Lord (2012). Reproduced with permission from SuperPower Inc.

production-scale equipment would be capable of processing 4–10 cm wide strips in piece lengths up to 1 km.

With a large number of projects to demonstrate the commercialization of YBCO in real-world applications, such as transmission cables, fault current limiters, superconducting motors and generators, so far there has been literally no effort made on its application to MRI. The reason is the above yet-unresolved challenges, including (a) in-field wire performance (needs to be improved at least 3–4-fold at 5 T. It should be pointed, however, that with its high B_{irr} YBCO may find its unique application in helium-cooled high-field MRI with B_{peak} of 10–15 T); (b) variation of parameters along its length (needs to have consistent I_c guaranteed throughout the multi-km pieces); (c) cost (needs to be reduced to at least \$10 kA^{-1} m^{-1} in volume production); (d) persistent operation (joints remain key technology to be yet developed. The resistive lap joint made at SuperPower with a low resistance of 3.5×10^{-8} is still too high compared to a typical requirement of $\sim 10^{-11}$ Ω. A recent new concept of 'wind-and-flip' technique to construct persistent current mode pancake coils (Kim *et al* 2009) could be mentioned, which however does not eliminate the need for low-resistance YBCO joints as the persistent circuit needs to be closed at the switches/leads); (d) quench detection and protection challenges, which were discussed above.

All the above technical and cost issues, together with the rising cost of silver and rare earth metals, make it reasonable to expect that, with the possible exception of YBCO-based coils in a helium-cooled hybrid HTS/LTS ultrahigh-field MR scanner, MgB$_2$ should find use in the mainstream clinical MR before HTS magnets.

With both MgB$_2$ and YBCO, the most realistic introductory path includes specialty MRI magnets, with their smaller dimensions, amount of superconductor and cost threshold for their introduction.
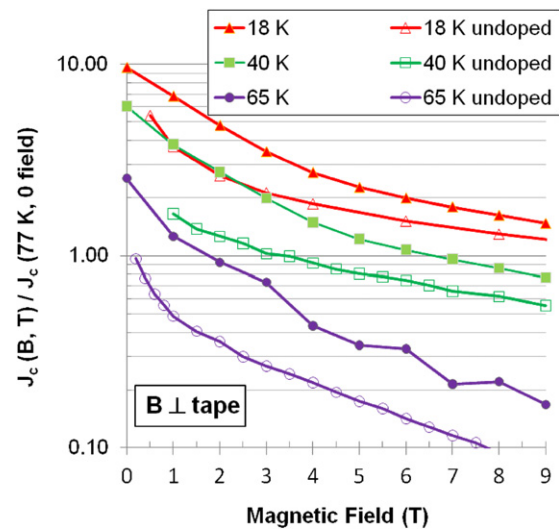

Figure 29. Comparison of Zr-doped and undoped YBCO tape by Superpower (2012). Reproduced with permission from SuperPower Inc.

3.5. Specialty magnets

3.5.1. Specialty opportunities. Whole body scanners presently dominate clinical and research markets due to their universality, which allows them to accommodate a wide range of diagnostic needs and procedures. However, such universality comes with a price tag and with penalties in clinical space, helium usage and performance limitations rooted in the full-size bore and FOV. This makes smaller specialty scanners, dedicated to particular anatomy, an increasingly attractive alternative.

From the clinical perspective, the appeal of a dedicated MR scanner is rooted in its low cost, simpler maintenance and the ability to site it within the limited space of a specialized
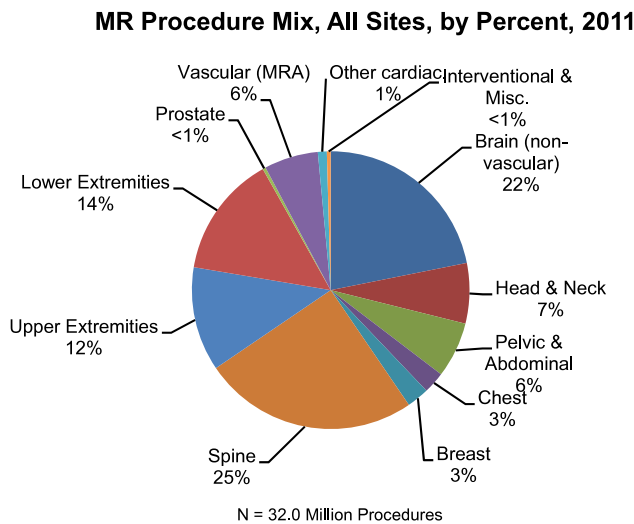
MR Procedure Mix, All Sites, by Percent, 2011

Figure 30. MR imaging procedures in the US based on 2011 data. Reproduced with permission from IMV Medical Information Division.
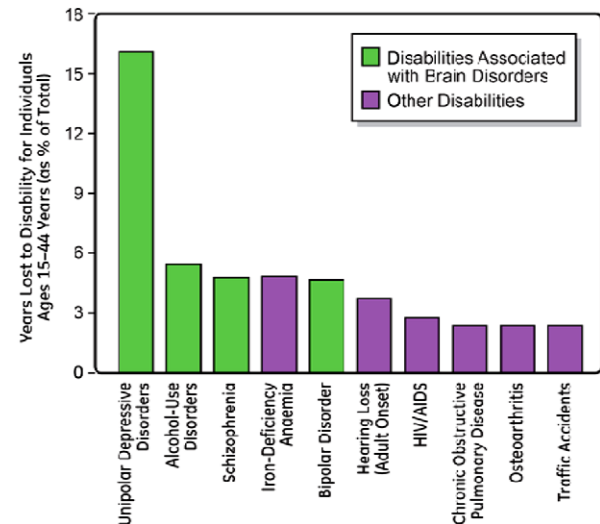

Figure 31. Years-of-life impact of brain disorders (Hyman 2008). Copyright 2008 Nature.

office. From the technical standpoint, specialty scanners have the following key advantages:

- Benefits of a non-traditional scanner geometry envelope, best tailored to the specifics of the imaged anatomy. A spherical (elliptical) FOV that strategically covers the targeted region of interest (ROI), and is also smaller than that of a whole body imager;

- Small size and hence lower coil stresses and reduced E_{stored} enable advanced design options, such as coils with high J_{ave}. The relatively small amount of superconductor and its reduced contribution to the total magnet cost makes the introduction of new superconductors, such as HTS and MgB_2, a more feasible proposition. A lower I_{op} becomes a possible option that allows embedded leads and closed magnet design;

- The small volume of specialty magnets makes them naturally less sensitive to helium availability and cost. Small dimensions are conducive to advanced cryogenic options, such as conduction or convection cooling, which are easier to implement thanks to the short heat removal distances and smaller total thermal budget;

- Significant advantages are also gained by other components of the scanner. The small FOV removes the problem of peripheral nerve stimulation. This, together with the small diameter and stored energy of the gradient coils, allows their design with a much higher strength and slew rate, and also reduces the rating and cost of the electronic power components of the scanner;

- Potential needs in specialized MR imaging are illustrated by the diagram in figure 30 that depicts the distribution of imaging procedures per US data of 2011 (IMV 2012).

The two main candidates that could benefit from dedicated scanners are the head (29%) and extremities (26%), with the spine (25%) being covered by the traditional whole body scanners.

3.5.2. 'The decade of the brain' and head imagers. As a consequence of the growing understanding and better control of the medical, genetic and environmental factors of ageing, the lifespan of humans has increased dramatically in recent decades. Unfortunately, however, this has also led to a great increase in the prevalence of neurodegenerative diseases of the brain, including Alzheimer's disease and other dementias, Parkinson's disease etc. An improved understanding of the brain changes associated with ageing is considered one of the most interesting and challenging topics in MR imaging. The increased importance of such neurodegenerative diseases of ageing along with the increasing incidence of movement disorders, stroke and traumatic brain injuries requires dedicated special neuroimaging tools and techniques.

Of further interest for the researcher in neurological diseases is the growing number of patients with depressive, schizophrenic, bipolar and alcohol-use-based disorders. These disorders as a group significantly increase the number of years-of-life lost to disability (figure 31).

The design of the dedicated head imager can derive certain advantages from the specifics of the imaged anatomy. With the whole body scanner, the bore should allow imaging of any part of the patient's anatomy, and therefore must: (a) provide clearance for the widest point of the body, (b) allow unobstructed axial travel of the patient throughout the full bore length for scanning purposes, and (c) have the full-length gradient and RF body coil incorporated into the scanner bore. Therefore it is the R_{min} of the gradient/RF assembly that defines the clearance for the widest point of the human body in the whole body scanners.

In contrast, for the head imagers the widest parts of the human anatomy, such as shoulders or lower body, lie outside the imaged FOV. They can be accommodated inside the magnet bore, while the gradient/RF insert, with a much smaller inner diameter, would be located at the magnet center and extends only around the head. As a result, magnets with much smaller bores can be employed. The smaller, focused
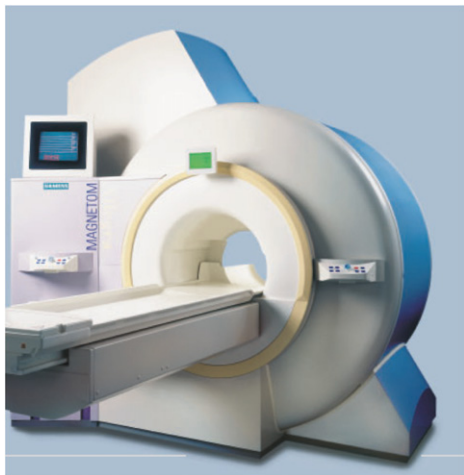
Figure 32. Siemens 3 T head scanner Allegra (Siemens Allegra brochure 2004). Copyright 2004 Siemens.

Table 3.5. Major parameters of the Magnetom Allegra magnet (based on Evaluation Report 2003).

Central field B_0	2.89 T
Patient bore diameter	60 cm
Field-of-view	22 cm @ 0.1 ppm (V_{rms})
Magnet length (with covers)	125 cm
Magnet diameter (with covers)	170 cm
Magnet weight, incl. helium	4500 kg
Shielding	Active
0.5 mT line ($R \times Z$)	2.9 m × 4.4 m
Gradient: strength × slew rate	40 mT m^{-1} × 400 T m^{-1} s^{-1}
Magnet shimming	Passive, 24 trays × 17 pockets
Minimum install area	31 m^2
Superconductor	NbTi
Cooling	Helium bath
Boil-off rate	≤0.12 l h^{-1}

FOV of the dedicated head imagers, as with other specialty scanners, alleviates peripheral nerve stimulation and permits the use of gradients with increased strength and slew rate.

Further advantages can be pursued in the aforementioned asymmetric design. Such one-side accommodation promises the benefits of a shorter geometry as the patient's head is entering from one, shorter side. The length advantages are especially pronounced for the asymmetric gradient design, where the short, next-to-the-shoulders portion of the transverse gradient coils carries field generating conductor arcs, while the return current paths are moved to the remote area above the head. While the short section of the gradients covers the head-to-shoulder distance, it is the accommodation of the shoulders that defines the critical geometric parameters of the magnet, i.e. its length and bore diameter.

One of the first dedicated head scanners introduced in the clinical market was Siemens Magnetom Allegra, (figure 32, parameters see table 3.5). As an essential component for fast-high quality head imaging, in line with the above-mentioned enabling benefit of a specialty scanner, this 3 T system claims to sport the fastest gradient system paired

Figure 33. GE 0.5 T conduction-cooled head imaging system.

with minimum image distortion. On the other hand, the weight of this scanner and the large install area restricted by the magnet fringe field footprint, both exceeding the parameters of a typical 1.5 T whole body machine, are apparent targets for improvement in future pursuits of the siting benefits that are associated with a dedicated scanner.

As a newer development, as a part of the NIH Human Connectome project, Siemens have produced a dedicated brain scanner 'Connectome' using high gradients in conjunction with a commercial whole body magnet.

Innovation-based medical productivity paired with lower costs, the cornerstones of the GE product design philosophy, has been pursued in developments of a dedicated head imaging system at GE Healthcare and GE Global Research. An early 0.5 T developmental prototype was built in 1995. The NbTi magnet was conduction-cooled by one of the first Cryomech 4 K Pulse Tube Coolers (figure 33). The stepped 'top hat' coil envelope took advantage of the head–shoulder anatomy and has been optimized for performance and patient comfort (van Oort *et al* 1998). The unshielded magnet design had $I_{op} = 158$ A, $T_{op} = 6$ K, FOV = 20 cm, weight = 230 kg and 0.5 mT footprint of 2.75 m × 3.75 m (1.3 m × 1.5 m with steel room shielding).

Present market expectations for head scanners, however, are based on advanced standards of neuroimaging and modern clinical practices. Their demand of image quality and throughput is associated with $B_0 = 3$ T and above. Another key requirement for a dedicated brain imager is the high level of portability and autonomy, which should result in advantages in installation and in invisible cryogenic operation.

An advanced dedicated head scanner should feature high performance and imaging speed, small dimensions with improved patient comfort, light weight and autonomous operation for easy siteability and service (figure 34).

A new approach to dedicated head scanners is being investigated at GE Global Research. The concept targets magnet designs with an advanced cryogenic technology,
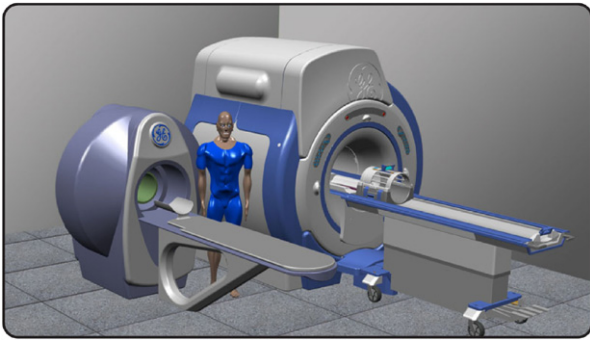
Figure 34. A dedicated head scanner in comparison to a standard 3 T whole body MRI system (artist's rendition).

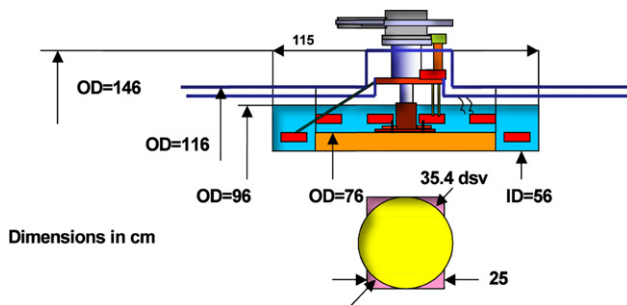**Figure 36.** GE 1.5 T orthopedic MR scanner.

Figure 35. Example of dimensions of a portable neuroscanner.

reductions in size and weight, a large range of imaging capabilities with a high gradient strength and slew rate, and optimized image acquisition protocols and an image analysis technology that permits improved assessment of brain disorders.

In the future, 'portable' scanners may become feasible if it is possible to arrive at a compact magnet design that requires less cryogens. Those portable neuroscanners for head injuries caused by accidents are of considerable interest and find application where the patient cannot be rushed to the hospital and a quick diagnosis is required at the spot, e.g. in the modern battlefield with the rising number of traumatic brain injuries.

However, portable neuroscanners should depend on a miniature cryogenic environment within a mobile ambulance only. 'Portable' could also mean 'cold-dockable', where the unit is temporarily disconnected from the cryogenic umbilical cord within the ambulance vehicle. For the time span that the diagnosis is in progress, the neuroscanner can be moved close to the patient. It has also been shown that cryogenic cooling of the brain can dramatically protect humans suffering from strokes or aneurysms in the battlefield. A mobile ambulance could facilitate both those requirements, slowing down the cellular and biochemical processes, as well as providing the necessary time slot required for imaging (PopSci 2009).

An example of typical parameters for a mobile portable neuroscanner concept is given in figure 35.

The logical expansion of such concepts could point to future hand-held MRI units, possibly based on highly magnetized bulk YBCO, which would presently require a substantial leap in technology.

A different type of specialty scanner targeting multimodal brain imaging is represented by the so-called neuromagnetometers. Neuromagnetometers are based on the design principle of a 'moveable top hat' (Nenonen *et al* 2000).

3.5.3. Extremity imagers. Another area of MRI market growth—orthopedic imaging—gives rise to dedicated extremity scanners. In comparison to head scanners, which are heavily impacted by the need to accommodate patients' shoulders, the extremity magnets have reduced overall dimensions, a smaller bore diameter, a shorter length and a smaller imaging FOV. As a result, the smaller E_{stored} allows additional design freedom, with better portability and cost potential.

Figure 36 shows a commercially available GE product—a 1.5 T orthopedic MR scanner that employs He-bath-cooled NbTi technology.

Like with the head scanners, the natural direction to further improve image quality and throughput of a dedicated extremity scanner is switching to $B_0 = 3$ T while retaining advantages of portability that enables installation in small areas and ease of operation. Such a goal is achievable with common NbTi technology.

With the advancement in high-temperature superconductor technology, in particular BSCCO 2223-type conductors (driven mainly by Sumitomo as the only remaining manufacturer of so-called DI-BSCCO tapes), above liquid helium temperatures there is the possibility of using neon at an operating temperature of 27 K. Since neon is an expensive coolant, thermosiphon technology can be employed. However, the coolant temperature has to be carefully controlled and monitored and should not be fall below 25 K, since neon starts to solidify within the tubes, causing the flow to stop and the magnet to quench (Stautner *et al* 2009a).

The concept of 1.5 T limb scanners based on HTS technology is presently under development at GE Global Research (see figures 37, 38 and table 3.6).

Coil winding using BSCCO tapes is in itself a tedious and costly task, presenting a considerable challenge when compared to a NbTi-based system; more information can be found in Xu *et al* (2010).

Continuing on this path, GE-GRC is currently exploring the design of an affordable MRI system for developing
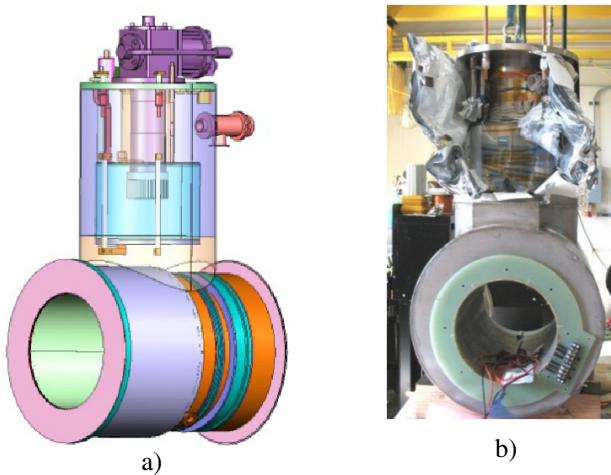
Figure 37. BSCCO-based limb concept scanner, GE Global Research: (a) transparent view; (b) magnet front view prior to closing the vacuum case (Stautner 2012a, 2012b, 2012c).
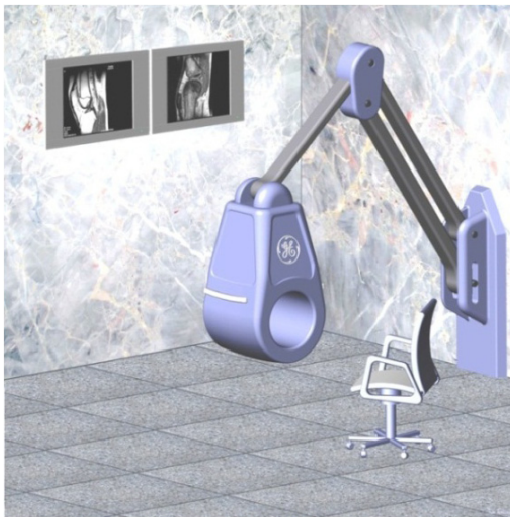

Figure 38. Artist's view of an MgB_2-based limb scanner.

regions, using the potentially low-cost superconductor MgB_2. The nearly cryo-free magnet is thermosiphon cooled. The magnet is unique in its feature that allows the end-user to run the system at dual temperatures, namely at 3 T @ 4 K with liquid helium or at 1.5 T @ 20 K with liquid hydrogen.

Key features here are greatly improved siteability, light weight and reduced cost. Further design details of this NIH sponsored project for 1.5 and 3 T are given in table 3.7 (see also Mine *et al* 2012, 2013).

An example of a 1.5 T HTS magnet for orthopedic application that uses second generation conductor can be found in the development by a New Zealand team (Parkinson *et al* 2013). The design of the passively shielded (iron yoke) magnet with $L_{magnet} = 470$ mm, $D_{bore} = 242$ mm, DSV $= 120$ mm, which has been built and tested, includes 16 double pancake coils wound of 4.8 km of AMSC YBCO conductor. It is another illustration of small specialty magnets being most suitable to pave the introductory way for novel technologies.

Table 3.6. Parameters of BSCCO-based limb scanner.

Parameter	Value
Central field (T)	1.5
Homogeneity (ppm)	6.0
Operating current (A)	120.15
Peak field (T)	2.43
Inductance (H)	8.34
Energy stored (kJ)	60.2
Wire length (m)	7724
Wire resistance (nΩ)	0.43
Fringe field, R_5G (m)	2.5
Fringe field, Z_5G (m)	3.2
Number of coils	6
Conductor	SEI DI-BSCCO
Bare conductor height (mm)	0.22
Bare conductor width (mm)	4.3
Conductor insulation	Kapton, 0.5 mil spiral wrapped
Layer insulation	Pre-preg fiberglass tape
Insulated layer thickness (mm)	0.30
Insulated turn width (mm)	4.4
Operating temperature (K)	27.1
Cryogenic coolant	LNe/closed loop

Table 3.7. Parameters of MgB_2-based limb scanner.

Magnetic field (T)	1.5	3.0
Operating temperature (K)	20	4.2
Operating current (A)	40	80
Peak field (T)	2.25	4.5
Number of coils	6	6
Field stability (ppm h^{-1})	<0.1	<0.1
Image volume		
Diameter (cm)	15	15
Homogeneity (ppm)	10	10
Unshielded gradient		
Strength (mT m^{-1})	50	50
Slew rate (T m^{-1} s^{-1})	200	200
Dimensions (cm)		
Patient bore ID	20	20
Magnet warm bore ID	26	26
Magnet OD	55	55
Magnet length	56	56
Weight (kg)	400	400
5G line from magnet center		
Axial distance (m)	3.2	4
Radial distance (m)	2.5	3.2

3.5.4. Neonatal scanners. Another distinct specialty MR application that could develop clinical potential is for neonatal scanners. An MRI scanner that provides fast, effective and minimally invasive diagnostics of newborn babies would occupy an important role in hospital neonatal intensive care units (NICU).

The specifics of the neonatal application dictate key requirements for such a scanner. Moving a baby from an incubator to a separate imaging room may introduce substantial stress and elevated risk for a frail sick or premature newborn baby. A dedicated scanner design can minimize the impact of re-positioning by accommodating the newborn in

Figure 39. Artist's rendition of a dedicated neonatal scanner.

the bore of a nearby scanner together with its MR-compatible incubator module (figure 39), while preserving the full diagnostics, sensors and tubing connections.

If a whole body MR imager is used for neonatal purposes, it imposes a steep cost penalty of the severely oversized magnet. If positioned in a NICU, the whole body magnet would occupy an expansive footprint with a wide stray field exclusion zone accommodating neighboring field-sensitive equipment and personnel, due to the excessive dipole moment associated with the overly wide bore. Finally, the access limitations of the whole body scanner make it difficult to reach into the bore for interventional procedures or baby handling.

Dedicated neonatal MR imagers should take full advantage of the reduced dimensions, which on a par with extremity scanners represent the smallest scale of MRI imagers. This advantage translates into a shorter magnet, lighter weight and reduced stray field footprint, as well as a small E_{stored} enabling fast ramp up/down. Autonomous design options such as dry conduction-cooled magnets are available for neonatal applications, which would eliminate helium vent connections in the room (as an example, a conduction-cooled design for an actively shielded 1.5 T NbTi neonatal magnet using a pulse tube refrigerator, 830 mm long magnet with 500 mm bore and $E_{stored} = 1.1$ MJ can be found in Wang *et al* (2010); a magnet with a further reduced bore and fewer coils would benefit from an improved footprint, cost and openness).

The combination of the need for openness and the intrinsically small size makes neonatal scanners appropriate candidates for the introduction of the non-traditional non-tubular geometries described in section 3.2. With a smaller unit cost, the tradeoffs in the neonatal design would be predominantly driven by the critical enabling envelope, even if it had to impose some additional cost penalty.

3.5.5. Other specialized configurations. Other non-traditional configurations for potential future MR applications worth mentioning are: animal research MR scanners; MRI pre-polarization systems and MR hybrids, i.e. combination

of an MR scanner with another imaging device (such as MR-PET), or with a treatment device (e.g. MR-Linac combination for radiation therapy).

Scanners used for pharmaceutical and biomedical research on animals can take advantage of a much smaller bore and FOV, which is traded for high B_0 with research benefits. Bruker Biospin and Agilent are leading manufacturers in this area. Some examples of such scanners are shown in figure 40. A vertical BioSpec® system has also been engineered for research investigations of non-human primates. It specifically enables fMRI studies on monkeys, as they are particularly receptive to behavioral conditioning while sitting in an upright position. The vertical systems are offered with two different magnets, operating at 4.7 and 7 T, which both have a high magnetic field stability and excellent homogeneity. The actively shielded gradient coils with integrated shims are especially designed for a vertically oriented magnet.

MRI add-on tools for metabolic imaging. The pre-polarizer is an MRI add-on device that has significant promise in metabolic diagnostics. It uses dynamic nuclear polarization (DNP), in particularly, hyperpolarization of ^{13}C, as a tool for a wide range of applications: study of metabolic processes for disease diagnosis, determination of tissue pathology and organ viability, angiography and perfusion studies, interventional MR, catheter tracking and chemical ablation therapy.

Using ^{13}C hyperpolarization, metabolic processes within the body are made visible by injecting a solution that has been pre-polarized by cooling a vial filled with pyruvate to 1 K and polarizing it at 3.35 T and higher, prior to the imaging process. The injection sample has to satisfy the procedure time window, since its relaxation time exhibits a strong temperature dependence (figure 41(a)). Figure 41(b) shows the high, achievable polarization comparing ^{13}C, normal polarization in protons and electron–nuclear spin coupling, providing a highly sensitive process for prostate cancer detection.

MRI system clinical pre-polarizers are either ^{13}C or ^{128}Xe based. Xenon hyperpolarization would be mainly applicable for low proton density organs, such as lungs, to provide good signal enhancement. Figures 42(a) and (b) show the cryogenic part of the now fully automated ^{13}C SPINLab™ Polarizer built by General Electric. Recently, pre-polarization results were published at ISMRM 2010, showing the feasibility of the concept. In November 2010, UCSF researchers for the first time successfully used this technology to conduct real-time metabolic imaging in a human patient, after prior tests on animals. This new approach improves the assessment of the precise outlines of a tumor, its response to treatment and how fast it is growing (UCSF Website 2010). For further details on the multi-sample component closed-cycle hyperpolarizer and its fluid path, see Leach *et al* (2010). For cryogenics see Urbahn *et al* (2009), Stautner (2009) and Stautner *et al* (2009b).

Multimodality combinations. Combining an MR scanner with another imaging or treatment device in the clinical environment can be done in two ways. One obvious way is two separate devices positioned in the vicinity of each

Figure 40. Scanners for research (courtesy Bruker); (a) earlier PharmaScan® 7 T, bore diameter = 16 cm, with LN_2 thermal shield; (b) BioSpec® 70/20, B_0 = 7 T, bore diameter = 20 cm, single thermal shield; (c) BioSpec® 170/25, B_0 = 17 T, bore diameter = 25 cm, subcooled helium; (d) ClinScan®, B_0 = 7 T, bore diameter = 30 cm, bore diameter = 25 cm, pulse tube cryocooler, used in animal MRI/MRS metabolism studies. All magnets except (c) feature active shielding (Westphal 2012).
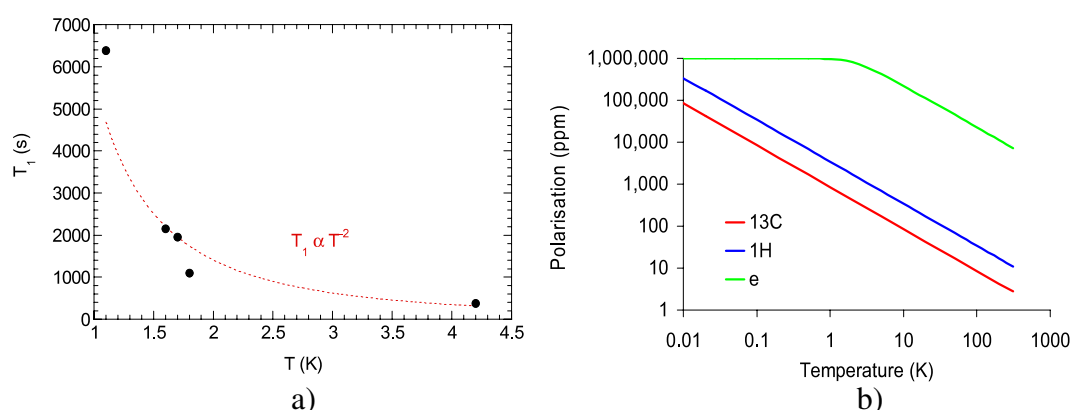

Figure 41. (a) Relaxation time T_1 (s) of polarized ^{13}C pyruvate versus temperature (K), (b) achievable polarization (ppm) versus temperature (K).

other, with the patient table shuttled between the two. Such an option, however, suffers from spatial and temporal separation between the two procedures, which limits the accuracy of mutual dynamic registration of organs in the region that is targeted for superposition. The other arrangement—an integrated device—represents the most efficient, albeit technically challenging option.

Integration of MR scanners with other imaging devices, such as CT or PET, typically takes place inside or near the bore, and thus has more interference with the gradient
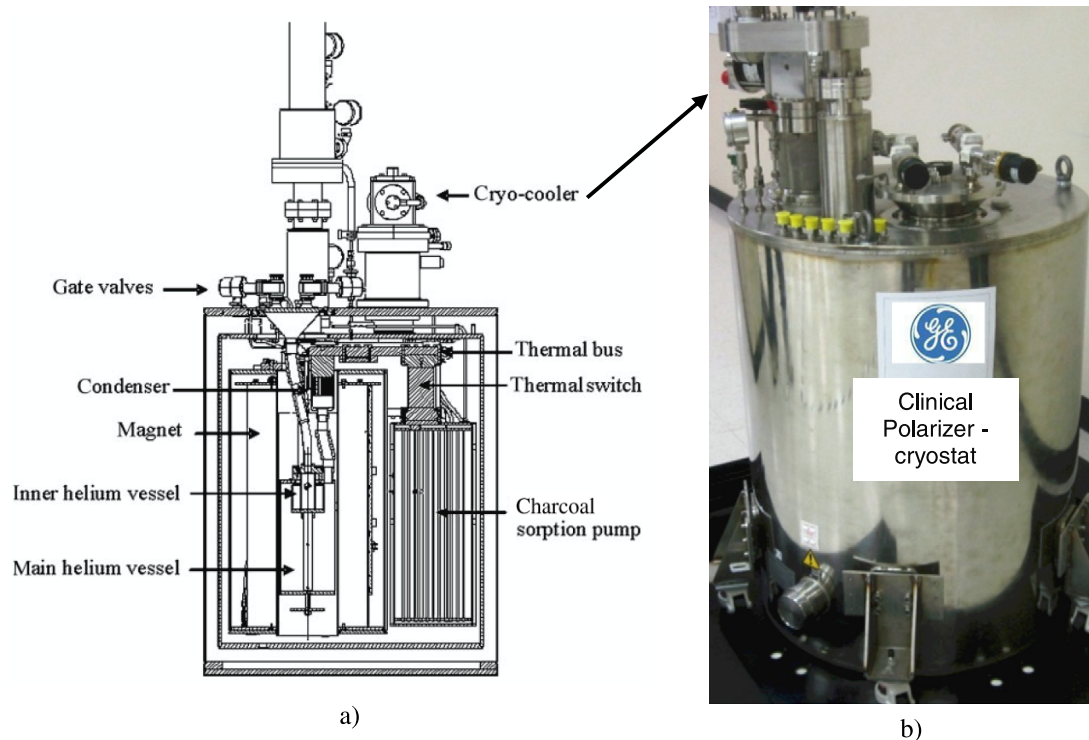
Figure 42. (a) 3.35 T magnet and cryostat design (sub-atmospheric operation) (Ardenkjaer-Larsen *et al* 2011). (b) Polarizer cryostat built with a cryocooler on top.

and RF components than with the magnet. This is not the case with MRI-guided radiation therapy (RT) for oncological applications. The effectiveness of radiation treatment depends on the accuracy of delivering the intended dose to the targeted tissues within defined margins, which is complicated by tissue movements during the procedure. MRI images are used to guide the beam delivery to the tissue. A combined system would include an accelerator incorporated around the centerline of the magnet, with the beam aimed at the FOV region.

To avoid attenuation or distortion of the beam, the magnet design in MR-RT combinations should provide sufficient central passage for the beam, and enable rotation of the beam position with respect to the patient. Different topologies can be employed for this purpose. A bipolar design with a full split between the halves provides the most unobstructed beam access, and can use either a permanent magnet (PM) MR scanner (figure 43(a)) or a split-open superconducting magnet (figure 43(b)). As was pointed out earlier, due to the design penalties of this topology, it is intrinsically limited to low fields (typically <0.5 T). Better image quality is pursued by Philips with a 1.5 T MR scanner (albeit with additional challenges from the high magnetic field, such as the electron return effect (Raaijmakers *et al* 2008)). The approach is currently actively pursued by Philips in its Linac MR Ranger Systems. In such a configuration, the magnet incorporates a sufficient central gap (split) cleared of coils, while the cryostat components do not provide a full magnet split (figures 43(c) and (d)). A considerable challenge also exists in creating a split gap in the gradient coil (Shvartsman *et al* 2011), which affects its maximum performance.

Last but not least, the MR-PET combination should be mentioned as a developing multimodality. This application has an option where a PET insert is used inside the standard magnet bore, without modifying the superconducting magnet configuration.

4. High-field LTS magnets

4.1. High-field NbTi and Nb₃Sn magnets for MR research

With 3 T now recognized as the high standard for field strength in clinical practice, pursuit of yet higher B_0 continues in research scanners, arming them with further improvements in resolution, image quality and speed.

In the earlier stages, several 4 T research scanners were produced outside of the 'standard' clinical 3 T denomination, but it is $B_0 = 7$ T that is increasingly considered in medical research practice as a new standard for research imaging (Wada *et al* 2010). Scanners for human research above 7 T are now a reality, with the first 9.4 T scanner installed by GE at UIC in 2003 (figure 44). While the number of 9.4 T imagers continues to grow, the first 11.7 T scanners are arriving on the scene (Hurst 2010). To date, over 50 ultrahigh-field (UHF) MRI scanners for human research with $B_0 = 7$ T or higher have either been installed or are scheduled for installation by different manufacturers in research centers and 'luminary sites' worldwide.

Based on their bore size, UHF MRI magnets fall into three distinct application-driven categories.

(I) *Whole body* scanners. This category initially included magnets with bore diameters around 900 mm. However,
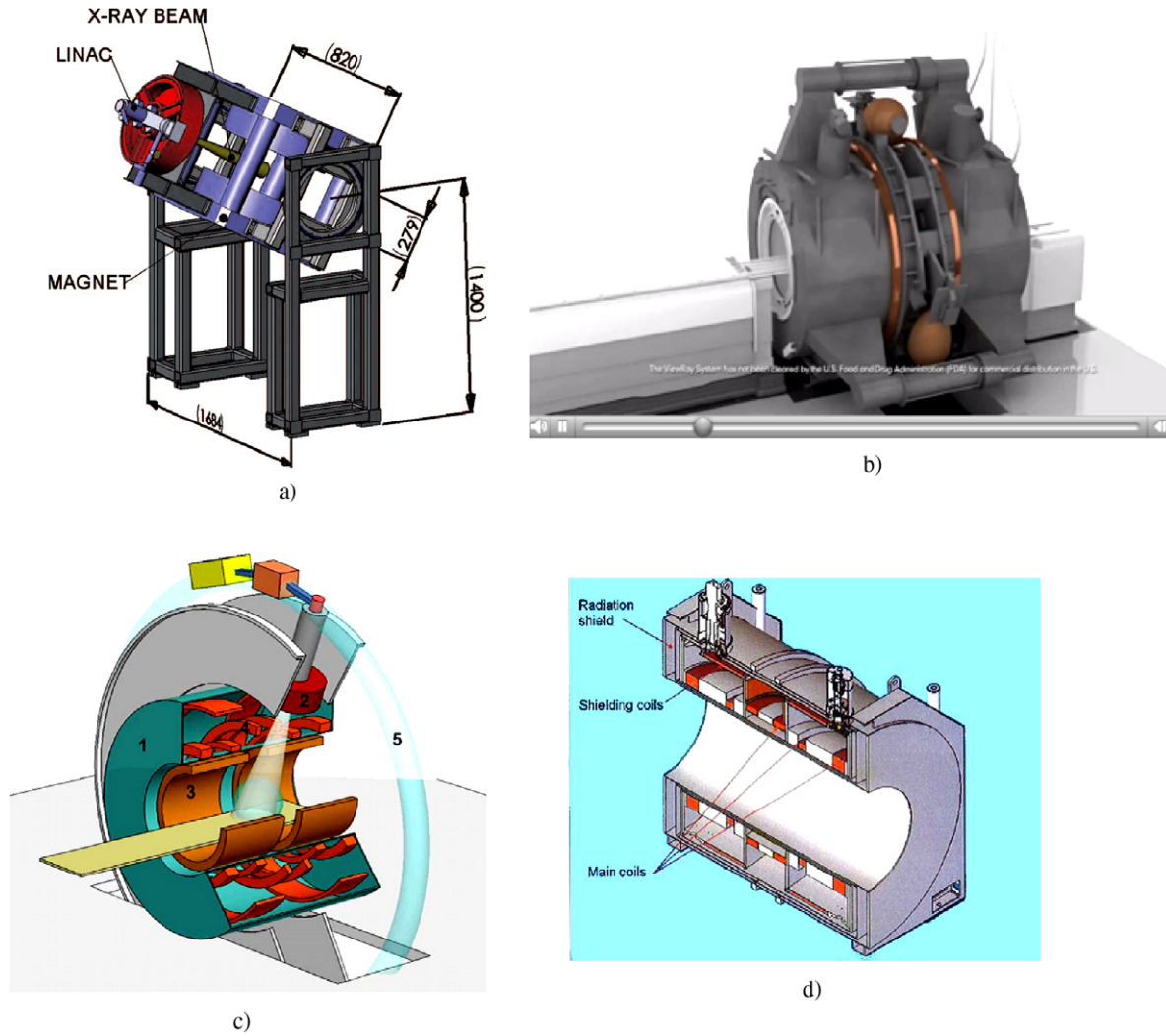
Figure 43. Possible MRI-RT combinations: (a) 0.2 T PM-Linac combination, University of Alberta, Canada; magnet and Linac rotate together around the patient (Fallone *et al* (2009), copyright 2009 American Association of Physicists in Medicine); (b) split superconducting magnet–accelerator combination by ViewRay (image courtesy ViewRay); (c) and (d) integrated MR-RT concept by Philips using a Magnex 1.5 T magnet with the 15 cm split in the central coil (Raaymakers *et al* 2009).

Figure 44. First 9.4 T MRI magnets for human imaging. Reproduced with permission from Lvovsky and Jarvis (2005). Copyright 2005 IEEE.

recent advances in gradient technology have brought a smaller, more efficiently utilized annular gradient space, which made possible accommodating the complete human anatomy with the smaller magnets. UHF magnets with bore diameters down to ~800 mm can now be designated for whole body imaging (Liebel 2011, Warner 2008, Dai *et al* 2012, Wang *et al* 2012).

Differences in the bore size have a strong impact on the magnet length (via the homogeneity, which depends on the coil envelope angle $\alpha = \tan^{-1}[R_{\min}/Z_{\max}]$), on the fringe field footprint and use of active shielding (via the dipole moment $M_{\mathrm{d}} \propto I_{\mathrm{op}}N_{\mathrm{turns}}D_{\mathrm{coil}}^2$); and on the overall weight and dimensions of the magnet (via conductor and structural components), which provides a significant resulting cumulative effect on the cost and risk of the design. Following a simple scaling with conductor cost $\sim D_{\mathrm{bore}}^3$, according to (Warner 2008), a 7 T whole body magnet with a 830 mm bore provides over 20% savings in conductor compared to a 900 mm magnet.

(II) *Head-only* scanners. Cost and risk are further reduced in this category, which has a magnet bore in the
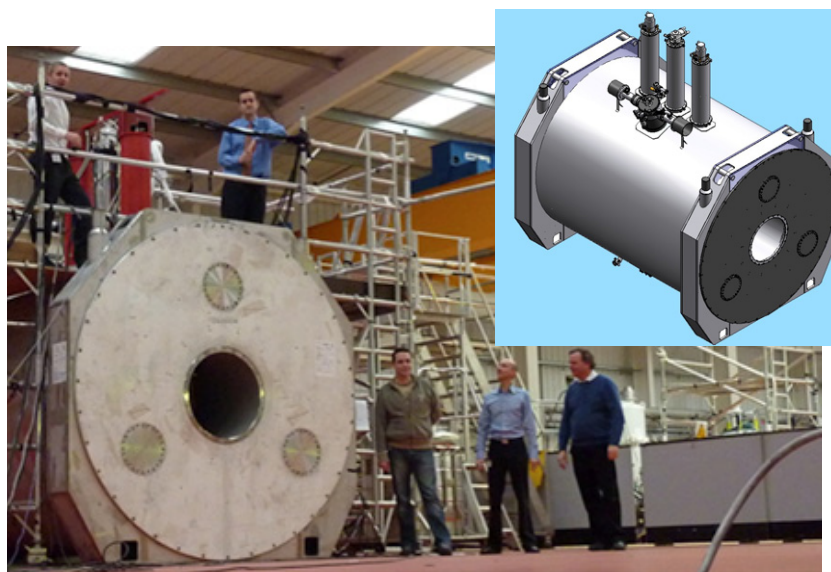
Figure 45. 11.7 T, 680 mm bore magnet for human imaging (photo at www.spinsights.net, posted on 20 Dec. 2010, inset magnet from Warner (2010), reproduced with permission).

650–700 mm range. Taking advantage of the imaged geometry, which does not require imaging of the rest of the body, this configuration has gradient and RF coils located only around the head, while the magnet bore is sized to accommodate the wider shoulders.

(III) *Animal* scanners for research represent a category that uses yet smaller magnets, with D_{bore} that can reach below 200 mm, depending on the intended research purpose. Magnets from this category may introduce advanced technical solutions that are enabled by their particularly small dimensions. In recent years, some technologies introduced in animal scanners have been migrating into UHF magnets for human research with increasingly larger bore sizes.

It is the traditional technology, based on traditional NbTi superconductors and a pool-boiling helium bath at nearly atmospheric pressure, that limits the available field strength for research MR magnets to $B_0 = 9.4$ T (400 MHz proton frequency). 7 and 9.4 T whole body magnets use a compensated solenoid design that minimizes the B_{peak}/B_0 ratio and coil stresses while operating at the limits of NbTi at 4.2 K. Compared with discrete coils, such a design inevitably pays a penalty in an increased amount of superconductor, magnet weight, length and cost. To create a homogeneous field, smaller coils are added on top of the main solenoid (example in figure 5), sometimes of negative polarity (Lvovsky and Jarvis 2005). In such an arrangement, unlike in a discrete multi-coil magnet, a large portion of the inter-coil forces is accommodated by a self-reacting solenoid, which eliminates the need of a portion of the inter-coil structure. (We should mention here the later described different approach that was chosen for the largest 11.75 T ISEULT MR magnet, under development in France, where the high-current pancake-wound coils are separated by field-shaping inter-coil distances somewhat similar to the discrete coil configuration.)

Advances beyond 9.4 T are achieved either by a reduced operating temperature of NbTi, or by introducing Nb_3Sn in the magnet design. Both directions have been pursued in UHF magnets for human MR research by Bruker and Agilent (former Magnex group), where their experience with NMR magnets and animal scanners helped pave the road for UHF human scanners.

While active shielding is the natural standard choice for smaller animal scanners, earlier 7 and 9.4 T scanners were passively shielded, which required several hundred tons of steel in the walls of the imaging room. Actively shielded designs for whole body UHF scanners are now being implemented. It represents the tradeoff where total siting (the total room weight and dimensions) is substantially improved at the expense of the weight and cost of the magnet. Active shielding is implemented in Bruker's Ultra-Shield Refrigerated (USR^{TM}) technology, and in Agilent ASR magnets. For example, use of active shielding in Agilent's 7 T, 830 mm bore magnet allows one to reduce the 5 G line to 3.8 m $\times$ 6.0 m (Warner 2008). A comparison of the parameters of different UHF MRI magnets and their shielding options can be found in Liebel (2011).

Magnets with $B_0 = 11.7$ T use NbTi coils in a sub-atmospheric He bath, allowing operation in the region around 2 K. The 11.74 T magnet by Agilent, shown in figure 45 ($L = 3.66$ m, weight $\sim$60 tons) uses 572 km of NbTi wire-in-channel operating below 2.5 K (the passively shielded, magnet fringe field extends 21 m $\times$ 27 m in the absence of room steel) (Warner 2010).

Above 11.7 T, Nb_3Sn has to be employed. Among the key challenges are: a demanding wind and react (W&R) process; a dedicated low-field area for joints that extends the space occupied by the already long coil former; single layer Nb_3Sn pieces of substantial length (Warner 2010). Using sub-atmospheric helium at about 2 K allows the amount of Nb_3Sn to be minimized by employing a hybrid design that

uses both NbTi and Nb_3Sn coils, but retains the challenge of the hybrid $NbTi/Nb_3Sn$ persistent joints.

Some advanced technologies that are finding their way into UHF research scanners may not yet be fully ready for the commercial level of cost and reliability demanded by clinical applications. Here UHF research scanners may help to introduce them in the MR field. One example is the Cryomech pulse tube coolers used by Bruker to reduce vibrations and improve image quality.

Among the key challenges of UHF magnet design are:

- high stored energy, exceeding that of a 3 T MRI magnet by an order of magnitude, has to be accommodated by the quench protection system. Use of commercial NbTi wires in a high-B_{peak} environment limits I_{op} typically to a ~300 A range, which results in a large inductance and a complex winding process, with demanding requirements on individual piece lengths and a large total amount of conductor;

- magnet weight and dimensions. The length of the magnet is critical in the compensated solenoid design. A large magnet diameter, increased due to shielding coils in the active shielding option, has challenges in ceiling height for magnet transportation, installation and maintenance;

- with high B_0, fully passive shimming is not an option. The magnet has to be equipped with superconducting shims, even though the solenoid has better potential for consistency than the multi-coil design. The shim assembly consumes important space in the cryostat and further increases the magnet cost;

- stability requires an extra margin in comparison with 1.5 and 3 T magnets, as the time and cost associated with excessive training of a magnet with >100 MJ stored energy is not an option. A graded conductor with an optimized stability and stress distribution helps to manage the cost of the magnet;

- limited options for low-field areas to accommodate field-sensitive components such as cryocoolers, switches and persistent joints. Their accommodation may require an increase in the length or ceiling height of the scanner (higher location for cryocooler). As a possible option for persistent joints in UHF magnets, local shielding with small dedicated coils can be employed, as attempted in some NMR magnets (Dixon *et al* 2005);

- strong magnet–gradient interactions. A high magnet B_0 exerts strong Lorenz forces on the conductors of the pulsed gradient coils, causing substantial vibrations and acoustic noise. Additionally, the UHF magnets exhibit elevated magneto-mechanical effects from the eddy currents induced by gradient coils in the conducting magnet components, e.g. thermal shield cylinders. Forces on such eddy currents in the magnet structure grow with the higher B_0 and with the stray field of high strength gradients, which can result in a noticeable gradient-induced helium boil-off with a resonant behavior (Dietz *et al* 2011).

A specific additional challenge may arise for UHF scanners that do not employ active shielding. It is related to

Table 4.1. Basic parameters of ISEULT magnet (Vedrine *et al* 2010).

Parameter		
Central field	T	11.75
Warm bore diameter	mm	900
Vacuum vessel length	m	5.0
Vacuum vessel OD	m	4.8
Magnet weight	ton	132
Homogeneity at 22 cm DSV	ppm	<0.5
Field stability	ppm h^{-1}	<0.05
Shielding (5 G line, axial × radial)	Active	13.5 m × 10.5 m
Stored energy	MJ	338
Operating current	A	1483
Cooling	—	Pressurized He-II
Operating temperature	K	1.8
Operating pressure	MPa	0.125

degaussing of the MRI suite with large embedded iron walls after a ramp (Sammet *et al* 2010).

All the above challenges impact the cost of high-field scanners, which is currently the main obstacle on their route to commercialization. The successful design, manufacture and operation of research scanners installed worldwide have demonstrated their technical viability and diagnostic benefits; it is the commercial equation that will define the pace of their transition to clinical volumes.

An area where a high B_0 can make the greatest diagnostic impact is in brain imaging. A dedicated head scanner with B_0 beyond 3 T has reduced challenges, due to a smaller bore size and E_{stored}, and thus may ease the clinical introductory threshold for high-field MR.

4.2. ISEULT, the largest 11.75 T MRI magnet

4.2.1. ISEULT–INUMAC project. As the world's largest-to-date whole body MR magnet under development, ISEULT is a notable example of a radical departure from the conventional solutions in several design areas. It illustrates the level of qualitative changes and increase in complexity and cost involved when a scale-up beyond the limits of the established MR technology is attempted.

The 500 MHz magnet with a warm bore of 900 mm is intended for the NeuroSpin Research Centre at CEA Life Science Division in Saclay, as part of the French–German INUMAC project, dedicated to advancing neurological research and molecular imaging in ultrahigh fields (Vedrine *et al* 2010, 2012). Among its goals are the investigation of advanced techniques at 11.7 T; exploration of novel concepts in gradient design and parallel imaging; and pre-clinical brain contrast development for patients with Alzheimer's, strokes and tumors. The project, which started in 2006 with a €200 M budget, involves a consortium of academic and industrial partners. The general parameters of the magnet are summarized in table 4.1.

The high B_0, large 900 mm warm bore and stringent 5 G line are key specifications that drove the departure from the traditional MRI technology, and resulted in adopting a coherent set of interdependent design solutions.
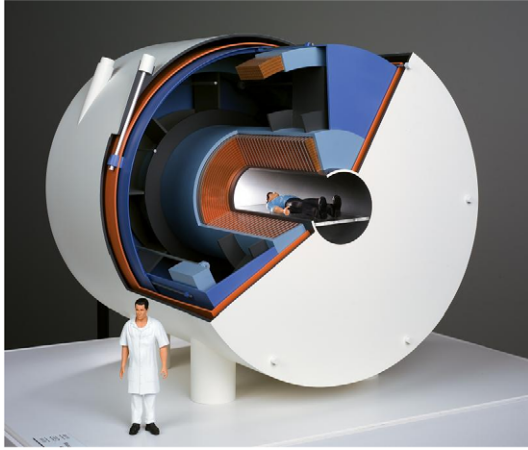
Figure 46. ISEULT 11.75T 900 mm warm bore magnet (artist's rendition).

- The high central field together with the large bore diameter dictated a large E_{stored}. In order to limit the quench voltage, as well as the number of individual conductor lengths and joints, the design resorted to high-current conductors, well beyond the traditional MR range of I_{op}.

- The non-traditional large conductor impacted the main coil design and winding approach, as well as the choice of non-persistent joints and embedded current leads, that implemented the B_0 stabilization scheme by power supply.

- To constrain the 5 G line within the experimental room, active shielding has been selected. Tradeoff analysis showed that passive shielding would require 800 tons of steel, while the active shielding results in a 15% conductor cost increase (Schild *et al* 2008).

- Shielding coils with smaller B_{peak}, controlled stresses and optimized, more traditional conductor dictated a large OD, which impacted the cryostat design, cryogenics and quench protection approach.

4.2.2. Magnet concept, coils and conductors. The principal concepts of the ISEULT magnet (figure 46), their drivers and a comparison against conventional MR design approaches are summarized in table 4.2.

The magnet design uses NbTi coils cooled by superfluid He-II at 1.8 K. A possible alternative approach would be a hybrid design that employs both Nb_3Sn and NbTi coils in a traditional helium bath at 4.2 K (Wada *et al* 2010); however this creates a substantial challenge with stress-sensitive Nb_3Sn coils during manufacture (W&R versus R&W). In the tradeoff between Nb_3Sn risks and NbTi He-II cryogenics, the choice was made in favor of the latter.

The ISEULT main coil (MC) consists of 170 double pancakes (DPs) with 88 turns in a single pancake. Control of the theoretical homogeneity with the DP design is done (a) by selecting an axial distribution of DPs (adjusted with inter-DP spacers); and (b) by controlling individual conductor positions in the DPs (special half-spiral winding with center offset to minimize transverse harmonics (Aubert 2011)). Modular

DP design allows redundancy in DP manufacture and testing to cover contingencies in magnet assembly; it also places inter-DP resistive joints in the low-field region over the OD and accommodates a larger conductor bending radius.

Active shimming coils, with passive shim backup, are planned to control the actual 'as-built' FOV. The main coil employs a 10-strand Rutherford cable soldered into copper channel stabilizer (RIC). Conductor parameters for main and shield coils are given in table 4.3.

The RIC conductor configuration, selected among three options (Berriaud *et al* 2010), has never been used previously in MR applications. It enables a large total NbTi cross-section for $I_{op} = 1.5$ kA at 12 T, while accommodating acceptable filament twist, structural integrity and dimensional stability of composite conductor at optimal cost. The large copper stabilizer area ($J_{op} = 33$ A mm^{-2}) with RRR >100 is primarily driven by the mechanical strength $\sigma_{0.2\%} > 250$ MPa required for coil hoop stresses; it also helps to achieve high conductor stability. The He-II channel-cooled RIC is characterized as cryostable; at this low T_c (12 T), the stability limit is dominated by Kapitza resistance (Berriaud *et al* 2010).

The shield coils employ a traditional vacuum impregnated solenoidal design thanks to the relatively low $B_{peak} = 3.88$ T. The 36 layers $\times$ 53 turns coils are wound in individual pockets in an aluminum former. The wire-in-channel (WIC) conductor, albeit of non-traditionally large dimensions (table 4.3), provides the required current carrying capacity; the copper cross-section ($J_{op} = 39$ A mm^{-2}) is driven by the hoop support requirement. Both RIC and WIC conductors are manufactured by Luvata.

The large shield coil diameter ($OD \approx 4.3$ m), their axial positions and the 5 G footprint have been carefully selected. These design tradeoffs allowed adjustment of the axial force so that it is minimal and directed inward. It mitigates potential frictional stick–slip quenches at the coil interface at the loaded inner flange; it also simplifies the task of structural support. The main challenges to the shield coil design are hoop stress and stability control.

In quench reduction efforts, coil mechanical support minimizes mechanical interactions between the coils, formers and helium vessel (Nunio *et al* 2010). The stack of DPs that constitute the MC solenoid has no contact with the helium vessel inner cylinder, allowing no-friction contraction of the main coil and helium access at the ID. The MC is held from its sides between two plates which provide a 360 ton preload with a stack of Belleville washers; the outer and inner cylinders act as tie-rods. The internal Lorenz force of 8000 ton in the MC solenoid is transferred/reacted through the inter-DP insulation plates.

The shield coils are supported in aluminum former pockets; they are preloaded to ensure stable contact with the loaded surface of the frame under a 91 ton inward force. The mechanical design also accommodates a 334 ton unbalanced force during abnormal fault conditions (Nunio *et al* 2010). Eight titanium alloy rods are used as the cold mass radial suspension elements.

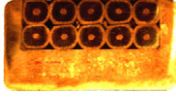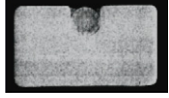**Table 4.2.** Key technical solutions and drivers in ISEULT magnet design.

Area of design	Present MR technology	ISEULT solution	Solution drivers	Impact
Coils topology and winding	Discrete multi-coil <4 T; compensated solenoid >4 T; layer-wound	Main: stacked double pancakes (DP); axial location control by spacers; shields: traditional layer coils	$B_{peak} \approx 12$ T; $E_{stored} = 338$ MJ; large 1.5 kA conductor; DP modularity and redundancy	Tight dimensional accuracy for DP and conductor positioning >170 inter-DP joints
Homogeneity control	Coil position and build dimensional control SC and/or passive shims	Inter-DP spacers; offset half-circles in DPs; shimming: SC + passive	0.5 ppm @ 20 cm DSV; large size conductor	Radial build variations control; limited shim capacity at 12 T
B_0 temporal stability	Persistent operation, $I/I_{op} < 0.75$; n-value 30+ supercon joints < 10^{-10} Ω, moving metal comp circuit	$I/I_{op} = 0.32$; resistive joints $\sim 10^{-9}$ Ω; PS with driven-mode stabilization	Number of joints between DP; large number of filaments; no SC joints @ 1.5 kA	Added complexity/cost of PS; permanent leads; non-zero boil-off cryogenics
Conductors	WIC and monolith NbTi wire; I_{op} below 1 kA	$I_{op} = 1.48$ kA; main: Rutherford cable-in-channel; shields: large WIC	$E_{stored} = 338$ MJ → high I_{op}, large conductor size	Conductor cost; individual turn placement accuracy
Conductor stability	Epoxied coil < cracks limit; optimized former interfaces	Pressurized 1.8 K He-II wetted DP cryostable conductor; DP friction-free at OD and ID	Large single conductor; high stress; quench avoidance (large E_{stored})	Low $J_{ave} = 2.6$ kA cm^{-2}; conductor weight 65 ton (main)
Quench protection	Passive detection, active protection (heaters); E_{stored} dumped into all coils; dump resistor internal	Active detection, active protection; E_{stored} dumped in shields only; dump resistor external; quench expands into satellite vessel	Unknown dynamics in He-II DP; quench pressure control	Expansion satellite vessel; 1.5 kA breakers; cost of QP system
Cryogenics and Helium vessel	He-I at ~ 4.2 K; single vessel with cryocooler; zero boil-off recondenser	3 separate, connected He-II vessels; stand-alone cryoplant; satellite buffer vessel; cryotube with electrical connections	NbTi at 12 T requires subcooled; 1.8 K He-II; He volume reduction; heat load from permanent leads	Cost of stand-alone cryoplant with satellite equipment; operational complexity/cost
Current leads	Retractable or embedded	1.5 kA leads embedded in outside vessel; connection via 1.8 K cryotube	Driven-mode → embedded leads; high I_{op} → extra heat load	Increased thermal budget; extra cryo capacity and lines
Main coils axial support	Force from coil interfaces transferred via former	DP stack-up between two plates; preloaded against HeV cylinders	Main compressive force of 8000 ton; friction avoidance at interfaces	Inter-DP spacer design; preload sensitivity
Shield coils axial support	Force from coil interfaces reacted via former structure	Aluminum former with pockets; in-pocket wound/VPI'ed; inward force of 91 ton	Conventional approach, modified former/HeV accommodation	Loaded flange interface (friction)
Coil hoop support	Cu in conductor; overwrap (or former) @ coil OD	Self-supported DP and shield coils	Quench avoidance at interfaces	Increased amount of Cu; coil size and weight.

4.2.3. B_0 stability and quench protection. With the absence of reliable superconducting joints in the 1.5 kA range, the design adopted resistive inter-DP joints with a resistance of 10^{-9} Ω, which results in a total magnet resistance ~ 200 nΩ during operation. The required B_0 stability <0.05 ppm h^{-1} is achieved via a filtering stabilization technique, using an external power supply unit (PSU) (Sinanna *et al* 2010). An

external PSU implies embedded leads. This approach also enables the use of an external dump resistor, $R_D = 2.7$ Ω for quench protection, permanently connected in parallel with the magnet. The quench terminal voltage can reach 4 kV.

The filtering resistor $R_F = 0.1$ mΩ is connected in parallel to the magnet and dump resistor. It provides a shorting path for small ripples in the high-frequency range where

**Table 4.3.** Conductor parameters in ISEULT main and shield coils.

		Main coil	Shield coil
Conductor type	—	RIC	WIC
Conductor dimensions	mm × mm	9.2 × 4.9	9.1 × 4.2
Core strand dia/number of wires	mm/—	1.49/10	1.57/1
B_{peak}	T	12	3.88
I_c	A	$\leq$1500@12 T, 4.2 K	$\leq$2100@5 T, 4.2 K
I_{op}/I_c@T_{op}, B_{peak}	%	32	27
Overall Cu/NbTi ratio	—	5.03:1	44:1
Temperature margin	K	1.0	4
Conductor length	km	139	60
Conductor weight	ton	65	19
Inter-turn insulation	—	A-stage pre-preg	VPI glass-epoxy

the magnet coil impedance is high enough, so that only the constant 1.5 kA PSU component goes to the magnet. This approach allows effective filtering of ripples of frequencies ω that satisfy the relation $R_F \ll \omega L_{mag} \ll R_D$, while reducing the stability requirements for the high-current PSU and hence its cost. During quench with $V_q = 4$ kV, the filtering resistor is protected against the overcurrent by the superconducting fault current limiter (FCL) connected in series, which is located in a separate satellite helium vessel (figure 47).

Magnet quench protection is based on active detection of differential voltages in coils (detection threshold 100 mV; duration 100 ms) (Vedrine *et al* 2012). Circuit breakers disconnect the PSU, and the magnet energy is discharged into the magnet coils and into R_D. A deliberate design decision was made not to rely on spreading the secondary normal zones in the main coil, due to the uncertain accuracy of the complex quench dynamic modeling in the He-II cooled DP geometry (Juster *et al* 2010). The two shield coils are equipped only with quench heaters, six in each, that are initiated by the quench protection system. Detailed quench modeling confirmed the feasibility of the approach, indicating a time delay of 5.8 s, and $T_{hot\ spot}$ below 150 K for the shield and under 120 K for the main coils (Juster *et al* 2010).

4.2.4. Cryogenics. The need to provide He-II bath cooling of the 105 ton cold mass with large diameter coils demanded non-traditional cryogenic solutions. To minimize the He-II volume, the main coil and each of the shield coils are placed in separate helium tanks, all three vessels are connected by tubes. Even with the optimized topology, it requires a total of 4500 l of He-II, two-to-three times the He-I volume of a 1.5 T/3 T whole body MR magnet.

The large cold mass surface area, permanent heat loads from the embedded 1.5 kA leads and FCL cooling contribute to an increased thermal budget. A dedicated cryoplant covers cryogenic loads at the three levels: 590 W at the 55 K thermal shields; 23 W at the 4.5 K vessels/components and 20 W at the 1.8 K volumes. The cryoplant includes the dewar, cold box, satellite vessel and cryopipe (figure 48). A separate satellite vessel accommodates the leads and the FCL, and is connected to the magnet with a 1.8 K cryopipe
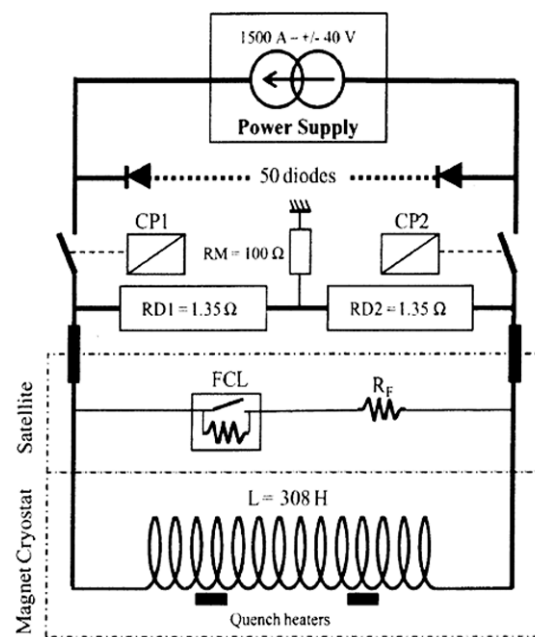
Figure 47. ISEULT filtering field stabilization and quench protection scheme (Schild *et al* 2010). Copyright 2010 IEEE.

with cryogenic and electrical connections. The satellite vessel implements a double-bath solution, having a saturated bath with a 4.2 K/1.8 K heat exchanger and a pressurized He-II bath that is separated from He-I by a lambda plate. The cryopipe volume also helps control the helium expansion pressure in case of quench. With tubing welded on the coldmass, the cooldown from 300 K should take about four weeks.

4.2.5. Technology applicability for clinical and research magnets. Several reduced-scale prototypes, each addressing a specific set of design and manufacturing risks, have been tested. Full-scale serial production of double pancakes has started at Alstom. The project plan included finishing DP and shielding coil manufacture in mid-2012, followed by coldmass and cryostat assembly. Partial tests at room temperature will be performed at Alstom upon completion
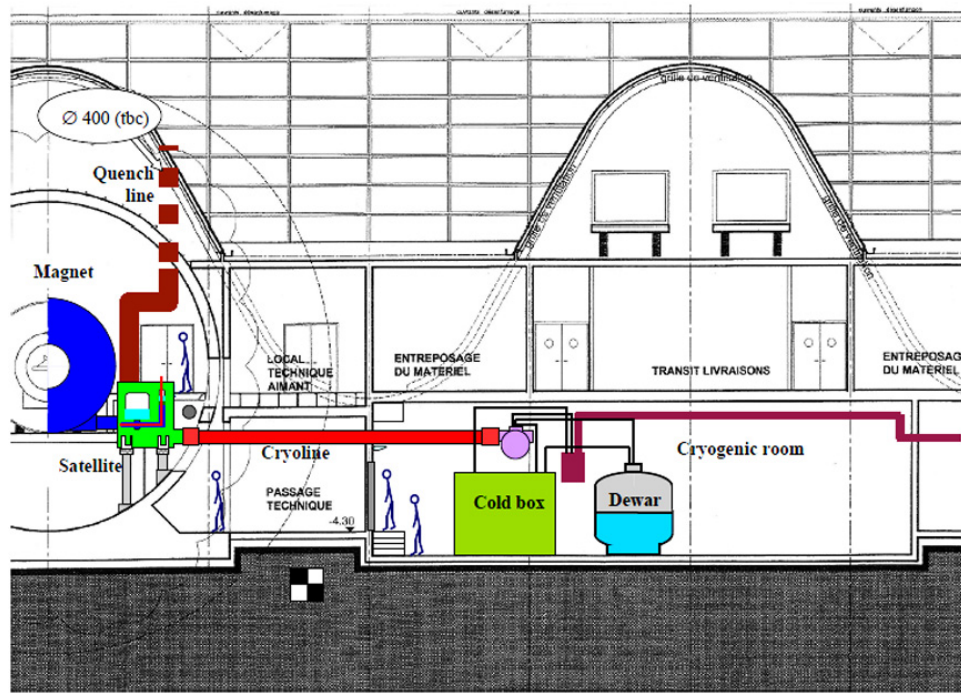
Figure 48. Cryogenic arrangements of ISEULT magnet. Reproduced with permission from Schild *et al* (2008). Copyright 2008 IEEE.

of the assembly. The magnet is planned to be delivered to Saclay, where the final tests will be conducted at 1.8 K at the Neurospin Centre.

ISEULT's unprecedented mission and size yielded advanced developments in several technical areas, using an approach tailored for such a unique one-of-a-kind magnet. Even if other UHF MRI may not follow such an approach directly and choose a smaller bore compatible with less complex traditional solutions and lower cost, one can see how some components of the ISEULT-developed technology may, in some incarnation, find their way into various segments of future MR (Schild *et al* 2011). Among potential candidates:

- a superfluid design for UHF MRI magnets with He-II cryostable windings; He-I/He-II cryogenic solutions and the use of an external helium quench expansion volume;
- helium vessels with excised/tailored multiple volumes for helium reduction;
- approaches to force management and interface friction mitigation in the main and shielding coils;
- developed large size/high current conductor designs, including RIC;
- homogeneous DP EM design, beneficial for HTS coils with field orientation sensitivity (Schild *et al* 2011);
- UPS-driven B_0 stability with filtering stabilization resistor (HTS magnets, esp. small specialty).

5. Advanced cryogenic solutions

5.1. He-I cryogenics of today: long way to where we are

A knowledge of the technologies and resulting strategies of the past is of utmost importance for our future. To

illustrate this we give the following examples showing the relevance of cooling strategies in the early 1980s that evolved into a very specific framework of boundary conditions for MRI. Once those conditions, together with their experimental verification, are understood within their technological context and re-evaluated in the light of today's rapidly progressing technology, they can more easily merge into other superconducting power applications, or into MRI systems that use HTS technology which, with little effort involved, can immediately lead to novel solutions.

MRI magnets with NbTi-based superconductors still have a major burden—the requirement for liquid helium, requiring a detailed, quantitative energy balance analysis in cryostat design (Stautner 1984, 2012a, 2012b, 2012c). As outlined in the following, the role of cryogenics for MRI systems has changed considerably over the past 30 years and gradually evolved from merely 'facilitating a helium bath for the magnet coils' towards 'magnet integrated cryogenic solutions' that require changes to the magnet itself.

The three main drivers for cryogenic changes were the technical progress in cooling equipment, the cost of liquid helium and the voice of the customer. In the following the cryogenic evolution of different magnet cooling design concepts is shown. Interestingly, several paradigm shifts took place over the years starting in the 1980s. One of the very first 3 T MRI systems featuring a 93 cm warm bore was built in 1985 by Bruker and delivered to the customer. At that time the cryostat basically consisted of an unshielded main magnet in a liquid helium bath (so-called bath-cooled mode), with one thermal shield (half-floating) and an outer vessel filled with liquid nitrogen. If properly designed the floating thermal shield settles at a temperature of 40–50 K, resulting in a heat load to the magnet of typically >1 W. This type of cryostat is
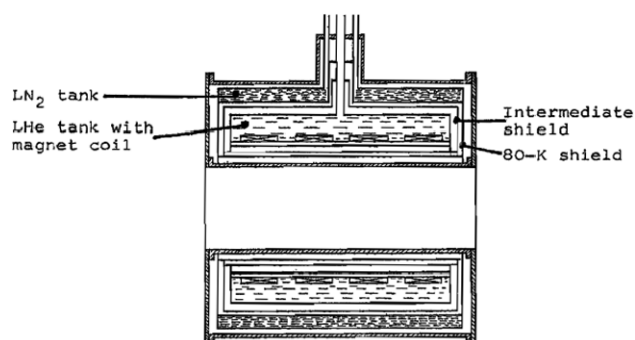
Figure 49. State of the art 'OPEN' cryostat with an unshielded magnet. Reproduced with permission from Forth (1986). Copyright 1986 Elsevier.

a so-called 'OPEN' system, since it boils-off liquid helium to the atmosphere that at the same time very efficiently cools the main turrets and penetrations leading from RT to the helium vessel, as shown in figure 49.

For the first time researchers had a 3 T system at their disposal with a manageable cryogenic infrastructure requiring only monthly liquid helium top-ups with liquid nitrogen refills every two weeks. Several cryocooler manufacturers already produced Gifford–McMahon (GM) type coolers, but mainly for military applications and for cooling cryopanels (Airproducts, CTI and Leybold). Soon after the nitrogen vessel on MRI units was equipped with a cryocooler that considerably increased the liquid nitrogen service interval.

What followed after 1985, however, was a decade of lasting uncertainty on how the cryogenics roadmap would develop, with what ideas it would be populated and what the best cooling route would finally be.

Although dual and single-stage GM type coolers were already available on the market, the way to link them

to the cryostat was not immediately evident (e.g. with respect to cold sink, vibration, magnetic shielding) and their cooling power still remained inadequate to cool a thermal shield surface area of 10–15 m^2. Besides, multiple GM coolers had to be mounted in the patient room, resulting in an increased acoustic noise level. Both Philips Cryogenics (www.stirlingcryogenics.com/) and Leybold Vakuumtechnik, when approached by the MRI manufacturer, had different ideas. Philips, in particular, had close links to the Netherlands-based Stirling company, a company that produced robust coolers for liquefaction of industrial gases with a good market in developing countries.

Philips Cryogenics proposed four main technical routes to solve the cryogenic cooling problem of MRI systems, each of which had their intrinsic weaknesses and strengths (Philips NPB-S&I-Cryo). Figures 50–53 show several interesting design principles and approaches for MRI.

The Leybold concepts were slightly different (see figures 54–56) and made use of their in-house capability of manufacturing efficient and robust single-stage and dual-stage cryocoolers. This design concept involved a so-called coldbox in which the cryocoolers and heat exchangers are housed to supply cryogens to the respective thermal shields.

Most of these design concepts saw two cryocoolers installed in a separate cryogenic coldbox in the utility room, requiring large sized cryogenic transfer lines leading to the MRI unit. The coldbox design, especially for the liquefaction requirement, was sophisticated but bulky and complicated, featuring multiple complex heat exchange units, requiring chilled water cooling, exhibiting a considerable noise level, particularly with the installed Stirling type cooler, and transmitting strong vibrations to the sensitive outer cryostat shell.
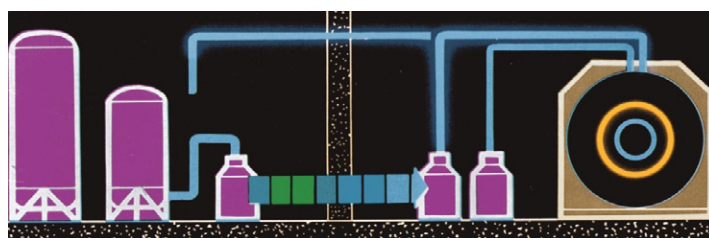

One fill line for filling liquid nitrogen in the outer thermal shield, one fill line for topping up liquid helium and for cooldown from 77 K to 4 K, cooldown of thermal mass takes up to 5 days, starting with filling LN$_2$ into the helium vessel.

Figure 50. Helium bath-cooled MRI system and liquid nitrogen (both cryogens with auto-refill). Reproduced with permission from Philips.
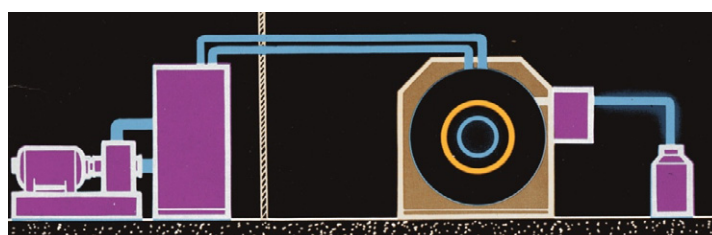

Two options: either LN$_2$ on outer shield (right LN$_2$ dewar) (inner shield at 40 to 50 K), or refrigeration cooling of outer and inner shield.

Figure 51. Conventional compressor–expansion refrigeration cooling (two thermal shields), 'OPEN' helium bath. Reproduced with permission from Philips.
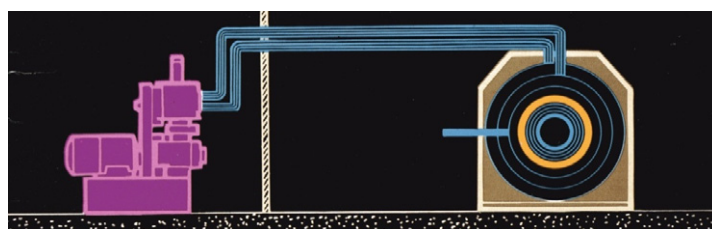
Semi-closed-loop system using a cryogenerator for separately cooling two thermal shields. Since the 2nd thermal shield approaches a very low temperature of 20 K, the liquid helium boil off is comparatively small < 50 ml/h).

Figure 52. Philips PGH 107 Cryogenerator based on the Stirling cycle principle supplying forced flow helium gas through two thermal shields, keeping them stable at 80 and 20 K. The system is open to boil-off liquid helium to atmosphere. Reproduced with permission from Philips.
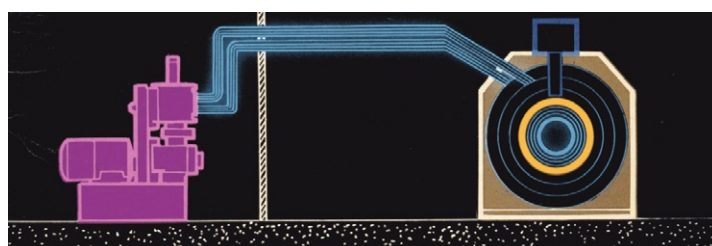

One of the world's first closed system designs, forced flow for thermal shield cooling, recondensing unit attached to helium vessel for zero boil off.

Figure 53. Philips cryocooler supplying two thermal shields with an attached recondensing unit. CLOSED system. Reproduced with permission from Philips.
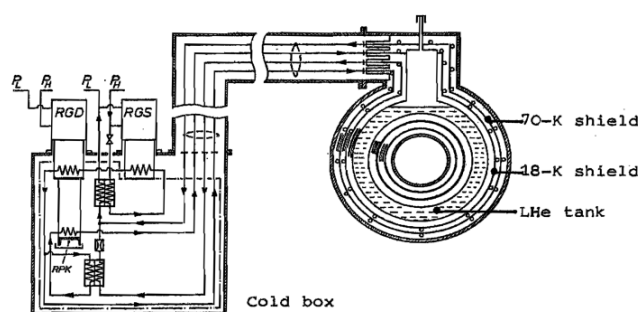
"OPEN" cryostat connected to coldbox via transfer line for cooling 2 thermal shields.

Figure 54. Leybold dual-shield refrigeration system for MRI with an external coldbox (Forth 1986). Copyright 1986 Elsevier.
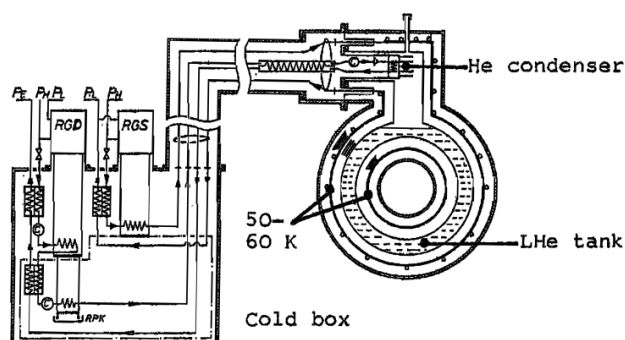
"CLOSED" cryostat connected to coldbox via transfer line for cooling one thermal shield and recondensing. Since the thermal shield temperatures were higher than in the previous figure, the recondensing unit had to be powerful > 1.5 W.

Figure 55. Refrigeration system with an external coldbox and integrated helium recondensation unit (Forth 1986). Copyright 1986 Elsevier.

Many of these different concepts were tried and tested by the cooler manufacturers in the laboratory only, but never made it to customer.

Pressured by the MRI industry, the cryocooler manufacturers started to develop cryocoolers in a cooling power range useful for thermal shield cooling. While striving for compactness and cooler efficiency, while avoiding transfer losses, the cryocooler had to be brought closer to the magnet and tightly integrated into the outer vacuum case (OVC) of the MRI unit, actually becoming part of the magnet. The cryocooler had to have a cooling power of at least 30–40 W @ 40–50 K on its first stage and 10 W @ 20 K on its second stage.

As the dual-stage shield cooler technology advanced, the second-stage temperature was reduced from 10 to 4 K by better cooler optimization and gas flow control, but mainly
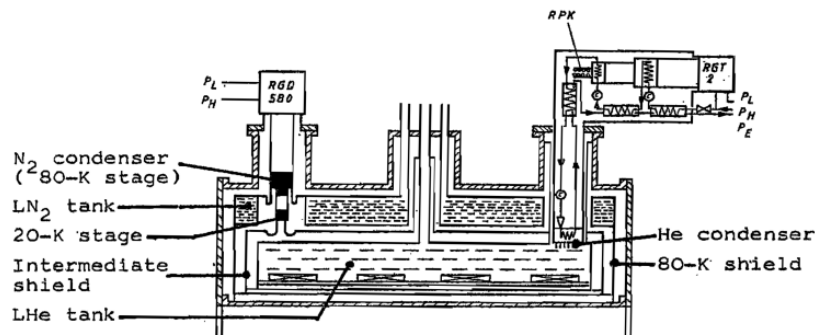
Zero boil off design with dual-stage GM coldhead for shield cooling (note liquid nitrogen tank) and separate recondensing unit requiring a much lower liquefaction rate (20 K intermediate thermal shield).

Figure 56. 'CLOSED' MRI magnet cryostat with an 'early' refrigerator version offering a direct closed-cycle cooling system. Copyright 1986 Elsevier.

by introducing a new rare earth material in a ball shape, exhibiting specific heat peaks that matched the c_p of helium.

5.1.1. 'Open' or 'closed' MRI system? With the introduction of powerful dual-stage coolers that brought the intermediate thermal shield temperature down to 20 K, liquid helium consumption was drastically reduced to 35–50 ml h^{-1} in the best cases. This led to safe liquid helium top-up intervals of >1 yr for a cryogenic MRI system, depending on the mode of operation. Due to the long liquid helium hold time this technology was favored for a very long time until the first reliable 4 K cryocooler of a new player, Sumitomo Heavy Industries (SHI), became available, delivering cooling powers in excess of 1 W @ 4.2 K. It was GE, as the technology leader, that set the pace in the MRI industry by first introducing an entirely closed system able to recondense evaporating helium for 1.5 T systems (Katsuhiko *et al* 1996, Chen 1997, 1998).

An equally important advantage that came with single-stage cryogenics was the sudden gain in extra space available for the coil envelope, as the single thermal shield allowed smaller cryogaps between the vacuum vessel and the coils. Not only did it allow expansion of the room temperature bore of the magnet, thus increasing patient comfort, but also made shorter, compact magnets feasible (alternatively, given a fixed magnet length, expansion of the coil envelope can be used towards cost reduction of the magnet). Initially, this technological breakthrough was not immediately accepted by competitors, since the higher cost of the 4 K cryocooler and the reduced ride-through time had to compete with the annual topping up cost of the liquid helium level (Morrow 2000). In addition, techniques had to be developed that enabled coldhead swapping while the magnet is at field and cold. GE decided on an evacuated sleeve approach, whereas Siemens and Philips left the cooler exposed to a helium gas environment.

The voice of the customer eventually decided on an MRI system with no loss of helium, and today's MRI systems are capable of liquefying helium in a 'closed' mode. It is a good example of how a single technical and strategic decision of a main MRI player can change the landscape of MRI systems, opening up further design space for novel application-dependent, dedicated solutions, hand in hand with the cryocooler manufacturer.
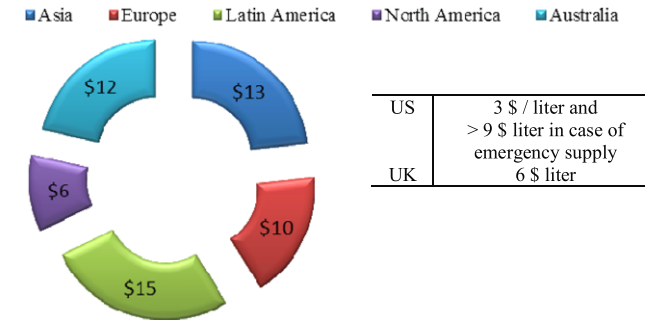

Figure 57. Cost of helium around the world—as of 2010—continental and for selected countries (based on authors' estimates).

5.1.2. MRI cryogenics: going green. European MRI manufacturers noticed as early as 2002 a growing and disturbing uncertainty on the projected supply and cost of liquid helium. Consequently, the first projects aimed at thinking of a new way of saving helium for MRI magnets, coining the acronym MHIT (Minimum Helium Inventory Technology). These efforts have been documented in Atkins *et al* (2009) ('in order to reduce the cost of working cryogen (helium) consumed, its volume in the system is minimized'), for example in Gilgrass (2009) (dry magnet) and in Belton (2006), where a reservoir volume of 80–100 l is envisaged (see also Philips (Ackermann and Menteur 2011)). These designs have been widely explored, even in the past, as will be shown later on, but not implemented yet. Still, the volume of liquid helium for a fully immersed, MRI bath-cooled magnet of today is approx. 1600–2000 l. This cost, the added cost for magnet cooldown, cost for ride-through to customer, as well as for cryostat top off at the customer site, is substantial. Figure 57 shows the cost of helium in selected areas of the world as of the beginning of 2010, based on the authors' estimates. Table 5.1 gives feedback obtained from large users of helium (Nutall *et al* 2012).

To further reduce the cost of helium, sophisticated cooldown concepts were developed and deployed in MRI manufacturing sites worldwide, especially for reducing and minimizing cooldown transfer losses (e.g. using rotary-valve-based transfer siphons).

The next paradigm shift now dawns on the horizon, targeting a drastically reduced liquid helium volume with

Table 5.1. Large user feedback (using $> 2500 \, l \, month^{-1}$)—helium usage, prices and availability (Nutall *et al* 2012).

Large user feedback
Accounted for 86% of liquid helium used
A constituency of 44% of respondents
Average use $76\,500 \, l \, yr^{-1}$
Typical He budget $> US\$ \, 200\,000 \, yr^{-1}$
92% have seen recent price increases
Average increase of 36%
Worst-case price rise of 74%
36% have had an interruption to supply
55% had been put on allocation
The average allocation was 63% of previous usage
58% had liquefier on site

Prices and availability	
Sum of annual He usage (l)	919 000
Average of annual He usage (l)	76 583
He cost per liter—min.	US$ 2.50
He cost per liter—max.	US$ 4.35
He cost per liter—average	US$ 3.43
Most recent price—min.	US$ 3.62
Most recent price—max.	US$ 5.65
Most recent price—average	US$ 4.51
Average price increase	36%

a fraction of what was required in the past, saving both helium and the energy that is required to extract it from natural gas resources (max content of helium in natural gas is ∼7%). Those different technically competing and cryogenically challenging concepts and emerging trends are now outlined in the following.

Good engineering practice, which is in line with GE policy of going green, and the sustainability of magnet systems led to a continuous effort to develop minimum cryogenic inventory technology.

5.2. Toward future MRI: low helium volume cryogenics

The roadmap for minimum helium inventory technology (MHIT) is still emerging and several routes seem possible.

The 'ideal' goal for an MRI manufacturer would be a fully sealed, push-button operated, self-contained cryostat, which would use only a fraction of today's liquid helium reservoir and remain hermetically sealed under all operational regimes and pressures, with no cryoservice required and no vent arrangement present on site. Multiple technologies could be employed on the roads to low helium or fully-sealed MRI magnets.

5.2.1. Solutions for helium volume reduction. In table 5.2 we briefly collate ongoing advanced (top) as well as possible future activities (bottom); table 5.3 comprises the technological efforts and anticipated benefits when implemented in an MRI system.

Any future MRI cooling system will most likely be a mix of those combined technological efforts outlined in the tables, either near-term, advanced or even disruptive. It goes without saying that any technically feasible implementation requires in-depth cost reasoning. Once the main route has been chosen then technical corrections and design changes will be difficult to rectify and implement in volume production.

The first two items in table 5.3 are obvious, but nevertheless difficult to implement. Changing the helium vessel envelope around the MRI magnet, for example, does not seem technically challenging when choosing today's metal forming processes, but comes with a cost penalty. Several attempts have been made and documented in patents, such as those on support columns (Kruip and Mann 2008) and on convective flow (Astra 2007). In 1997, Oxford Instruments (Stables *et al* 1999) built a cryostat vessel with a shape consisting of wide rectangular channels that are in close proximity to the coil pocket structure of the main magnet. On the superconducting wire side, some of the properties can be enhanced to deliver a higher stability margin, which would also allow a higher circumferential temperature gradient. A team of scientists at the Kurchatov Institute and at Bochvar (Keilin *et al* 2011) recently proposed doping the SC wire with rare earth compounds, (e.g. $HoCu_2$, $CeCu_6$, $CeAl_2$, PrB_6) and

Table 5.2. Minimum cryogen inventory technology for MRI.

Advanced cryogenics	Application
• Cryogenic heat pipes *(without/with nanowicking structures)*	Dedicated cooling of hot spots and cryogenic components (e.g. dry SC switches, current leads), coldhead to thermal shield heat pipe link, magnet with embedded 'cryo-vascular/arterial spreaders for surface cooling'
• Cascading heat pipes *(heat pipes in parallel, e.g. nitrogen, hydrogen, neon)*	Reduced magnet cooldown time, push-button actuated requiring no user intervention (part of user-invisible cryogenics)
• Passive thermosiphon *(bubble transport)*	MRI and NMR units
• Cryogen-free cooling *(conduction-cooled)*	Whole body (see figures 8 and 22), limb size HTS magnets, head-only magnets
Disruptive cryogenics	Application
• Active thermosiphon *(self-induced liquid flow circulation)*	Mainly magnet cooling, shield cooling
• Pulsating heat pipe *(active bubble/liquid flow circulation)*	Thermal shield cooling, magnet cooling, cooldown, thermal link and switches
• Antigravity flow and other lifts *(wicking flow)*	Thermal shield cooling, magnet cooling for DRY and WET systems
• Novel heat pipe designs *(Thermoacoustically driven)*	Mainly for thermal mass cooldown

Table 5.3. Strategies and trends for reducing helium cost on MRI systems.

Technological effort	Benefit
Change helium vessel design	Reduces helium volume and consumption
Use of displacers in the bath-cooled magnet system	Reduces helium fill volume
Tailored high I_c LTS wire with good temperature stability margin (4.2–4.5 K, thermal gradient)	Reduces the quantity of coolant helium
Thermal storage battery concepts	Reduces helium consumption for transient operating conditions and ride-through
External cryocooler backup platform	Reduces helium consumption during ride-through
Heat pipe technology and family	Minimizes the amount of helium required
External helium gas storage	Capture helium gas and re-liquefy
Increase cryocooler cooling power, maintenance interval and reduce cost	Conduction-cooled system either 1 or 2 cryocoolers required
New cryocooler technology (embedded PTR with Sterling compressor)	Helium-free technology and multi heat pipes incorporated in PTR technology
Use of medium or high-temperature superconductors	Eliminates the demand for helium as coolant, replace helium with hydrogen
Coil former with wicking envelope	Liquid flow close to winding
Use the natural helium gas boil-off from a minimized thermal reservoir and optimally direct this flow around the magnet	Reduce total helium fill volume to 'puddle' in a bath-cooled system

Table 5.4. Materials suitable as cryo batteries.

Material/operating temperature	Enthalpy H (kJ kg^{-1})		ΔH (kJ kg^{-1})	Mass (kg) required
	20 K	30 K	20–30 K	to store 1 MJ
Water ice	0.615	2.330	1.715	583
Lead	0.368	1.042	0.674	1484
Rubber	0.770	2.320	1.550	645
Glyptal	0.670	2.200	1.530	654
Araldite	0.608	1.688	1.080	926

ceramics (Gd_2O_2S, Gd_2O_3) with a high specific heat at the wire operating temperature. A similar approach using GOS (gadolinium oxysulphide) was taken by Thomas of SMT (Beasley and Thomas 2008). The concept of rare earth components contributing to enthalpy stabilization of a composite superconductor was also mentioned early on by Rosenblum in his 1977 survey (Rosenblum *et al* 1977) measuring 2.5×10^{-2} J cm^3 for the temperature range 2.5–4 K with 7.2 wt% Gd_2O_3. Woolf, on the other hand, proposed heavy fermions as a thermal stabilizer for superconductors in 1987 (Woolf 1987).

5.2.2. Displacer technology. Displacer technology aims at substantially reducing the liquid helium volume requirement around the MRI magnet by inserting displacer elements. Those elements can be mechanical elements that can be used beneficially during MRI operation and cooldown. Other elements may consist of small non-floating spheres or cryogenic foam structures that are filled into the helium vessel or embedded on the magnet itself during assembly. However, this is accompanied by an additional cost for cooldown to 4 K of those structures, caused by the high enthalpy that most of the materials in question exhibit. Any seemingly practical solution needs to be carefully scrutinized and proved experimentally without compromising operational reliability and safety at all operating conditions.

5.2.3. Storing 'cold' at down times, the need for phase transition elements. The cost and availability of liquid helium in underserved and remote areas in the world and the so-called 'ride-through' time for MRI magnets, that is the time that elapses from the MRI unit leaving the factory to reaching the customer site for installation, poses a severe problem for minimizing liquid helium consumption. Furthermore, coping with transient heat loads to the MRI system, either during operation (heat loads due to gradient pulsing) or during cooling power outages, requires an intelligent solution to bridge this time span.

A plausible solution would be a substance that is able to act as a heat sink whenever external cryocooler supplied cooling is unavailable. Indeed, a number of those materials are easily available and can be used as thermal batteries, for example by painting them directly onto the thermal shield surrounding the magnet (see table 5.4). In the event of no cooling being available the material absorbs the radiative and conductive heat from the OVC and efficiently prolongs the liquid helium hold time. Once all the helium has evaporated these substances potentially keep the thermal shield temperatures low enough, mainly below 77 K. Above 77 K, thermal battery concepts have hardly any value unless there is an additional sorption capacity embedded on the thermal shield that is able to keep the vacuum at very low levels well below the Smoluchovski threshold (10^{-4} mbar).
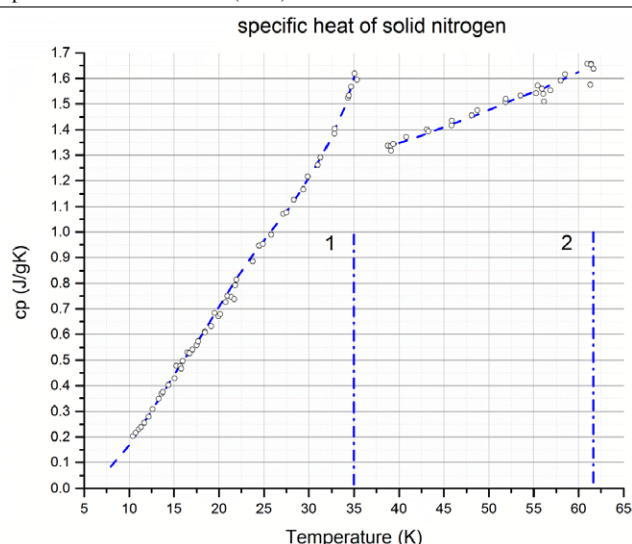
specific heat of solid nitrogen

Figure 58. Anomaly of C_p of solid nitrogen ($T_{\alpha \to \beta}$ and triple point T_{tp}) (Scott 1976, Johnson 1960).

If this is not the case warm up will be more rapid, but rise linearly above 77 K.

In table 5.4 are listed some promising materials suitable for thermal storage in the 20–30 K range.

Once the cryocooler is operational again the thermal shield with its battery feature is cooled back to the operating temperature (e.g. 45 K), presumably during non-operating hours. For higher heat load absorbance more advanced solutions are required.

5.2.4. Advanced thermal storage materials (phase change materials PCM). Reportedly Iwasa (see Haid *et al* 2002b) and Jones (see Hales *et al* 2005 and Hales *et al* 2006) looked at liquid PCMs for high-temperature superconducting magnet applications. Nitrogen in particular has unique features (Scott 1976).

Solid nitrogen exhibits an $\alpha \to \beta$ phase transition at 35.6 K. This phase transition may be attractive for MRI and NMR LTS magnets since the thermal shield temperature for MRI systems with low heat ballast is in this temperature range. This application can be two-fold, used for both the thermal shield and the magnet coils. The latter would save helium during a quench when the magnet energy is dumped into this thermal reservoir (the other phase transition point is at 63 K, the melting point of solid nitrogen).

Figure 58 depicts the two distinct phase change temperatures (1 is the C_p-anomaly, 2 is the melting point) accompanied by a peak in specific heat.

In theory, the energy that can be stored is substantial during this phase transition when cooled to lower temperatures (Scott 1976), however, experiments at the Clarendon Laboratory have shown that the thermal contact between solid nitrogen and the contact surface needs to be optimized. Most likely a finned or finely meshed heat exchange structure would be promising, similar to what is used in activated carbon sorption pumps. Generally, solid nitrogen has a very poor thermal conductivity. As mentioned above, Y Iwasa and H Jones of the Clarendon Laboratory looked at ways

of exploiting this anomaly. While the team at Oxford successfully investigated the use of solid nitrogen for HTS MHD ship propulsion (Hales *et al* 2006), B Haid and Y Iwasa, together with a Korean team, not only thought of traditional NMR and MRI LTS applications using solid nitrogen as the primary battery, but expanded this idea further, including secondary heat capacitors such as ammonia and other gases such as argon (Haid *et al* 2002a, Sugawara 2002). Several patent filings have recently been recorded showing the general practicality of this approach in the future, for example Atkins *et al* (2009); Nakagome *et al* (1992).

So far we have been concerned with reducing helium consumption and fill volume on standard systems only. If liquid helium is supposed to be saved drastically, for example, reducing it from 2000 l to a fraction of that amount (5–50 l), a more radical design approach is required that calls for fundamental changes to the magnet structure and eliminates the traditional helium vessel surroundings, moving from an bath-cooled system to heat pipe cooled designs.

5.2.5. Heat pipe technology. Cryogenic heat pipes are introduced when heat transfer by thermal conduction is no longer efficient, for example when thermally linking the cryocooler to a coldmass over long distances aiming to maintain a very low ΔT. Prenger 1997 (see also Prenger *et al* 1996) showed that cooldown of solid structures can be greatly improved and accelerated by utilizing heat pipe technology. Heat pipes reduce cooldown times by 40–50% in LTS systems. Heat pipes deliver an advantage because the first stage of the cryocooler has much more cooling power than the second stage. During cooldown it is useful to shunt as much as possible power to the second stage. Within the operating temperature range 63–123 K, nitrogen heat pipes drastically increase the heat transfer to the first stage of the cryocooler. When the temperature of the heat pipe drops below the triple point of the working fluid, the working fluid freezes, effectively stopping its operation. In order to extend the operating temperature range of heat pipes at the high end, recent designs favor a cascaded system using ethane-filled pipes mounted in parallel with oxygen- or nitrogen-filled pipes. When the first stage (ethane) pipe freezes, the second stage continues to provide thermal shunting until they too freeze out.

Further benefits of heat pipes in cryogenics are:

- they are hermetically closed and can be directly placed into a vacuum environment;
- maintenance-free structure;
- no moving mechanical parts;
- a performance increase using nanotechnology is possible.

For MRI systems, Siemens (Rieger 2004) reportedly discussed the cooling of MRI components using heat pipes, as shown in figure 59.

Heat pipes are also used for cryopanel cooling of large vacuum chambers (Chandratilleke and Ohtani *et al* 1997). The same technology ('cryo-vascular approach', an arrangement of multiple heat pipes) applies for dedicated
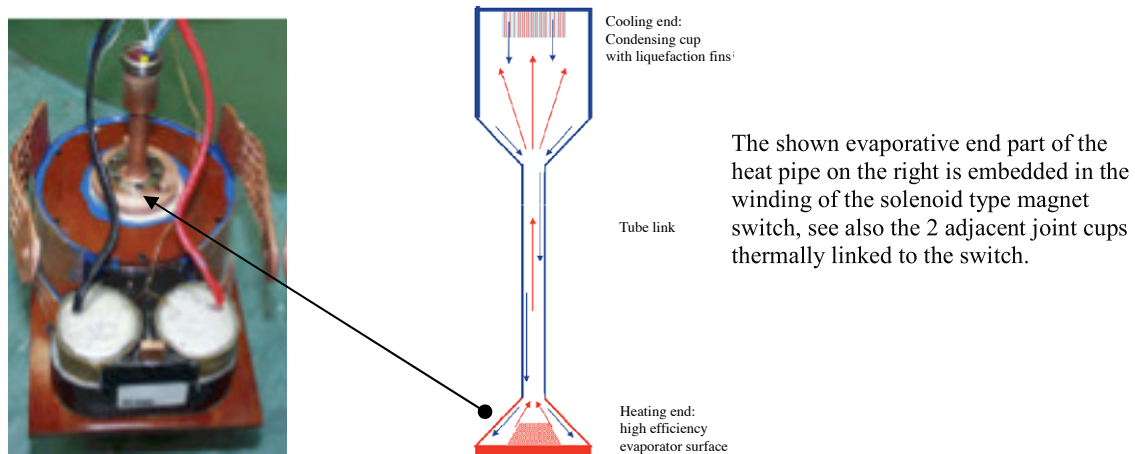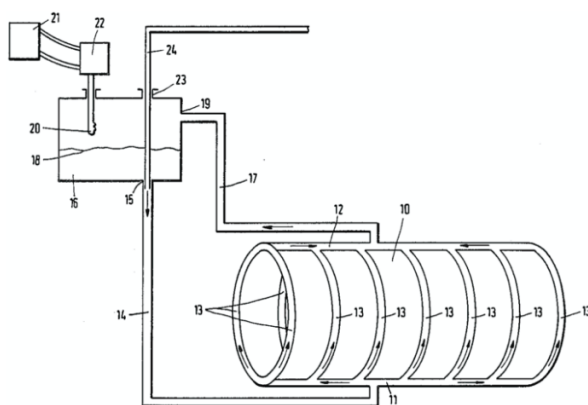
The shown evaporative end part of the heat pipe on the right is embedded in the winding of the solenoid type magnet switch, see also the 2 adjacent joint cups thermally linked to the switch.

Figure 59. Heat pipe cooled 'dry' superconducting switch for MRI. Reproduced with permission from Siemens.

The liquid reservoir depicted on the far left allows liquid helium run through the downer line. A manifold at the bottom of the MR magnet splits the flow into several branches and collects the escaping vapor at the top where it is then fed back to the reservoir. The reservoir is equipped with a cooler that reliquefies the helium gas keeping the liquid level in the reservoir constant.

Figure 60. Typical MRI thermosiphon cooling approach.

thermal shield cooling of known hot spots in the interior of a MRI magnet and, in particular, when the cooling magnet supports (suspensions) or embedded current leads; more generally speaking, whenever heat sinking contact needs to be improved. Recently, a number of cryogenic heat pipe patents have been filed for various thermal shield cooling methods, including different cryocooler connections. The introduction of a new cooler type, the pulse tube cooler, opens further avenues towards total heat pipe and cooler integration (Skye *et al* 2008). It is safe to say that heat pipe technology for cryogenic applications is going to further increase in popularity. Nanotechnology, in particular, is expected to help in increasing the efficiency of heat pipes by developing sophisticated wicking structures for liquid helium and hydrogen (Zhang *et al* 2012).

Heat pipes are usually pre-charged with high-pressure gas and cooled to operating temperature, liquefying at the top end and evaporating at the heat exchanger surface at the bottom of the connecting tube (see figure 59, right). A special case of a heat pipe is the so-called thermosiphon, a device that utilizes a two-phase fluid in its risers and downers, typically filled with >90% liquid content. Unlike the heat pipe that was used mainly in small lab experiments, the simpler thermosiphon technology has a far longer application history and was first reported for efficiently reducing the boil-off of a spherical hydrogen container in 1964 (Elrod 1963). Since

then, thermosiphon technology has been used successfully for cooling superconducting magnets for large accelerators, and most recently for small MRI HTS magnets (Stautner *et al* 2011).

The team at the research center at Karlsruhe (FZK, now KIT, Germany) and Dustmann (1986) were the first in 1985 to propose cooling of an MRI magnet employing thermosiphons. The basic principle is shown in figure 60.

Since then, an increasing number of patent filings have shown a trend towards this type of MRI magnet cooling, e.g. (van Hasselt 2006; Atkins *et al* 2007; Yoshito *et al*).

In summary, the use of thermosiphons in MRI and NMR magnets is very attractive for several reasons.

- The thermosiphon structure requires at best ~5–50 l of liquid helium as compared to 2000 l.
- No requirement for a helium vessel structure. Substantial cost benefit plus improved coil envelope space.
- Overall heat load reduction to the cryostat:
  (a) the size of the MRI magnet is reduced;
  (b) the weight is minimized;
  (c) the number and size of penetrations from room temperature (RT) to 4 K is reduced.
- The coolant is now close to the winding.
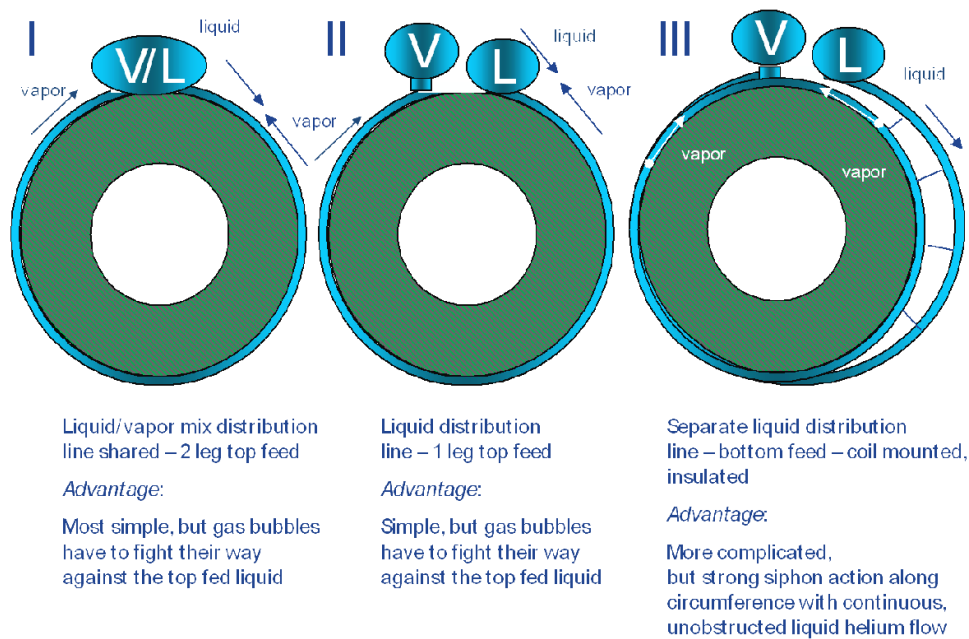- The coolant is self-adapting to transient heat loads.

Figure 61. 'Static' or 'passive' thermosiphon cooling options (V = vapor, L = liquid).

- Safety requirements and installation construction are relaxed, no need for a quench line, no coding approval required.

Several main principles for incorporating thermosiphon technology have emerged for use in next-generation MRI and NMR systems: one that is more or less passively driven by bubble transport and buoyancy forces, the other, more important, one is able to initiate a continuous flow loop of liquid helium with reasonably high mass flow rates and without any external mechanical pumping requirements.

5.2.6. The 'passive' thermosiphon. Figure 61 shows the thermosiphon implementation on an MRI system with different pipe routings and the respective advantages (to cool the magnet cartridge of an MRI unit at least four of those tubes need to be placed along the *z*-axis and additional tubes for the shielding coils). Note that the helium reservoirs are split into a siphon liquid supply and gas capturing reservoir. For reasons of clarity the connecting line to the liquefying cryocooler is not shown. This is similar to a conventional system, where the cryocooler liquefaction fins receive the helium gas flow and redistribute the condensed helium back to the liquid reservoir. Passive thermosiphons are by far simpler to install on an MRI system than active siphons (Stautner 2007).

5.2.7. The 'active' thermosiphon. So far only the static mode of the thermosiphon has been considered, merely governed by density-driven gas bubble transport. However, for higher heat loads—under certain conditions—efficient gas bubble transport is restricted due to the size of the gas bubbles causing flow friction and possible temporary flow instability, reducing the thermosiphon efficiency.

In this case, either the system operating pressure has to increase to reduce the bubble size, the tubing diameter

Table 5.5. Minimum thermosiphon tube dimensions.

Calculation of tube diameter in mm	Fluid	
	Helium	Neon
Bubble movement	0.58	1.17
Siphon performance	2.434	1.262

has to change, or a completely different concept needs to be introduced, namely the *dynamic* or '*active*' thermosiphon. Agglomerated bubbles can remain motionless unless provided with a channel of sufficient diameter. The dimensionless Eötvös number must therefore be greater than 3.37, or correspondingly the channel diameter must be greater than 0.58 mm, as shown as an example in table 5.5. The helium bubble reaches its maximum vertical rise velocity in a channel of 5 mm maximum dimension (the required minimum diameter for helium at 4 K is given in table 5.5) and needs a channel inclination of at least 5° to maintain that velocity in liquid helium. This was recently confirmed again by experiments at Saclay (Gastineau *et al* 2012, Baudouy *et al* 2013). The transition to film boiling at about 0.9 W cm^{-2} and subsequent hysteresis effects prevents the return to nucleate boiling until a surface heat flux of 0.17 W cm^{-2} is reached. Reducing surface tension also reduces bubble size. Figure 62 illustrates a common room temperature thermosiphon design known to work efficiently for domestic warm water heater (cold water supply from top of tube).

It is not commonly known however, that the above principle works extremely well at cryogenic temperatures, as well as for a multitude of applications. In this design we are primarily circulating liquid helium accompanied by a small percentage of micro bubbles only (see figure 63). Furthermore, this mass flow rate is self-adapting. Once a transient heat load is applied to a thermosiphon, flow

Figure 62. Historic 'basic' physical model of an active thermosiphon.
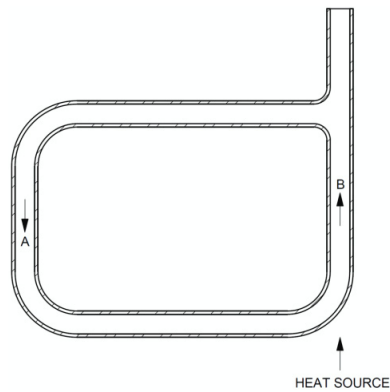
"Heavier" cold water flows down from the top supply tube and is being heated at one end of the tube leg (at the burner) locally creating a substantially "lighter" fluid. As soon as heat is applied, a flow circulation is induced efficiently transferring heat from B to A due to the density differences created, as indicated by the arrows.
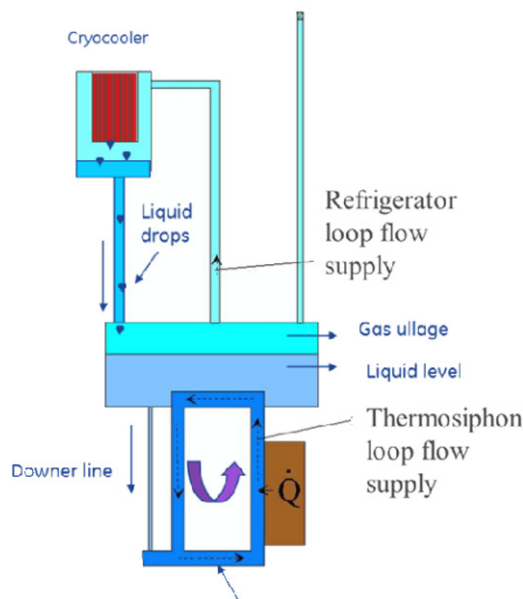
Figure 63. Example of an active cryogenic thermosiphon.

Figure 64. (a) Measured thermal conductivity of a PHP with different fill media, heat from the bottom and fill ratio of 50% (Natsume *et al* 2012): Copyright 2011 IEEE. (b) Possible implementation of PHPs in an MRI cryosystem (Stautner 2012a, 2012b, 2012c).

circulation and heat transfer increases. As previously mentioned, this may be particularly important when switching gradients in MRI systems (fast EPI sequences) and for quickly removing heat loads imposed on the magnet.
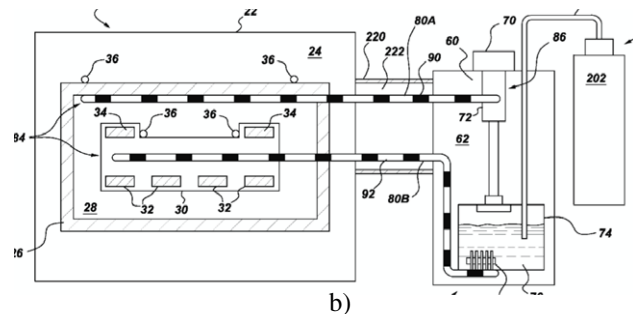
Reports also indicate an excellent performance down to slightly above 1.8 K (Hofmann 2012). Below the superfluid transition at the lambda point of 1.8 K, other mechanisms capable of producing a flow, for example, the thermomechanical pump (fountain pump) as described by Hofmann, can be used. This principle was successfully tested for cooling a large Tokamak type fusion magnet, e.g. large coil task project (LCT) (Kasthurirengan and Hofmann 1998, Stautner 2012a, 2012b, 2012c).

Details on thermosiphon operation have also recently been published by van Sciver (2012).

5.2.8. Pulsating heat pipes. Since its introduction by Akachi (see Akachi and Polasek 1995), this promising new type of heat pipe has quickly been welcomed in cryogenics, mainly for cooling HTS SMES with cryogenic liquids such as

hydrogen, neon and nitrogen. PHPs work even well for LTS applications with helium as the main coolant.

The PHP consists of a meandering capillary tube filled with gas bubbles and liquid portions that can be thought of mass oscillators providing an oscillating flow towards the liquefaction surface (Stautner 2012a, 2012b, 2012c).

Figure 64 shows one of the very first experimental results (Natsume *et al* 2012) revealing the potential for HTS MRI or for other component cooling as a cost efficient alternative with respect to high-purity metals as a thermal link. Figure 64 a shows the performance of open loop pulsating heat pipes (OLPHP) with 1/8–1/6 in diameter. For reference,
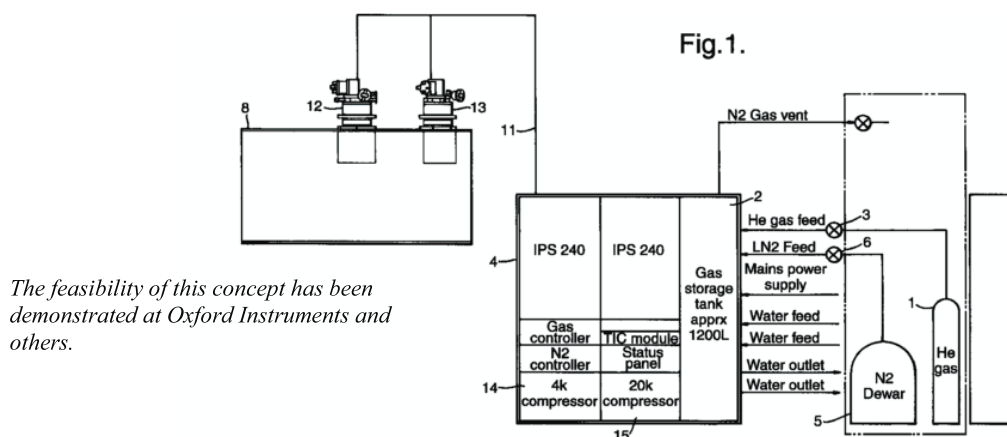
Figure 65. Gas compression and external gas storage (Stables *et al* 1999).

the thermal conductivity of Cu with RRR = 100 in field of 1 T at 20 K is about 2000 W mK^{-1} (Natsume 2011). Figure 64(b) shows the implementation on an MRI system with PHPs (dotted line) connected to the first and second stage of a cryocooler (Stautner 2012c).

For a general overview of the genealogy of passive two-phase systems, see (Khandekar *et al* 2004).

5.2.9. External helium gas storage for normal operating conditions (NOC). Heat load reduction to the MRI magnet cryogenic environment is of utmost importance. Not only does it generally increase the ride-through time, but it also helps to extend the service life of the cryocooler (MTBF). For regular operation the GM cryocooler with its >1 W cooling capacity at 4.2 K can cope with normal heat loads. Additional heat loads can be expected, however, when running aggressive sequences such as EPI on a gradient system on 3 T, 7 T or higher MRI magnet systems (Dietz *et al* 2011). To cope with this excess liquid helium, which is then boiling off, a temporarily external capture may be envisaged. The gaseous helium can then be reclaimed again at operating times with lower additional heat loads (at night) and re-liquefied from RT.

External storage of helium requires a permanently installed umbilical cord from the helium reservoir to the storage device. For MRI systems those storage devices need to be quite large, due to the helium liquid to gas expansion ratio (1:700). For storage device reduction a gas compressor is envisaged that could be installed in the MRI maintenance room.

5.2.10. Advanced MRI cryogenics. 'Advanced MRI cryogenics' reduces the liquid helium inventory from 2000 to 5–50 l by introducing heat pipe technology, as discussed above, creating a basically 'near-dry' type, conduction-cooled magnet with a fast quench spreading zone. Loss of vacuum in the cryosystem triggering a quench, for example with typical heat flux densities of 4–5 W cm^{-2} and 0.6–3.8 W cm^{-2} in the case the vacuum collapse (Lehmann 1978), no longer requires satisfying the safety ordinance efforts of a 2000 l helium

vessel and greatly reduces the design and build cost of an MRI system.

Further benefits are (comments in brackets refer to the specific cost-saving items).

- Absence of the helium vessel (cost of design, material and build, acceptance test obsolete, pressure vessel FEM not required, reduced cooldown mass).
- Cryostat access turret diameter reduction (less material, reduced heat loads, no safety risk).
- Quench vent piping minimized (smaller diameter, easy routable at customer site).
- Minimized helium inventory (less helium cost, no safety measures required for the customer, e.g. oxygen monitor becomes obsolete).

External or internal helium quench gas storage leads to significant interest.

5.2.11. Helium gas storage during a quench for advanced MRI systems. Should the MRI magnet dump its energy into the helium bath (usually a heat load of up to 15 MJ for 3 T systems), the helium gas can be captured in external storage tanks (see figure 65) or large inflatable bags. The gas from the inflatable bags can then be compressed into standard gas bottles and shipped back to the gas supplier. After quench, the magnet requires quick re-cooling to its operating temperature and back filling of its designed storage volume. Cryomech, for example, recently reported a helium liquefaction rate of 32 l d^{-1} from room temperature with a 4 K pulse tube cooler (Wang 2009) instead of two 4 K 1.5 W GM type coolers producing 6 l d^{-1} with an electrical power of 15 kW (Sumitomo Heavy Industries Catalog). A. Hofmann was the first to discover the greater potential of gas liquefaction from RT using a PTR, as compared to the GM cooler, by exploiting the longitudinal tube temperature profile. A typical example of an early dual-stage 4 K four-valve pulse tube cooler of GM/Matsubara type is shown in figure 66 (Hofmann 2003).

If the total MRI liquid helium reservoir were 500 l instead of 2000 l it would still take 14 days for refilling and a further
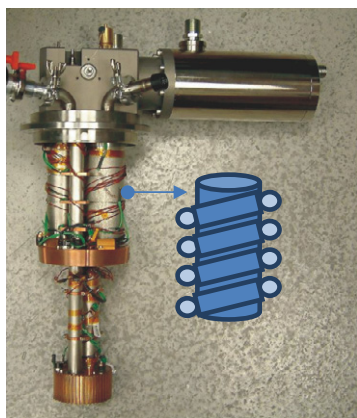
Figure 66. Fully instrumented prototype PTR showing a possible liquefaction path along the tube length (in blue). Cooler design parameters: fully welded design; no magnetic shielding required; no buffer volume; same geometry as 4K SHI GM cooler; no noise; no vibration (PTR in side-sock); self-balancing wear-free rotary valve; liquefaction fins incorporated on second stage. (Reproduced with permission from Hofmann and Stautner 2005.) Copyright 2005 IEEE.

Figure 67. Embedded current leads in a turret (Steinmeyer *et al* 2002). Copyright 2002 IEEE.

thousand liters for cooldown to the 4 K operating temperature, which is not acceptable to the customer.

However, for future MRI systems with much smaller cryo-inventory quench gas capturing becomes feasible.

This way quench gas can also be conveniently stored and reclaimed internally within the vacuum space of the MRI magnet, the ultimate goal of a truly 'closed' and 'green' MRI system of the near future.

5.3. Component cooling

Amongst the most important components of an MRI magnet system are the current leads (CL) required to ramp the magnet to field and the persistent current switch (PCS).

5.3.1. Power leads for MRI. Over the years, engineers have come up with innovative solutions that minimize the heat loads during and after completion of the ramp, in the steady state. To reduce the ramp heat load, most of the current leads take advantage of heat exchange with the escaping helium gas from the MRI reservoir.

Traditional clinical systems have for a long time utilized retractable leads that are inserted from the atmosphere into the cryostat, and retracted once the magnet ramp is complete. The leads penetrate the helium vessel and make contact with the sockets at the 4 K level. Obviously, such a 'penetrating' solution may not be compatible with the discussed helium-vessel-less options of a 'dry' conduction-cooled or limited helium reservoir magnet. Alternative advanced current leads solutions have been looked into that allow supporting the 'closed magnet' design.

5.3.2. Embedded normal metal current leads for MRI applications. Rather than exposing the MRI magnet to atmosphere to insert the current leads, they can be fully
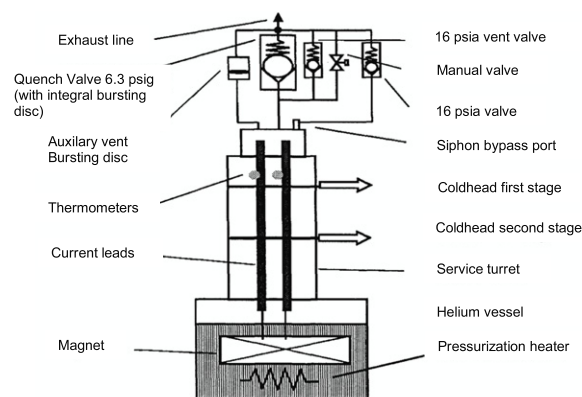
embedded in the magnet structure, which is advantageous for a number of reasons.

- No need to depressurize the helium vessel/reservoir for CL removal.
- No need to open the cryostat and expose it to the atmosphere. The cryogenic system remains leak tight and icing is avoided.
- A fully automated ramping process is feasible.

Embedded leads made of brass, copper, aluminum or other alloys require vapor cooling during ramping to reduce the heat load to the magnet and to be able to force the operating current through the leads. This requires a dedicated venting system on the cryostat turret on conventional MRI systems, designed to address the required level of redundancy and safety, see figure 67 for a typical MRI turret component arrangement (Steinmeyer *et al* 2002).

A neat solution for an embedded lead is given by Scurlock (2006). The current lead is wrapped around a cryostat service turret to reduce the current lead height and increase the thermal path from RT to 4 K (see figure 68). During ramp, heat exchange on the tube inner surface is increased, whereas the current leads themselves remain in a vacuum space.

Vapor-cooled current leads also come in different shapes with enhanced heat transfer characteristics (Chang *et al* 2006). Alternatively, the main cryostat turret itself can be used as a current lead in a conventional MRI system, further details are found in Belton *et al* (2006); White and Steinmeyer (2005).

As will be shown later, current leads preferably need to be placed in close proximity to a heat sink, e.g. the cryocooler. Conveniently, even the cryocooler itself can be thought of as a current lead (Steinmeyer and Kramer 2000) or heat pipe, as Daugherty and his team report (Daugherty *et al* 1995).

A novel, low heat load HTS lead wrapped around a support tube structure that uses a nitrogen bath at the warm end during ramp has recently been proposed by GE (Huang *et al* 2006) and is shown in figure 69.

Adiabatic, indirectly cooled metallic current leads for NMR and MRI magnets were investigated and modeled successfully as early as 1960. Vapor-cooled current leads

Figure 68. Vapor-cooled current lead on a cryostat turret (500 A, spiral wound leads, total length 150 mm between 300 and 4 K). Reproduced with permission from Scurlock (1988). Copyright 1988 Elsevier.
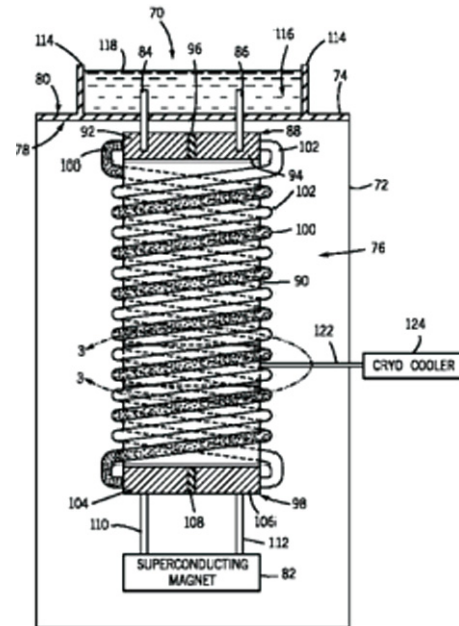

Figure 69. HTS spiral wrap current lead.

on the other hand still seem to attract considerable research interest, especially for applications requiring very high currents >55 kA. Cooling of leads in the 10 kA range and higher require additional heat exchangers and sophisticated helium counter flow techniques. For most MRI applications, the amperage ranges from 100 to 1000 A only, depending on the particular MRI application and magnet design. For optimum performance CFD calculations are recommended to detect the occurrence of local hot spots and gas pockets within tubular vapor-cooled current leads at tube bends and heat intercepts. A careful design is recommended to avoid severe magnet quenching issues during ramp and in operation (the so-called 'hot gas quenching' phenomenon). During ramp, a tubular current lead requires an unrestricted gas flow, free of ice and nitrogen condensation.

The typical heat flux through a pair of optimally sized adiabatic copper leads (in vacuum) from RT to 4 K amounts to approx. 84 mW A^{-1} (Wilson 1982), whereas the same pair would burden the cryostat with only 2.2 mW A^{-1}, if vapor-cooled. This optimum value, based on thermodynamic calculations, however assumes perfect heat transfer, a boundary condition which in practice is difficult to maintain along the complete current lead length.

5.3.3. Embedded HTS current leads for MRI applications.
It is commonly accepted that HTS lead technology for the next generation of MRI magnets would reduce cooling costs during magnet ramp and steady state operation. HTS tape manufacturers claim to be able to reduce the ramp heat load by a factor of 100 (Dietrich 2005). While the above figure of 100 may still be ambitious, a factor of 50 seems to be reasonable in the near future. HTS leads eliminate some of the problems discussed in section 5.3.2 concerning adiabatic or vapor-cooled current leads, provided those leads

are properly designed, heat intercepted, mechanically robust in all operating modes and reliable. Those factors are very important, since ramp up/down is not possible with cracked leads (Steinmeyer *et al* 2002). Repair is usually impracticable without warming the magnet up to room temperature. If faults were to occur during operation, a safe and cost-saving magnet ramp down would no longer be possible. HTS leads made of tape stacks are field dependent; if subjected to a perpendicular field on the tape width, the current carrying capacity tends to degrade rapidly (see figure 70) (Kellers 2003).

Although low-cost HTS tubular bulk current leads (Nexans 2004, CAN Superconductors 2012) are available, the stacked tape technique seems to give more robust leads. A metallic shunt or other suitable quench protection is advisable to safeguard against lead burn-out.

Once those criteria are fulfilled at reasonable cost, future, next-generation MRI magnet designs will benefit from this technology. Heat loads during ramping and with optimized HTS current leads could be less than 100 mW in total for the complete assembly, depending on the chosen operating current for a typical MRI unit, the available heat stationing temperature and the vapor cooling rate. Efforts on minimizing the heat loads of HTS leads are still ongoing (Lakrimi *et al* 2007). Figure 71 shows the dogbone type attachment of a current lead pair attached to the first stage of a cryocooler. Above the first stage the current lead consists of a resistive copper or brass lead.

Ballarino gives a good overview on the current state of high-power HTS current leads (Ballarino 2007). Various CL shapes made from different materials and additives, either BSCCO-2223, BSCCO-2212 based or from YBCO or MgB_2, are reported. Trithor for example, used Bi-2223 with an high AgAu content of 4% (Kellers 2008). This kind of doping leads to enhanced electron defect scattering that results in a reduced specific thermal conductivity of the matrix (Schwarz 2009).
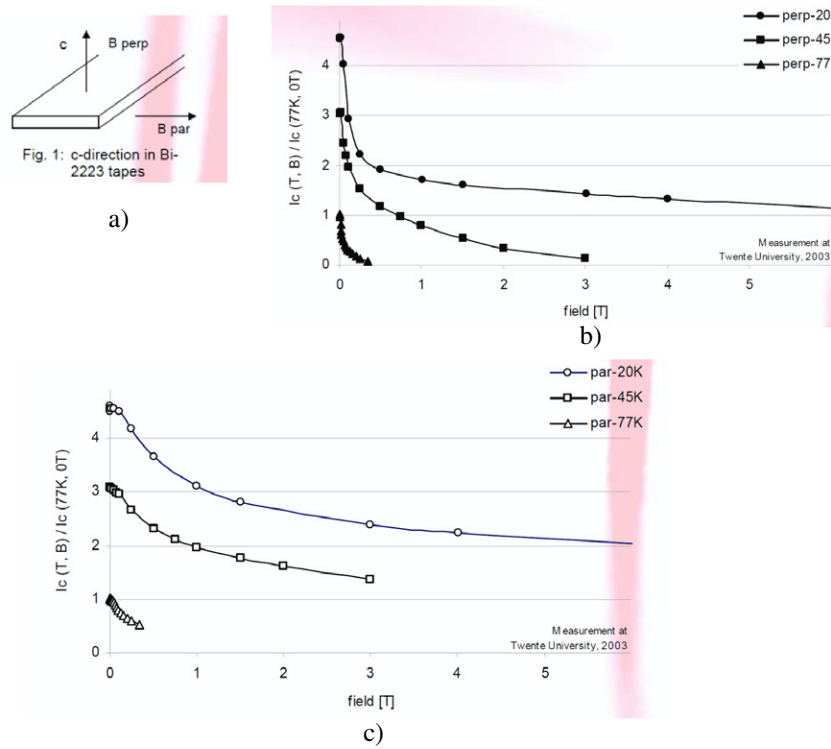
Figure 70. (a) BSCCO tape field orientation dependence, (b) perpendicular field, (c) parallel field (Kellers 2003). Copyright 2003 Trithor.
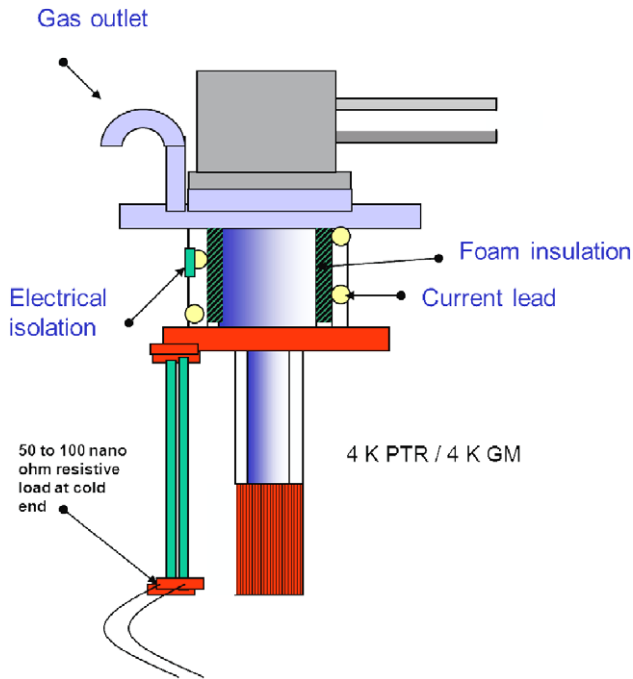

Figure 71. Typical 'Hybrid' current lead, warm end of a HTS lead heat-stationed to the cryocooler first stage. Resistive part extends from cryocooler first stage to room temperature.

5.3.4. Retractable embedded current leads for MRI applications. Retractable embedded current leads can reduce the heat load to the magnet by mechanically disengaging them from the cold magnet after the ramp, either manually with a

sliding seal through the vacuum space itself without breaking the vacuum, by hydraulic actuation (Ennis *et al* 1985) or demountable (Vermilyea and Dorri 1994). In particular, next-generation MRI magnets with low cryogen reservoirs may use adiabatic, retractable leads, situated close to the cryocooler and the thermal shield. Retractable hybrid current leads are feasible as well, in this case the lower HTS part is embedded and the upper, conventional resistive part is retractable (GE patent pending).

5.3.5. Persistent current switches for next-generation MRI units. One of the most important and critical components of an MRI magnet is the superconducting switch connected to the magnet terminals, also called the persistent current switch (PCS), that allows ramping the magnet to the design field (switch in 'open' state) and trapping the field in the magnet ('closed') state. The switch is designed for an intended magnet ramp time according to:

$$L\frac{\mathrm{d}I}{\mathrm{d}t} = V - Ir \qquad (8)$$

whereas V is the ramp voltage when turning on the power supply (PS) (PS arranged in parallel to switch), t is the ramp time, I the electrical current fed into the magnet and r is the sum of the resistances of leads and joints. The generated heat Q in the switch can then be described as:

$$Q_{\text{switch}} = V^2/R \qquad (9)$$

with R as the normal state resistance of the switch. Several design criteria are important, for example the low inductance of the switch itself, the thermal response time,
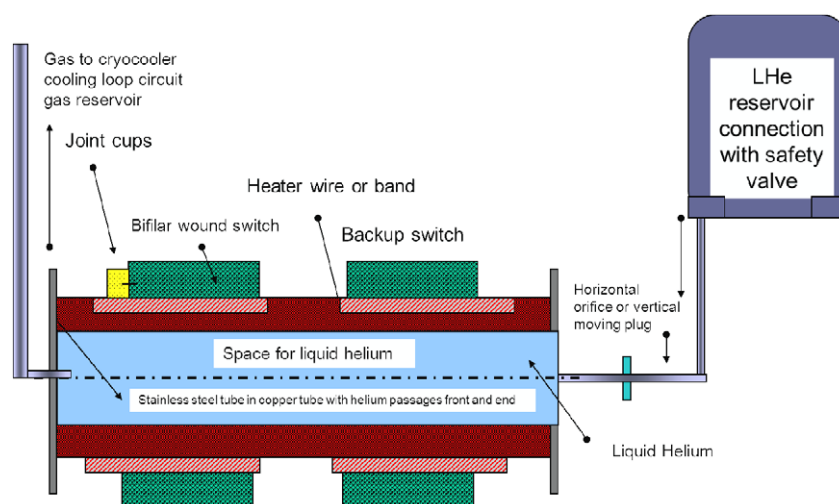
Figure 72. PCS connected to a satellite reservoir (not to scale, switch part enlarged for clarity).

the normalization time, to name but a few. For switch 'opening', a heater may be either incorporated during winding or attached to the superconducting winding of the switch. In helium bath-cooled magnets, even with an epoxy-encapsulated switch, heat transfer to the helium bath is adequate and switching rates are very fast. Switches for dry magnets (Dorri and Laskaris 1995) on the other hand need to be carefully designed to avoid burn-out due to the absence of a helium bath. Overheating and switch wire burn-out is more likely to happen since the thermal resistance of the conduction path, as well as the limited cooling power of the cryocooler, influences the design.

As we have shown earlier, some future MRI systems may employ a very small so-called LHe 'satellite reservoir' (e.g. of 5–50 l). This calls for PCS designs that work in vacuum (conduction-cooled, cryo-free) or designs that tap into this satellite reservoir, either with direct contact to liquid helium or through conduction. Main-reservoir-fed PCS designs featuring their own intrinsic, liquid envelope are feasible and advantageous, since they can conveniently be mounted anywhere in any orientation in low magnetic field regions with exceptionally quick response times in open (normal)/closed (superconducting) states. Figure 72 shows a design implementation of this type of switch. Various design modifications enable fine tuning the PCS to satisfy the MRI magnet requirements (Stautner 2013b).

5.4. He-II cryogenics for MRI magnets

5.4.1. He-II technology for NMR and ultrahigh-field MRI.
Sub-cooling of bath-cooled magnets is done to get significant advantages in the design due to the extended critical parameters of superconductors at lower temperature.

- An increase in the maximum critical field B_{C2} (T_{op}) makes systems feasible with higher B_0.
- An increase in $J_c(T_{op})$ allows operation at a higher I_{op}/I_c ratio, with superconductor savings.

- For the wire, the amount of superconductor within the wire (fill factor) is increased.

For high fields, about 11 T, the critical current of NbTi wire wound solenoids cooled with superfluid helium at 1.8 K corresponds to that of Nb_3Sn at 4.2 K (Warner 2008, Liebel 2011, Claudet and Seyfert 1981).

Cryogenic disadvantages are the cost increase (COE, cost of energy) in the cryogenic infrastructure to maintain the MRI/NMR system at specific operating temperatures over long operating times. UHF MRI systems in general can benefit from existing high-field NMR magnet technology as outlined in the following.

Ultrahigh-field magnet technology—the GHz race is on. Varian, Oxford Instruments and Bruker, as well as the University of Tsukuba and NHMFL (see figure 76), started to compete neck on neck for the first 1 GHz system.

It is now widely expected that the newer Nb_3Sn conductors will permit 1 GHz NMR magnets to be made of NbTi and Nb_3Sn. This would require persistent operation at a field of about 23.8 T in a material with an upper critical field of about 28–29 T at the operating temperature, a truly challenging but attainable goal'. Shortly after the above statement made by Larbalestier (Scanlan *et al* 2004), Bruker won the race and in July 2009 announced that the world's first GHz magnet had gone to field (warm bore size 54 mm). The first unit was installed at Centre de RMN à Très Hauts Champs à Lyon, France.

Development history in brief. This project started back in 1984 in collaboration with the Research Centre Karlsruhe, Institute of Technical Physics, who had been working on high-field magnets with Nb_3Sn inserts for years (Turowski *et al* 1980), pioneering the delicate wind and react process of the required Nb_3Sn inserts. In particular a magnet designed for Mößbauer-spectroscopy experiments achieved an unprecedented maximum central field of 13.9 and 14.16 T close to the conductor at 4.5 K in early 1980. As early as 1990, Turowski and Schneider reported on the design and operation of the world's first 20 T superconducting magnet system and
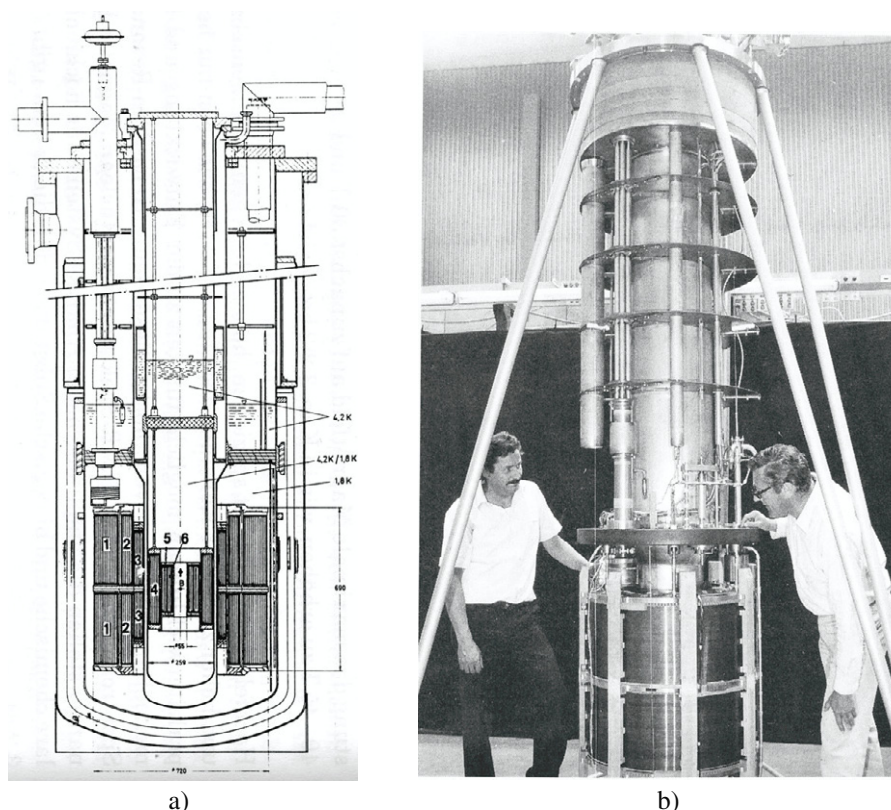
Figure 73. (a) Pumped cryostat for a 20 T magnet (Turowski and Schneider 1990) showing the inner Nb$_3$Sn sections; (b) hybrid 20 T magnet as of 1989 (Turowski and Schneider 1989). Reproduced with permission from Noe (2012). Copyright 2012 ITP/KIT.

its future prospects (Turowski and Schneider 1989, 1990). They describe a superconducting hybrid system consisting of a NbTi outer magnet and several Nb$_3$Sn insert magnets which used multifilamentary Nb$_3$Sn conductors. Figure 73 shows their compact advanced magnet system operating at 1.8 K.

Building on this success at FZK, a 750 MHz NMR magnet prototype, followed by a product introduction seemed to be an achievable, although challenging goal. Bruker had already produced 500 MHz NMR systems since the early 1980s, but this first step towards Nb$_3$Sn insert technology was considered very challenging.

Moreover, to achieve 17 T with the wire available at that time, a new cryostat design was required that subcooled the helium bath to a temperature low enough to achieve the design field. Lessons were learnt from the Saclay team, especially from their 'Marinette project' (Lottin 1981) and other French collaborating groups working on the Tore Supra project (Claudet and Aymar 2007) that had reported progress on He-II cooled superconducting magnets 15 yr earlier. With increasing field strength requirements the NMR system development roadmap had to commit to a wire development with a reliable partner. Kobe partnered with the superconducting wire supplier JASTEC, whilst Oxford Instruments, competing with Bruker, received wires from Oxford Superconducting Technology OST for their NMR program, Bruker recently decided to acquire Vakuumschmelze, expanding the long-term relationship with this company (now EAS), and knowing about their capability in developing Nb$_3$Sn wires with very

high current carrying capacity, tailor-made for the next generation of ultrahigh-field NMR magnets. On December 5th, 1992, the first new magnet type went to a field of 17.62 T, corresponding to 750 MHz (Müller *et al* 1992a, 1992b, 1993a, 1993b). Further development is presented in figures 74 and 75.

Cryogenic challenges: UHF would not have been possible if not for the earlier development and in-depth analysis done by the scientific community and their shared expertise. See, in particular, the work published in Kan *et al* (1980) and Roubeau (1975) on cryogenic pumping requirements; in Mardion *et al* (1978), Claudet and Aymar (2007), Mardion and Senet (1979a), van Sciver (2002) and Hilal (1980) on heat transfer; in (van Sciver 1978, McClintock 1978, Augueres *et al* 1980) on He-II vertical cryostat design; in Faure-Brac and Grenber (1984), Elsner and Klipping (1973) on pumping speed; and in François and Lottin (1979), Wilks (1967), Lottin (1981) on pumping requirements.

A key part in the design is the refrigerator line. Typical lines are shown in figure 77 and normally consist of a precision needle valve delivering an annular flow passage, a filter block made of sintered metal and an appropriately designed heat exchanger (Mardion and Senet 1979a, 1979b) as well as a means of eliminating any possible film creep at the suction point.

Figure 78 shows the dual bath design chosen by Oxford Instruments/Varian group. This basic principle was first published in 1981 by the Williams/Iwasa team (Williams *et al*

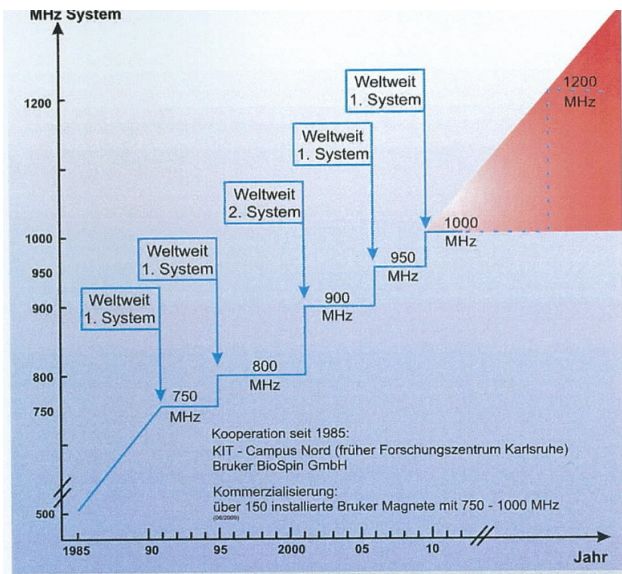**Figure 74.** NMR Bruker product family tree (Goldacker *et al* 2002).

Figure 75. NMR milestones of collaboration effort. Reproduced with permission from Noe (2012). Copyright 2012 ITP/KIT.

Table 5.6. Typical field strength and approximate stored energy of NMR magnets versus operating frequency (Larmor frequency: 42.576 MHz T^{-1}).

Operating frequency (MHz)	Field strength (T)	Stored energy (MJ)
200	4.7	0.018
400	9.4	0.219
500	11.747	0.45
600	14.1	1.25
750	17.62	5
1 GHz	23.5	26
1.3 GHz	30.533	tbd.

MRI with $E_{stored} > 100$ MJ, due to the much larger bore size of the MR system.

5.4.2. Outlook for MRI. Ultrahigh-field MRI magnet systems will draw from the experience gained with the high-field pre-clinical NMR systems discussed herein and will combine cryogenic and magnet technology. Examples are shown in figure 79, depicting a subcooled tomography system for the Neurospin project in France, delivered by Bruker in 2007 (21 T system in preparation), and an Agilent 16.4 T wide bore system.

As mentioned before, a subcooled magnet system improves the properties of the superconducting wire provided the temperature stability of the bath itself is maintained and the coolant is close to the winding.

Subcooled MRI systems require continuous pumping on the 4 K He-I bath to maintain a constant temperature gradient for 2 K operation. The pumping flow cannot currently be recondensed with a cryocooler, requiring external gas storage.

1981). The design requires direct pumping on the 2.2 K bath, filling back from the He-I reservoir. The cryostat diameter is slightly increased, whereas the Bruker system requires a greater room height since the He-I bath is designed above the He-II bath. In this case the He-II bath and the He-I bath are thermally isolated from each other (Müller *et al* 1992a, 1992b, 1993a, 1993b).

In the product, the above concepts need to also ensure safe operation in case of a quench. Table 5.6 depicts typical stored energies, which represent a fraction of typical UHF
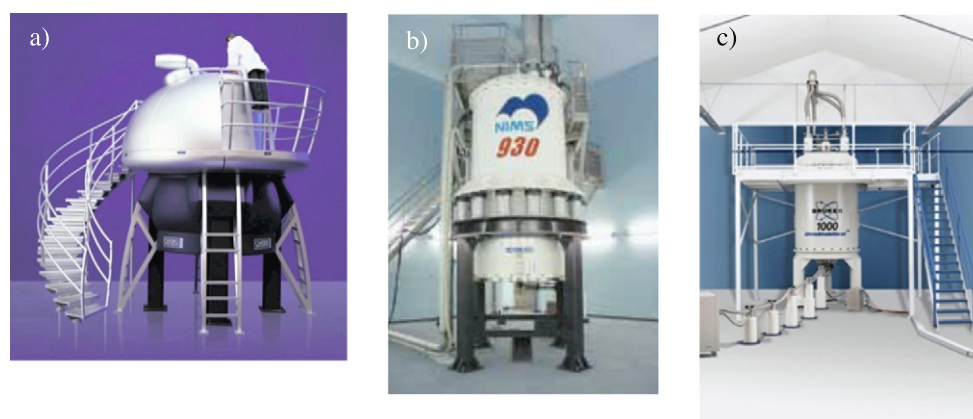
Figure 76. Ultrahigh-field magnets, the three main competitors. (a) Oxford Instruments 900 MHz (reproduced with permission of Oxford Instruments); (b) NIMS 930 MHz (Tachikawa 2012) (reproduced with permission of NIMS) and (c) Bruker 1 GHz (reproduced by permission of Bruker).
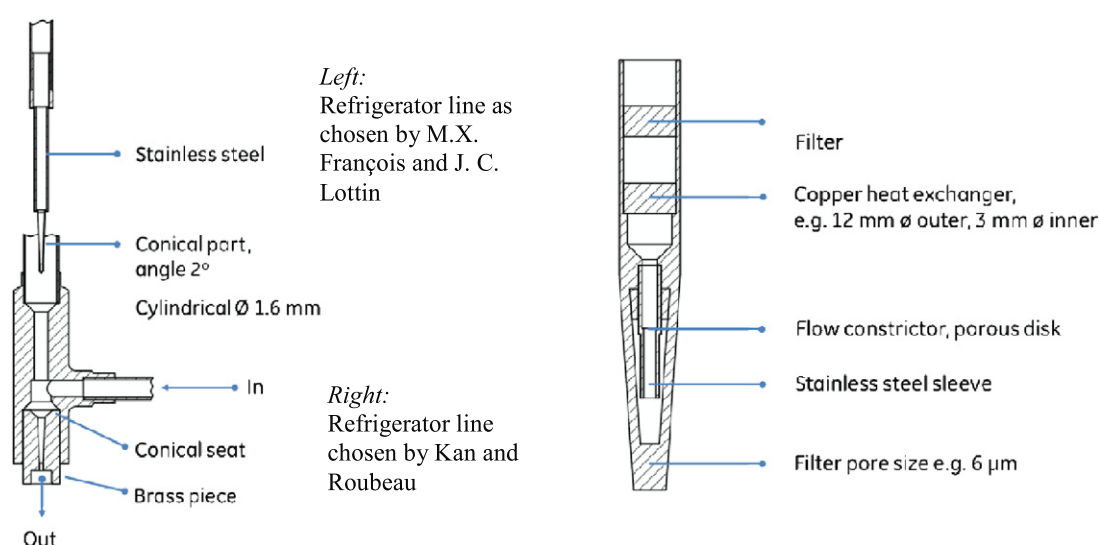

Left: Refrigerator line as chosen by M.X. François and J. C. Lottin

Right: Refrigerator line chosen by Kan and Roubeau

Figure 77. Typical refrigerator lines and choices.

The technology now culminates in the largest MRI magnet, ISEULT, constructed for research use at the Neurospin Centre, which will be using a stand-alone cryoplant with He-I/He-II cooling system (see section 4.2). If successful, it may stimulate use of the He-II option in other, smaller, MRI UHF whole body systems.

5.5. Non-traditional cryogenics—hydrogen economy

5.5.1. Hydrogen economy: elements applicable to MgB_2 MRI/MRI 'going green'. With the arrival of the first superconductor wire available with a T_c close to 18 K, namely Nb_3Sn (Matthias *et al* 1951), Nb_3Ge (Matthias *et al* 1965) and V_3Ga (A15 compounds), subcooled liquid hydrogen was thought to replace the costly helium. But, even before that time, indeed cryoresistive non-superconducting magnets based on copper and aluminum were cooled with liquid hydrogen (Schauer *et al* 1970). Liquid hydrogen pre-cooling was also used successfully for the superconducting ANL bubble chamber magnets (Brechna 1973). In the early 1960s

liquid hydrogen was used as a thermal shield for a large spherical helium vessel (Elrod 1963) and even earlier a 500 l LH_2 experimental dewar was in use at NBS (Scott 1959, Scott *et al* 1964). Experimenters then quickly learned that liquid hydrogen is the most advantageous cooling media we know in cryogenics, exhibiting a higher heat transfer efficiency than helium, leading to a faster thermal mass cooldown and drastically lower boil-off (by a factor of 12).

Today, we are fortunate to see the hydrogen economy and infrastructure beginning to take shape, established by the automotive industry and their partners. Hydrogen is not only energy efficient and clean, but also readily available in large quantities at extremely low cost for hydrogen fuel cell cars from all major renewable energy sources and landfills. Durable high-pressure cryogenic storage containers have been developed, as well as the required fueling infrastructure and its safety components, standards and features (LHA). High-purity hydrogen is produced reliably, fast fueling is possible, all safety devices required are qualified for hydrogen
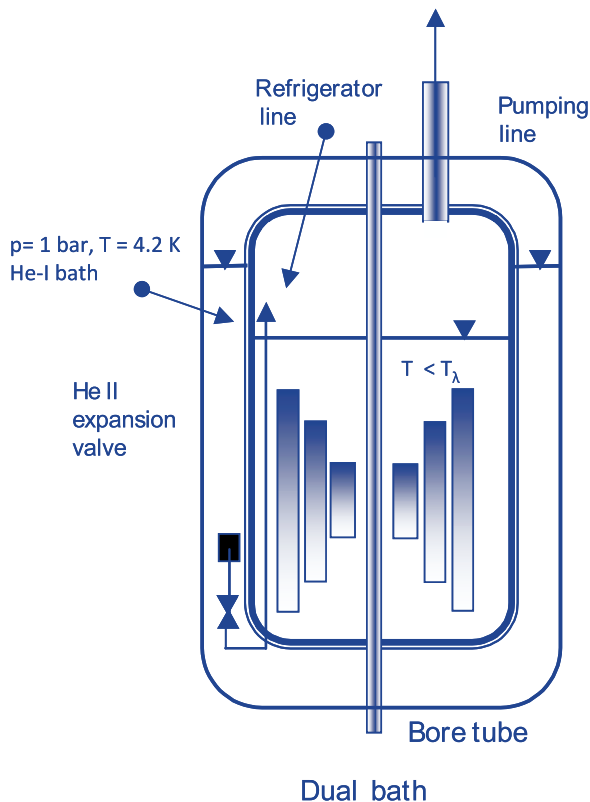
Figure 78. Basic parallel bath design.

use and hydrogen is boiled off safely in garages through relief valves.

The automotive industry may help to overcome the so-called 'Hindenburg syndrome' mentioned by Edeskuty and Stewart (1996), which finally no longer poses an insuperable obstacle to the safe use of hydrogen.

Suddenly hydrogen as a coolant has sparked great interest for replacing costly helium, since now it seems possible to directly embed superconducting magnet systems within this hydrogen infrastructure. Examples are Grant's concept of interconnected hydrogen-based smart grid components (e.g. HTS cables) (Grant 2012) or hydrogen thermosiphon-cooled SMES systems to compensate the power fluctuations of renewable energy components, such as with 5 MW wind generators (Shintomi *et al* 2012), as shown in figure 80.

The medium-temperature superconductor MgB_2 can certainly play a major role in future MRI designs if it succeeds in continuing to increase in engineering current density over time, if the production of long wire lengths is under control and reproducible with consistency of key parameters such as J_c or n-value, if wire costs can be further reduced to the levels of NbTi, and if multifilamentary wire joints can be made successfully during the winding process. Three of those aspects are currently being addressed by the scientific community besides an increase in I_c. Further benefits for the MRI industry are increased ride-through time and reduced cryocooler cost with longer life time, since the costly rare earth in 4 K coolers is no longer required for 10–20 K hydrogen cooling.

5.5.2. Cryocoolers for 'next-generation wire' MRI systems.
If MgB_2 can successfully transition to larger MRI systems, as hoped by the MRI industry, and the hydrogen infrastructure at the same time becomes feasible such that even conduction-cooled small systems appear on the market, the traditional 'shield cooler', also called the '10 K cooler', will receive an overwhelming comeback. Instead of the currently required and available cooling powers of 1–1.5 W @ 4.2 K, now 5.4 W @ 10 K and approx. 13 W @ 20 K will be obtainable, accompanied by a further simplified cryogenic design at reduced cost.

An engineering prototype for limb size MRI application, sponsored by the NIH, is currently being built by the GE Global Research Electromagnetics and Superconducting Magnet Lab team and its partners and will optionally operate in dual mode (liquid helium or liquid hydrogen) (Mine *et al* 2012, 2013).

Figure 79. (a) Neurospin cryo subcooled tomography system. Reproduced with permission of Bruker. (b) Agilent wide bore systems 16.4 T/260 mm–18.8 T/210 mm. Reproduced with permission of Agilent.
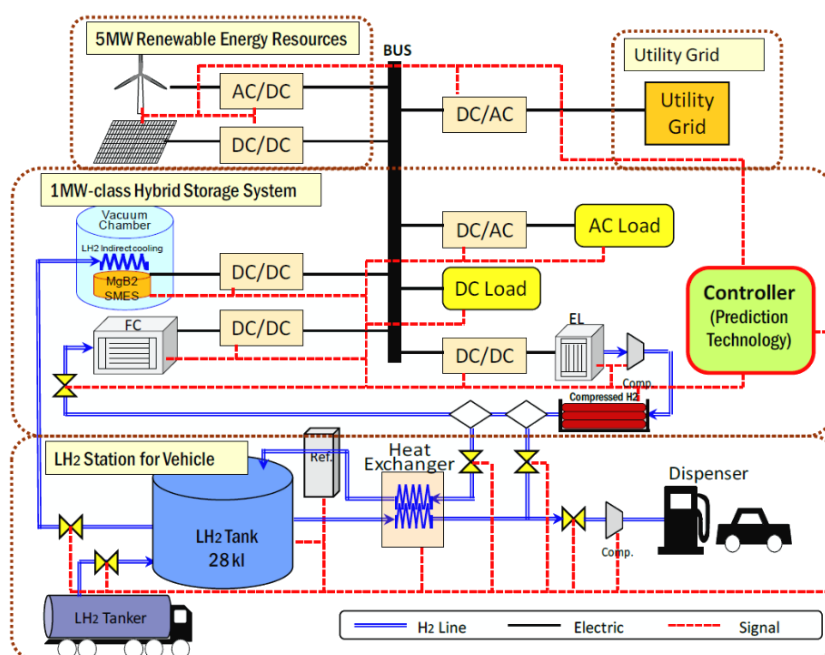
Figure 80. Hydrogen infrastructure serving superconducting magnet systems. Reproduced with permission from Shintomi *et al* (2012). Copyright 2012 IEEE.
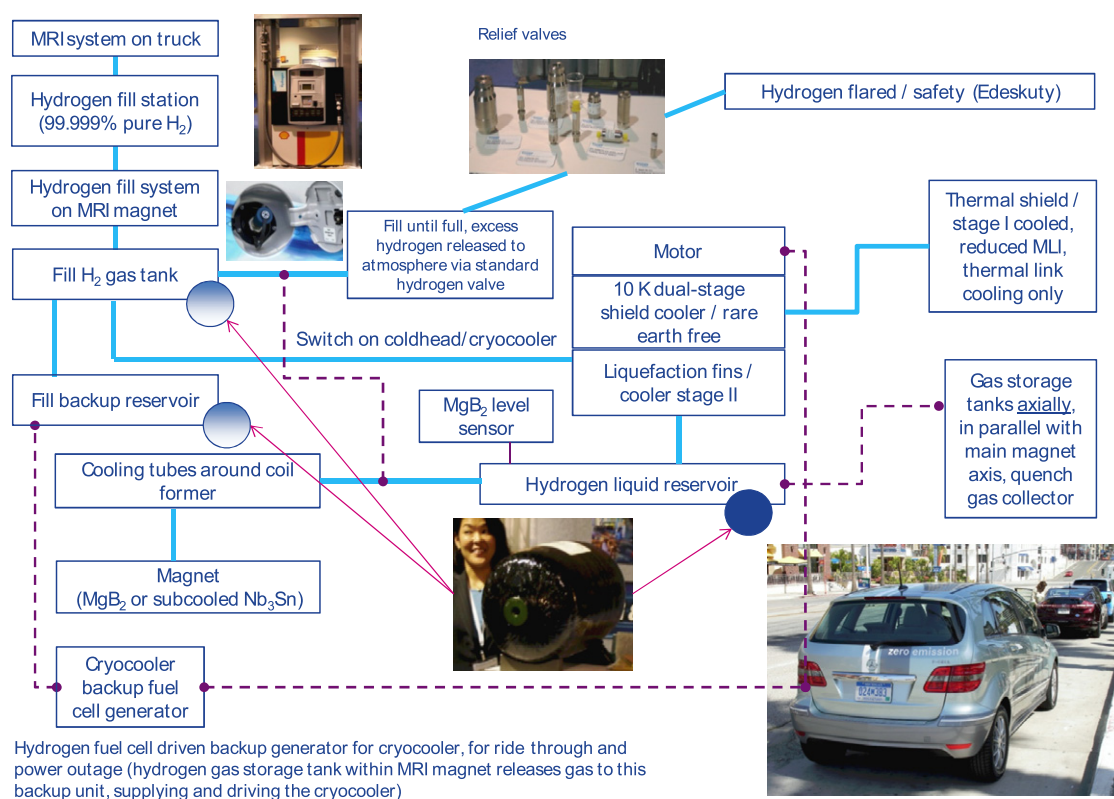
Figure 81. Hydrogen-cooled MRI in H_2 economy.

Figure 81 depicts in what way future hydrogen coolant-based MRI systems will be designed and commissioned, based on a future hydrogen economy (Stautner 2013a). To this effect low helium volume MRI systems will use hydrogen as a coolant instead of costly helium. In a potential scenario future MRI systems can thus be initially filled directly from a conventional hydrogen automotive fueling station. Those existing fueling stations already supply high-purity

Table 5.7. Amount of cryogenic fluid required to cool metals. (Note: σ = ratio of weight of fluid to cool the same weight of metal to the fluid boiling temperature, and required coolant liters required/lb of metal; based on Jacobs' curves (Jacobs 1963).)

Fluid	Helium				Hydrogen				Nitrogen	
Initial metal temperature	300 K		77 K		300 K		77 K		300 K	
	σ	1 lb^{-1}	σ	1 lb^{-1}	σ	1 lb^{-1}	σ	1 lb^{-1}	σ	1 lb^{-1}
Using latent heat of vaporization only										
Aluminum	8.3	30.2	0.4	1.45	0.38	2.42	0.018	0.12	0.83	0.46
Stainless steel	4.2	15.1	0.18	0.65	0.2	1.28	0.0085	0.05	0.43	0.24
Copper	3.9	14.1	0.27	0.98	0.17	1.08	0.012	0.08	0.37	0.21
... and by additionally making optimal use of the enthalpy of the gas										
Aluminum	0.2	0.73	0.028	0.1	0.075	0.48	0.0097	0.06	0.51	0.29
Stainless steel	0.1	0.36	0.013	0.05	0.037	0.24	0.0045	0.03	0.27	0.15
Copper	0.1	0.36	0.02	0.07	0.037	0.24	0.0065	0.04	0.23	0.13

gas for fuel cells. With the fueling technology in place it would then be possible to safely fill the reservoir of an MRI system and start the initial cooldown by exploiting the highly efficient cryogenic properties of hydrogen, as briefly indicated in table 5.7. Safe high-pressure hydrogen fuel tanks (liquid/gaseous), high-quality fueling nozzles, hydrogen safety valves, coolers, hydrogen level sensors and backup fuel cell generators for cryocoolers already exist thanks to the development efforts in the automotive industry (Stautner *et al* 2013).

6. Conclusions

The discussed technologies are presented in table 6.1 according to their relevance in different MR applications.

Conventional technology that comprises tubular magnets with NbTi coils in a helium bath, at present time firmly occupies the dominant position in the whole body imaging market, with B_0 up to 9.4 T. The advantages of a well-optimized, reliable commercial technology at an efficient cost point rightfully secures its present place as the choice for clinical MR scanners.

However, with new dynamics in existing and emerging imaging markets as well as trends in the commodities, particularly helium accessibility and cost, the discussed novel approaches in cryogenics, superconductors and scanner topologies are opening up attractive alternatives in the areas of high field, siteability, and anatomically-specific patient accommodation, that could become prospective candidates for future mainstream cost-efficient MR scanners.

The move to reduce helium usage in MR magnets and the pursuit of closed cryogenics solutions is gaining momentum and, while we are currently at the beginning of this road, it will continue to develop.

In many cases the introduction of novel technologies into a cost-conscious commercial market will be stimulated by growing needs in advanced customized procedures. Specialty scanners, such as orthopedic or head imagers, can lead the way due to the intrinsic advantages in their design. A smaller imaging volume, and reduced weight and coil dimensions, lower the introductory threshold for their cost and risk. Lower inter-coil and intra-coil stresses contribute to improved coil stability. The smaller cryostat size and reduced stored energy that need to be absorbed during quench are conducive to closed cryogenic solutions. A cryo-invisible cooling design that employs conduction or convection loops and never needs a service refill, eliminates duct lines in the imaging room and promotes easy office siting for such specialty imagers. They are also better candidates for HTS/MTS introduction, as their lower superconductor-to-cryostat cost ratio means that the initial higher cost of the new conductor will be easier to offset against the advantages associated with advanced cooling arrangements.

Similarly, the advantages in image quality promised by increasing B_0 to 7 T and higher, and corresponding technologies such as Nb$_3$Sn coils or sub-atmospheric helium and He-II cryogenics have so far been limited to developments for animal and pre-clinical research scanners. Here, specialty head scanners may be the first to open the door for clinical ultrahigh-field MR. The smaller FOV of the dedicated head magnet, as well as its small bore size (albeit sufficient to accommodate a patient shoulders) allow one to scale down the many challenges associated with the compensated solenoid design, improve complexity and cost as well as stray field and siteability, and can help to usher in the new 'decade of the brain'.

As with many other applications, new high-temperature superconductors still have to clear the common hurdle of cost, reliability, stress tolerance and persistent joints, before the commercial use of MR magnets can be attempted. Their maturity in the future can bring significant advantages and enable non-traditional, more open configurations and advanced cryogenic solutions. Rapidly accelerating MgB$_2$ developments, now with its first use in a commercial 0.5 T MR scanner, have made it a realistic candidate as a volume substitute for NbTi in 'cryogenless' 1.5 T/3 T MR magnets in the future. This is still subject to reaching cost competitiveness with NbTi and progress in joint technology; again its

Table 6.1. Magnet technologies: potential in different applications.

Applications	Whole body $B_0 < 1.5$ T	Whole body $B_0 = 1.5$ and 3 T	Whole body high-field	Dedicated head ≥ 3 T	Specialty limb ≥ 3 T	Specialty breast MR	Portable/hand-held
Superconductors							
NbTi	Lowest cost & risk, choice wire at this field	Lowest cost/risk, standard design choice	Standard for 7, 9.4, up to 11.7 T (subcooled). Part of NbTi/Nb$_3$Sn hybrid > 12 T	Choice for $B_0 < 12$ T	Lowest cost & risk, choice wire	Lowest cost & risk, choice wire	Low-field option *j*
Nb$_3$Sn	N/A	N/A	In whole body scanners above 12 T	Inserts at $B_0 > 12$ T	Limited benefits	Limited benefits	N/A
MgB$_2$	Entry for MgB$_2$ into whole body applications	Possible contender with NbTi; cryo-free prospects, cost-driven	No advantage; limited B_{c2}	Potential candidate for cryo-free and LH$_2$	Potential candidate for cryo-free and LH$_2$	Potential candidate for cryo-free and LH$_2$	Candidate for cryo-free
HTS	Limited cost/benefit beyond demos	Long-term perspective; limitations: cost, joints and mech. parameters	High potential for inserts and main coils; present cost and technical limits	Potential future use above 12 T	Long-term perspective; mainly high-field specialty	Long-term perspective; mainly high-field specialty	Long-term future potential
Configurations							
Tubular	Disappearing for $B_0 < 1.5$ T	Clinical mainstream; optimal patient access versus cost	Only configuration presently feasible	Main configuration	Cylindrical or conical	Not feasible unless uses whole body magnet	N/A
Split-open	Primary topology at <1.5 T; intrinsic design penalties; intervent.use	Non-existent at ≥ 1.5 T; distant future with MTS/HTS unclear	Cost/benefits unfavorable	N/A	Limited benefit	Use in whole body magnet	N/A
Planar/disk	Limited by $B_0 < 1$ T and FOV for present technology	Limits may be improved with mature HTS technology	Potentially with HTS only, substantial cost challenge for high B_0	Limited benefit	Limited benefit	Anatomy advantage	Preferred topology
Offset tubular FOV	Limited benefit	Limited benefit	Limited benefit	Anatomy advantage	Anatomy advantage	Limited benefit	N/A
External FOV	Limited by $B_0 < 1$ T and FOV for present technology	Limits may be improved with mature HTS technology	Potentially with HTS only, substantial cost challenge for high B_0	N/A	N/A	Anatomy advantage	Preferred topology

Table 6.1. (Continued.)

Applications	Whole body $B_0 < 1.5$ T	Whole body $B_0 = 1.5$ and 3 T	Whole body high-field	Dedicated head ≥ 3 T	Specialty limb ≥ 3 T	Specialty breast MR	Portable/hand-held
			Cryogenics				
Open boil-off He bath	Older technology, replaced by 0BO	Stepping stone for emerging companies	Limited to NbTi below 9.4 T; or Nb$_3$Sn	Disadvantageous technology	Disadvantageous technology	Disadvantageous technology	Unfeasible—closed cryogenics a must
Zero boil-off He recondensing	Present standard, may shift in future with He cost	Present standard, may shift in future with He cost	Limited to NbTi below 9.4 T; or Nb$_3$Sn	Basic approach, He duct in room	Basic approach, He duct in room	Basic approach, helium connections in room required	Unfeasible—closed cryogenics a must
Sub-atmospheric He	N/A	N/A	Enables NbTi use up to 11.7 T	Extra complexity, benefits unclear, except > 12 T	Extra complexity, benefits unclear, except >12 T	Extra complexity, benefits unclear	Unfeasible—closed cryogenics a must
'Cryogenless', conduction cooling	Potential growth due to He availability; whole body cooling size challenge	Potential growth due to He & new MTS/HTS; whole body cooling size challenge	Potential with HTS only; NbTi/Nb$_3$Sn coils too large for such cooling	Duct-less imaging room advantage	Duct-less imaging room advantage	Duct-less imaging room advantage	Preferred option
'Cryogenless', convection loops	Potential growth due to He availability; conducive in non-tubular topology	Potential growth: He availability & new MTS/HTS; use of other cryogens	Potential with HTS or Nb$_3$Sn coils	Duct-less imaging room; LH$_2$ and other cryogens	Duct-less imaging room; LH$_2$ and other cryogens	Duct-less imaging room; LH$_2$ and other cryogens	Potential use

65

appearance in dedicated specialty magnets may help to speed up that introduction.

New technologies in the areas of scanner configurations with better patient accommodation, invisible cryogenics with minimized helium usage, and novel high-performance superconductors will undoubtedly serve as fertile ground for exciting future developments in superconducting magnet design for an expanding MRI market—the largest commercial application of superconductivity.

Acknowledgments

References

Abele M, Trequattrini A, Pittaluga S, Besio S and Punzo V 2011 Magnetic resonance imaging apparatus with offset imaging volume *European Patent Application* 2284558A1

Ackermann R A and Menteur P A 2011 Tubular thermal switch for the cryo-free magnet *International Patent Application* WO2011/080630A2

Akachi H and Polasek F 1995 Pulsating heat pipe review of the present state of the art *Technical Report ITRI-ERL* Chutung

Ardenkjaer-Larsen J H, Leach A M, Clarke N, Urbahn J, Anderson D and Skloss T 2011 Dynamic nuclear polarization polarizer for sterile use intent *NMR Biomed.* **24** 927–32

Astra E 2007 Apparatus for cooling *US Patent application* 2007/0214821A1

Atkins A F, Gilgrass G and Stautner E W 2009 Apparatus for maintaining a system at a cryogenic temperature over an extended period of time without active refrigeration *US Patent Specification* 7497086

Atkins A F, Harrison S M and Kruip M J M 2007 A cryogenic cooling arrangement and method *US Patent Specification* WO2007003499 A1

Aubele A, Glücklich V, Sailer B and Schlenga K 2010a Verfahren zur Herstellung einer supraleitenden Verbindung von MgB$_2$-Supraleiterdrähten über eine MgB$_2$-Matrix aus einem Mg-infiltrierten Borpulver–Presskörper *European Patent Specification* 2221895A2

Aubele A, Glücklich V, Sailer B and Schlenga K 2010b Supraleitende Verbindung von MgB$_2$–supraleiterdrähten über einen Presskörper aus HTS-Pulver *European Patent Specification* 2221894A2

Aubert G 2011 Method and device for generating homogeneous magnetic field in an area of interest, especially for NMR imaging *US Patent Specification* 7952454

Augueres J L *et al* 1980 700 mm diameter cryostat operating at 1.8 K and atmospheric pressure *Cryogenics* **20** 529–33

Ballarino A 2007 HTS current leads: performance overview in different operating modes *IEEE Trans. Appl. Supercond.* **17** 2282–5

Baranov A N *et al* 2003 Synchrotron radiation study of MgB$_2$ formation under high pressure *Supercond. Sci. Technol.* **16** 1147–51

Baudouy B, Bessette A and Four A 2013 Modeling a horizontal circulation open loop in two-phase helium *Cryogenics* **53** 2–6

Beasley P and Thomas A 2008 Thermal diffusion barrier *GB Patent Specification* 2435918B2

Belton N 2006 Apparatus and method for installing cooling loop tubes on a cooled former *International Patent Application* WO2006/122594A1

Belton N J, Hornsby R and Sorsby P G 2006 Assembly providing a tubular electrical conductor in thermal contact but electrical isolation with at thermal link *US Patent Specification* 20060207266 A1

Berriaud C *et al* 2010 Conductor R&D for the Iseult/Inumac whole body 11.7 T MRI magnet *IEEE Trans. Appl. Supercond.* **20** 1408–11

Bertora F, Borceto A, Viale A and Fabbricatore P 2012 A target field approach to open MRI magnet design *IEEE Trans. Appl. Supercond.* **22** (3) 4905204

Borceto A, Damiani D, Viale A, Bertora F and Marabotto R 2012 Engineering design of a special purpose functional magnetic resonance scanner magnet *Applied Superconductivity Conf. ASC2012 (Portland, OR)* paper 1JA-01

Brechna H 1973 *Superconducting Magnet Systems* (*Springer Technische Physik in Einzeldarstellungen* vol 18) (Berlin: Springer)

Bruker Biospin 2013 website www.bruker-biospin.com/mri-systems.html

Byrne A F, Davies F J, Raynor C, Stautner E W, Steinmeyer F, Albrecht C, Kummeth P, Massek P, Neumüller H-W and Wilson M N 1999 An HTS magnet for whole-body MRI *Proc. EUCAS (Sept. 1999)* pp 1215–8

Byrne A F, Parker N D and Davies F J 2001 MRI magnets *US Patent Specification* 6211676

Cai Z, Clarke R H, Glowacki B A, Nuttall W J and Ward N 2010 Ongoing ascent to the helium production plateau—insights from system dynamics *Resour. Policy* **35** 77–89

CAN Superconductors website 2012 www.can-superconductors.com/products/current-leads/

Cavaliere V *et al* 2008 Normal zone propagation in a MgB$_2$ conduction cooled test magnet *IEEE Trans. Appl. Supercond.* **18** 924

Chandratilleke G R *et al* 1997 Development of multi-loop heat pipes for superconducting magnet applications *Adv. Cryog. Eng.* **43** 1513–9

Chang H-M *et al* 2006 Effect of convection heat transfer on the design of vapor cooled current leads *Cryogenics* **46** 324–32

Chen W E 1997 Cryogen recondensing superconducting magnet *US Patent Specification* 5613367

Chen W E 1998 Cryogen recondensing superconducting magnet *US Patent Specification* 5782095 A

Claudet G and Aymar R 2007 Tore supra and He II cooling of large high field magnets *Adv. Cryog. Eng.* **35** 55–67

Claudet G and Seyfert P 1981 Bath cooling with subcooled superfluid helium *Adv. Cryog. Eng.* **27** 441–9

Cook L P, Klein R, Wong-Ng W, Huang Q, Ribiero R and Canfield P C 2005 Thermodynamics of MgB$_2$ by calorimetry and Knudsen thermogravimetry *IEEE Trans. Appl. Supercond.* **15** 3227–9

Crozier S and Doddrell D M 1997 Compact MRI magnet design by stochastic optimization *J. Magn. Reson.* **127** 233–7

Crozier S, Doddrell D M and Zhao H 2000 Asymmetric superconducting magnets for magnetic resonance imaging *US Patent Specification* 6140900

Crozier S and Liu F 2008 Shielded, asymmetric magnets for use in magnetic resonance imaging *US Patent Specification* 7375528

Dai Y *et al* 2012 Structural design of a whole-body MRI superconducting magnet *IEEE Trans. Appl. Supercond.* **22** 4900404

Daugherty M A, Prenger F C, Hill D D, Daney D E and Woloshun K A 1995 HTS current lead using a composite heat pipe *IEEE Trans. Appl. Supercond.* **5** 773–6

Dietrich R 2005 EAS press release www.bruker.com/products/mr.html

Dietz P, Schmitt F and Hennig J 2011 Gradients in ultra-high field (UHF) MRI *High Field MR Imaging* ed J Hennig and O Speck (Berlin: Springer)

Dixon I R, Markiewicz W D, Brey W W and Shetty K K 2005 Performance of the ultra wide bore 900 MHz NMR magnet at the national high magnetic field laboratory *IEEE Trans. Appl. Supercond.* **15** 1334–7

Doddrell D M and Zhao H 2007 Multi-layer magnet *US Patent Specification* 7212004

Doll D and Tomsic M 2010 Low loss joint for superconducting wire *WO Patent Specification* 2010/088254A1

Dorri B and Laskaris E T 1995 Persistent superconducting switch for cryogen-free MR magnets *IEEE Trans. Appl. Supercond.* **5** 177–80

Dorri B, Laskaris E T and Ogle M 1995a On-shoulder MRI magnet for human brain imaging *US Patent Specification* 5396207

Dorri B, Laskaris E T and Ogle M 1995b Over-shoulder MRI magnet for human brain imaging *US Patent Specification* 5416415

Dresner L 1995 *Stability of Superconductors* (New York: Plenum) chapter 6

Dustmann C-H 1986 Cooling system for indirectly cooled superconducting magnets *US Patent Specification* 4578962

Edeskuty F J and Stewart W F 1996 *Safety in the Handling of Cryogenic Fluids* (*International Cryogenics Monograph Series* vol 1) (New York, London: Plenum)

Elrod J 1963 *Design Handbook for Liquid and Gaseous Helium Handling Equipment* (Washington: US Dept. of Commerce) p 90 AD 410936

Elsner A and Klipping G 1973 Temperature and level control in a liquid helium II cryostat *Adv. Cryog. Eng.* **18** 317–21

Ennis R M, Coffey D M and McGhee R W 1985 Automatic current lead retractor system for superconducting magnets *US Patent Specification* 4544979A

Evaluation Report No. MHRA 03026 2003 *Medicine and Healthcare Products Regulatory Agency (MHRA)* London Imperial College

Fallone B G, Murray B, Rathee S, Stanescu T, Steciw S, Vidakovic S, Blosser E and Tymofichuk D 2009 First MR images obtained during megavoltage photon irradiation from a prototype integrated linac-MR system *Med. Phys.* **36** 2084–8

Faure-Brac G and Grenber A D 1984 Double unsaturated He-II baths for nesting superconducting solenoids producing field greater than 14 T *J. Phys. Colloq.* **45** C1–78

Flükiger R, Hossain M S A and Senatore C 2010 Progress in *in situ* MgB$_2$ wires after cold high pressure densification (CHPD) *IEA ExCo Stockholm* oral presentation

Forth H J 1986 Refrigerator cooling systems for NMR superconducting magnets *Proc. 11th Conf. on Cryogenic Eng.* p 194

François M X and Lottin J C 1979 Control of pressurized superfluid helium II: application to loss analysis *Adv. Cryog. Eng.* **25** 541–55

Garrett M W 1951 Axially symmetric systems for generating and measuring magnetic fields. Part I *J. Appl. Phys.* **22** 1091–107

Garrett M W 1967 Thick cylindrical coil systems for strong magnetic fields with field or gradient homogeneities of the 6th to 20th order *J. Appl. Phys.* **38** 2563–86

Gastineau B *et al* 2012 R3B-GLAD magnet R&D tests program: thermosiphon loop with horizontal section superconducting cable joints at 3600 A, and reduced scale 'coil in its casing' mock-up magnet *IEEE Trans. Appl. Supercond.* **22** (3) 9001004

Gieras J F 2009 *Advancements in Electric Machines* (Berlin: Springer) ISBN 978-1-4020-9006-6

Gilgrass G 2009 Resin-impregnated superconducting magnet coil comprising a cooling layer *US Patent Specification* 7616083B2

Goldacker W *et al* 2002 Development of superconducting and cryogenic technology in the Institute for Technical Physics (ITP) of the Research Center Karlsruhe *Cryogenics* **42** 735–70

Grant P 2012 www.w2agz.com/PMG%20SuperGrid%20Home.htm

Grasso G 2012 *Columbus* private communication (November 2012)

Haid J *et al* 2002a Design analysis of solid nitrogen cooled permanent high-temperature superconducting magnet system *Cryogenics* **42** 617–34

Haid J *et al* 2002b A permanent high-temperature superconducting magnet operated in thermal communication with a mass of solid nitrogen *Cryogenics* **42** 229–44

Hales P, Jones H, Milward S and Harrison S 2005 Investigation into the use of solid nitrogen to create a thermal battery for cooling a portable high-temperature superconducting magnet *Cryogenics* **45** 109–15

Hales P W, Milward S, Harrison S and Jones H 2006 A solid-nitrogen cooled high-temperature superconducting magnet for use in magnetohydrodynamic marine propulsion *IEEE Trans. Appl. Supercond.* **16** 1419–22

Havens T J 1995 Open architecture magnetic resonance imaging passively shimmed superconducting magnet assembly *US Patent Specification* 5389909

Havens T J and Smith R S 1997 Open architecture magnetic resonance imaging superconducting magnet assembly *US Patent Specification* 5696476

Herd K G, Laskaris E T and Thompson P S 1995 A dual refrigerator assembly for cryogen-free superconducting magnet applications *IEEE Trans. Appl. Supercond.* **5** 185–8

Hilal M A 1980 Two-dimensional heat transfer to superfluid helium *Adv. Cryog. Eng.* **25** 358–62

Hofmann A 2003 *Instructions for Using the Numeric Code FZKPTR for the Design of Pulse Tube Coolers* (*FZKA*) vol 6929, p 29

Hofmann A 2012, private communication

Hofmann A and Stautner E W 2005 The development of a pulse tube cooler with more than 1 W at 4.2 K *Adv. Cryog. Eng.* **51** 49–8

Huang X, Thompson P S and Xu M 2006 High temperature superconducting current leads for superconducting magnets *US Patent Specification* 7372273 B2

Hurst G 2010 Design of high field magnets and MR scanners for biomedical use *IV European Conf. of Medical Physics. Advances in High Field Magnetic Resonance Imaging (Udine)*

Hyman S E 2008 A glimmer of light for neuropsychiatric disorders *Nature* **455** 890–3

Hyper Tech Research Inc. 2010 Commercial product application brochure for MgB$_2$ wire

IMV 2012 IMV Medical Information Division, Des Plaines, IL USA www.imvinfo.com

Iwasa Y 2005 Stability and protection of superconducting magnets—a discussion *IEEE Trans. Appl. Supercond.* **15** 1615–20

Iwasa Y, Larbalestier D C, Okada M, Penco R, Sumption M and Xi X 2006 A round table discussion on MgB$_2$ toward a wide market or a niche production—a summary *IEEE Trans. Appl. Supercond.* **16** 1457–64

Jacobs R B 1963 Liquid requirements for the cool-down of cryogenic equipment *Adv. Cryog. Eng* **8** 529–35

Jensen J H 2002 Minimum-volume coil arrangements for generation of uniform magnetic fields *IEEE Trans. Magn.* **38** 3579–88

Johnson V 1960 A compendium of the properties of materials at low temperature: (part 1) properties of fluids *WADD Technical Report* pp 60–56

Juster F P, Berriaud C and Fazilleau P 2010 Quench propagation kinetics within Iseult/INUMAC whole body 11.7 T MRI magnet shielding coils *IEEE Trans. Appl. Supercond.* **20** 1818–22

Kakugawa S, Hino N, Komura A, Kitamura M, Takeshima H and Honmei T 1999 A study on optimal coil configuration in spilt-type superconducting MRI magnet *IEEE Trans. Appl. Supercond.* **9** 366–9

Kalafala A K 1990 A design approach for actively shielded magnetic resonance imaging magnets *IEEE Trans. Magn.* **26** 1181–8

Kan S, Rubeau J P and Sauzade M 1980 A 2.17 helium bath—practical considerations *Internal Report* (Institut d'Electronique Fondamentale Université Paris-Sud, Bâtiment 220-91405 Orsay CEDEX)

Kasthurirengan S and Hofmann A 1998 Response to transient heat load in a helium II loop operated with a self-driven thermomechanical pump *Cryogenics* **38** 833–7

Katsuhiko I, Yoshiaki K and Chen W E 1996 Helium cooling superconducting magnet assembly *Japanese Patent Application* 08279412A

Keilin V E, Kovalev I A, Kruglov S L, Shikov A K, Shutova D I, Vorobjeva A E, Medvedev M I, Potanina L V and Salunin N I 2011 Utilization of large heat capacity substances for improving the stability of superconducting magnets *Cryogenics* **51** 359–65

Kellers J 2003 Trithor *Application note 05*

Kellers J 2008 Trithor, private communication

Kettenbach J *et al* 1999 Computer-based imaging and interventional MRI: applications for neurosurgery *Comput. Med. Imaging Graph.* **23** 245–58

Khandekar S *et al* 2004 *Closed and Open Loop Pulsating Heat Pipes 13th Int. Heat Pipe Conf. (Shanghai)*

Kim W S *et al* 2009 Magnetic field stability of a small YBCO magnet in persistent current mode *IEEE Trans. Appl. Supercond.* **19** 2194

Kodama M 2012 Superconducting joint and method for manufacturing *same US Patent Specification* US20120108435A1

Komarek P 1995 *Hochstromanwendung Supraleitung* (Germany: Teubner)

Kruip M and Mann N 2008 A supported superconducting magnet *International Patent Application* WO2008/032110A1

Kruip M J M 2004 Magnet with improved access *GB Patent Specification* 2355799

Lakrimi M, Brown J, Cetnik P, Wilkinson M, Clapton D, Fair R, Smith K and Noonan P 2007 Low boil-off HTS current leads *IEEE Trans. Appl. Supercond.* **17** 2270–3

Laskaris E T, Ackermann R, Dorri B, Gross D, Herd K and Minas C 1995 A cryogen-free open superconducting magnet for interventional MRI applications *IEEE Trans. Appl. Supercond.* **5** 163–8

Laskaris E T and Ogle M D 1997 Planar superconducting MRI magnet *US Patent Specification* 5677630

Laskaris E T and Ogle M 1998 MRI head magnet *US Patent Specification* 5801609

Laskaris E T and Palmo M A 1999 Open magnet with shielding *US Patent Specification* 5999075

Leach A M, Urbahn J, Anderson D, Clarke N, Skloss T and Ardenkjaer-Larsen J H 2010 A DNP Polarizer designed for clinical use *Proc. Intl. Soc. Mag. Reson. Med.* **18** 3260

Lee P J (ed) 2001 *Engineering Superconductivity* (New York: Wiley–Interscience)

Lehmann W 1978 Safety aspects LHe cryostats and LHe transport containers *Internal Report* 08.01.01P04B Research Center Karlsruhe

Li G Z, Sumption M D, Susner M A, Yang Y, Reddy K M, Rindfleisch M A, Tomsic M J, Thong C J and Collings E W 2012 The critical current density of advanced internal-Mg-diffusion-processed MgB_2 wires *Supercond. Sci. Technol.* **25** 115023

Li X H, Du X J, Bao Q, Kong L Q, Ye L Y and Xiao L Y 2009a Design, development and experiment of a 1.5 T MgB_2 superconducting test magnet *Cryogenics* **49** 286–90

Li X H, Du X J, Qiu M, Ma Y W and Xiao L Y 2007 Design and experimental demonstration of an MgB_2 based 1.5 T MRI test magnet *Physica* C **463–465** 1338–41

Li X *et al* 2009b The development of second generation HTS wire at American superconductor *IEEE Trans. Appl. Supercond.* **19** 3231–5

Liebel H 2011 High-field superconducting magnet systems *High Field MR Imaging* ed J Hennig and O Speck (Berlin: Springer)

Liu Z K, Scholom D G, Li Q and Xi X 2001 Thermodynamics of the Mg-B system, implications for the deposition of thin films *Appl. Phys. Lett.* **78** 3678–80

Lord E 2012 *Superpower* private communication

Lottin J C 1981 He II experimental facilities at Saclay *Adv. Cryog. Eng.* **27** 431–9

Lvovsky Y 2002 Conduction crisis and quench dynamics in cryocooler-cooled HTS magnets *IEEE Trans. Appl. Supercond.* **12** 1565–9

Lvovsky Y 2009 Index loss effect in *n*-value measurements of commercial superconductors *IEEE Trans. Appl. Supercond.* **19** 2313–6

Lvovsky Y and Jarvis P 2005 Superconducting systems for MRI—present solutions and new trends *IEEE Trans. Appl. Supercond.* **15** 1317–25

Lvovsky Y and Jarvis P 2009 Systems, methods and apparatus for specialized magnetic resonance imaging with dual-access conical bore *US Patent Specification* 7498810

Lvovsky Y, Wilcox R E, Kalafala A K and Blecher L 2003 Split type magnetic resonance imaging magnet *US Patent Specification* 6570475

Mardion G B, Claudet G, Seyfert P and Verdier J 1978 Helium II in low-temperature and superconductive magnet engineering *Adv. Cryog. Eng.* **23** 358

Mardion G B and Senet L 1979a A counterflow gas–liquid helium heat exchanger with a copper grid *Cryogenics* **19** 552

Mardion G B and Senet L 1979b An emergency cold valve operating in He II *Cryogenics* **19** 552–3

Marken K 2004 *SPIE Leaflet of Oxford Instruments*

Marken K, Gilgrass G, Holesinger T, Campbell S and Bhattacharya R 2004 Open geometry HTS MRI system *Annu. Peer Supercond. Rev.* www.htspeerreview.com

Matthias B T *et al* 1951 Superconductivity of Nb_3Sn *Phys. Rev.* **95** 1435

Matthias B T *et al* 1965 Superconductivity of Nb_3Ge *Phys. Rev.* **139** A1501–3

McClintock P V E 1978 Liquid level detector for a pumped bath of He II *Cryogenics* **18** 183

McDougall I L 1987 Magnet assemblies for use in magnetic resonance imaging *US Patent Specification* 4689591

McDougall I L, Armstrong A G A M, Begg M C and Longmore D 1992 Magnetic field generating assembly *US Patent Specification* 05162768

McDougall I L and Bird M 1987 Magnet assembly having a plurality of nested coaxial coils *US Patent Specification* 4701736

McDougall I L and Hanley P 2004 Apparatus for magnetic resonance imaging *International Patent Application* WO2004/097443

McDougall I L and Hanley P 2008 Magnetic system for use in magnetic resonance imaging *International Patent Application* WO2009/001084

McDougall I L, Slade R A and Hanley P 2004 Magnet assembly *International Patent Application* WO04029644A1

McDougall I L, Slade R A and Hanley P 2008 Magnet assembly *US Patent Specification* 07355499

Mine S, Hong S, Xu M, Marte J, Buresh S, Stautner E W, Immer C, Laskaris E T and Amm K 2012 Test coil for the development of a compact 3 T MgB_2 magnet *IEEE Trans. Appl. Supercond.* **22** 4400604

Mine S, Xu M, Buresh S, Stautner E W, Immer C, Laskaris E T, Amm K and Grasso G 2013 Second test coil for the development of a compact 3 T MgB_2 magnet *IEEE Trans. Appl. Supercond.* **23** (3) 4601404

Modica M, Angius S, Bertora L, Daminani D, Marabotto M, Nardelli D, Perrella M, Razeti M and Tassisto M 2007 Design, construction and tests of MgB$_2$ coils for the development of a cryogen free magnet *IEEE Trans. Appl. Supercond.* **17** 2196–9

Morawski A, Cetner T, Adamczyk K, Rindfleisch M, Tomsic M, Zaleski A, Gajda D, Diduszko R and Presz A 2011 High enhancement of the J_c in the HyperTech Research Inc. & *ex/in situ* Unipress-made MgB$_2$ wires, obtained by HIP process under high pressure—their application perspectives *Int. Magn. Techn. Conf. MT22 (Marseille)* paper 2GO1-3

Morita H, Tanaka K, Suzuki Y and Okada M 2005 Superconductor connection structure *US Patent Specification* 6921865B2

Morrow G 2000 Progress in MRI magnets *IEEE Trans. Appl. Supercond.* **10** 744–51

Müller W, Roth G, Stautner E W, Turowski P, Lehmann W and Graf F 1992a NMR magnet for highly homogeneous magnetic field—uses at least one superconducting magnetic coil in first chamber of cryostat in deep cooled liquid helium *Patent* DE4039365 A1

Müller W, Roth G, Stautner E W, Turowski P, Lehmann W and Graf F 1992b NMR magnet with superconducting coil in supercooled helium bath—is kept at atmospheric pressure and with temp. of supercooled helium in first cryostat chamber less than 4.2 K with cryostat having at least one further chamber *German Patent Specification* 4039332 A1

Müller W, Roth G, Stautner E W, Turowski P, Lehmann W and Graf F 1993a NMR-magnetsystem mit supraleitender spule in einem low-loss-kryostaten *German Patent Specification* 4039365 C2

Müller W, Roth G, Stautner E W, Turowski P, Lehmann W and Graf F 1993b NMR magnet system with superconducting coil in a helium bath *US Patent Specification* 5220800 A

Musenich R, Sorbi B, Tavilla G, Volpini G, Marabotto R, Modica M and Nardelli D 2008 A MgB$_2$ superferric racetrack magnet *Supercond. Sci. Technol.* **21** 105014

Nagamatsu J, Nakagawa N, Murakami T and Akimitsu J 2001 Superconductivity at 39 K in magnesium diboride *Nature* **410** 63–4

Nakagome H, Kuriyama T and Takahashi M 1992 Superconductive cooling device *Japanese Patent Application* 4116907A2

Nardelli D 2009a Granular Superconducting joint *US Patent Specification* 2009/0264297A1

Nardelli D 2009b Superconducting coil having a granular superconducting junction *Patent* US2009/0264295A1

Natsume K 2011 Heat transfer performance of cryogenic oscillating heat pipes for effective cooling of superconducting magnets *Cryogenics* **51** 309–14

Natsume K *et al* 2012 Development of cryogenic oscillating heat pipe (OHP) as a new device for indirect/conduction cooled superconducting magnets *IEEE Trans. Appl. Supercond.* **22** (3) 4703904

NCD Medical website 2012 www.ncdmedical.com/index.php?content=mri/siemsopenviva

Nenonen J, Ilmoniemi R and Katila T 2000 A 165-channel neuromagnetometer for multimodal brain imaging *Proc. 12th Int. Conf. on Biomagnetism (Espoo)* (Helsinki University of Technology) pp 939–42

Nexans SA 2004 *WAMS* Archamps oral presentation

Noe M 2012 ITP/KIT Jahresbericht

Nunio F, Berriaud C, Bredy P, Schild T, Scola L, Tellier O and Vedrine P 2010 Mechanical design of the Iseult 11.7 T whole body MRI magnet *IEEE Trans. Appl. Supercond.* **20** 760–3

Nutall W J *et al* 2012 *The Future of Helium as a Natural Resource* (London/New York: Routledge)

Ogle M D and Angelo J D 1991 Design optimization method for a ferromagnetically self-shield MR magnet *IEEE Trans. Magn.* **27** 1689–91

Oomen M P, van Hasselt P, Proelss N, Leghissa M, Kruip M, Lister S, Atkins A and Gilgrass G 2006 A pulsed HTS coil cooled by heat pipes as part of a pre-polarizer magnet system *IEEE Trans. Appl. Supercond.* **16** 1519–22

Oomen M P *et al* 2011 Process for producing a connecting structure between two superconductors and structure for connecting two superconductors *Patent* WO2011/039223A1

Orbitmed website 1998 www.orbitmed.com/MRI/SOLD/1998%20Siemens%20Magnetom%20Open%20Viva/Siemens%20Magnetom%20Open%20Viva.htm

Overweg J A and Aldefeld B 2003 Vertical field type MRI apparatus with a conical gradient coil situated in the main magnet *US Patent Specification* 6618606

Paramed website 2012 www.paramedmedicalsystems.com/mr-open-overview.php

Parizh M and Cosmus T 2011 Advances in whole-body MRI magnets *IEEE Trans. Appl. Supercond.* **21** 2104–9

Park D K, Ling J, Rindfleisch M, Voccio J, Hahn S, Bascuñán J, Tomsic M and Iwasa Y 2012 MgB$_2$ for MRI magnets: test coils and superconducting joints results *IEEE Trans. Appl. Supercond.* **22** (3) 4400305

Parkinson B J, Slade R, Mallett M J D and Chamritski V 2013 Development of a cryogen free 1.5 T YBCO HTS magnet for MRI *IEEE Trans. Appl. Supercond.* **23** (3) 4400405

Penco R and Grasso G 2007 Recent development of MgB$_2$-based large scale applications *IEEE Trans. Appl. Supercond.* **17** 2291–4

Pfotenhauer J 2012 Data taken from US Geological Surveys from 1995–2012, private communication

Philips NPB-S&I-Cryo 1985 *Brochure: What You Should Know About Magnet-Cooling in Medical NMR Systems* Building TQIII-4 5600 Eindhoven

PopSci 2009 www.popsci.com/technology/article/2009—11/darpa-wants-freeze-traumatic-brain-injury-battlefield-its-tracks

Prenger F C 1997 *Superconductor Week*

Prenger F C *et al* 1996 Nitrogen heat pipe for cryocooler thermal shunt *Adv. Cryog. Eng.* **41A** 147–54

Pulyer Y M and Hrovat M I 2002 Generation of remote homogeneous magnetic fields *IEEE Trans. Magn.* **38** 1553–63

Raaijmakers A J E, Raaymakers B W and Lagendijk J J 2008 Magnetic-field-induced dose effects in MR-guided radiotherapy systems: dependence on the magnetic field strength *Phys. Med. Biol.* **53** 903–23

Raaymakers B W *et al* 2009 Integrating a 1.5 T MRI scanner with a 6MV accelerator: proof of concept *Phys. Med. Biol.* **54** N229–37

Razeti M, Angius S, Bertora L, Damiani D, Marabotto R, Modica M, Nardelli D, Perrella M and Tassisto M 2008 Construction and operation of cryogen free MgB$_2$ magnets for open MRI Systems *IEEE Trans. Appl. Supercond.* **18** 882–6

Reisch M S 2013 Heavy Demand NMR and other superconductor-based research is a small outlet for helium *Chem. Eng. News* **91** 19

Rieger J 2004 Siemens activities in superconductivity *Workshop on Accelerator Magnet Superconductors* oral presentation

Rosenblum S S, Sheinberg H and Steyert W 1977 A high specific heat for metals for use in superconducting composites *IEEE Trans. Magn.* **MAG-13** 834–5

Roubeau P 1975 *Centre d'Etudes Nucléaires de Saclay* 911991 GIF-SUR-YVETTE, private communication

Sammet S, Koch R M, Aguila F and Knopp M V 2010 Residual magnetism in an MRI Suite after field rampdown: what are the issues and experiences? *J. Magn. Reson. Imaging* **31** 1272–6

Scanlan R M, Malozemoff A P and Larbalestier D C 2004 Superconducting materials for large-scale applications *Proc. IEEE* **92** 1639–54

Schauer W, Specking W and Turowski P 1970 Development of a cryogenic synchrotron magnet with high purity aluminum coils *Internal Report* KFK 219

Schild T, Aubert G, Berriaud C, Bredy P, Juster F P, Meuris C, Nunio F, Quettier L, Rey J M and Vedrine P 2008 The

Iseult/INUMAC whole body 11.7 T MRI magnet design *IEEE Trans. Appl. Supercond.* **18** 904–7

Schild T *et al* 2010 The Iseult/INUMAC whole body 11.7 T MRI magnet R&D program *IEEE Trans. Appl. Supercond.* **20** 702–5

Schild Th, Berriaud C, Dandonneau P A, Girard J P, Hervieu B and Scola L 2011 Toward a new design for a cryogen free MRI magnet *Int. Mag. Techn. Conf. MT22 (Marseille, Aug. 2011)* paper 4DP1-8

Schwarz M 2009 Wärmeleitfähigkeit supraleitender komnpositleiter im temperaturbereich von 4 K bis 300 K *Dissertation* University Karlsruhe

Scott R B 1959 *Cryogenic Engineering* (New York: van Nostrand)

Scott R B, Denton W H and Nicholls C M 1964 *Technology and Uses of Liquid Hydrogen* (Oxford: Pergamon)

Scott T A 1965 Solid and liquid nitrogen *Phys. Rep.* **27** 89–157

Scurlock R G 1988 Cryogenics at the university of Southampton: a review *Cryogenics* **28** 439–66

Scurlock R G 2006 *Low-Loss Storage and Handling of Cryogenic Liquids: The Application of Cryogenic Fluid Dynamics* (Southampton: Kryos Publications) p 81

Sekino M, Ohsaki H, Wada H, Hisatsune T, Ozaki O and Kiyoshi T 2010 Fabrication of an MRI model magnet with an off-centered distribution of homogeneous magnetic field zone *IEEE Trans. Appl. Supercond.* **20** 781–5

Selvamanickam V *et al* 2009 High performance 2G wires: from R&D to pilot-scale manufacturing *IEEE Trans. Appl. Supercond.* **19** 3225–9

Selvamanickam V *et al* 2011 Progress in performance improvement and new research areas for cost reduction of 2G HTS wires *IEEE Trans. Appl. Supercond.* **21** 3049–54

Shintomi T, Makida Y, Hamajima T, Tsuda S, Miyagi D, Takao T, Tanoue N, Ota N, Munakata K and Miwa Y 2012 Design study of SMES system cooled by thermo-siphon with liquid hydrogen for effective use of renewable energy *IEEE Trans. Appl. Supercond.* **22** 5701604

Shvartsman S M, Demeester G D, Patrick J L and Dempsey J F 2011 *International Patent Application* WO2011063342A1

Siemens Allegra brochure 2004 *Siemens Medical Solutions* A91100-M2220-B87–1-7600

Sinanna A *et al* 2010 Field stabilization of the Iseult/INUMAC magnet operating in driven mode *IEEE Trans. Appl. Supercond.* **20** 790–3

Skye H M, Nellis G F and Klein S A 2008 Automatic distributed load temperature control strategies for a rectified continuous flow loop interfaced with a pulse tube cooler *AIP Conf. Proc.* **985** 1683–90

Stables G, Timms K W J and Daniels P D 1999 Refrigerator *US Patent Specification* US5979176

Stautner E W 1984 Quantitative energy balance analysis in cryostats *Annual Physicist's Conf. (Münster)* oral presentation

Stautner E W 2001 Load bearing means in NMR cryostat systems *UK Patent Specification* 2329701

Stautner E W 2002 MRI or NMR systems *US Patent Specification* US6490871

Stautner E W 2007 Cryogenic closed two-phase loop for superconducting HTS magnet cooling *Proc. 14th IHPC. Int. Heat Pipe Conf. at Florianópolis (Brazil)* pp 374–9

Stautner E W 2009 Methods and devices for polarized samples for use in MRI *US Patent Specification* 7631507B2

Stautner E W *et al* 2009a The cryogenics of an MRI demonstrator based on HTS technology with minimum coolant inventory technology *IEEE Trans. Appl. Supercond.* **19** 2297

Stautner E W *et al* 2009b An efficient helium sorption pump in the 1 K temperature range with a small footprint *ICEC: Proc. 22nd Int. Cryogenic Engineering Conf.* **22** 601–6

Stautner E W 2012a *US Patent Applications* 2012/0309630 and 2012/0306492

Stautner E W 2012b *US Patent pending*

Stautner E W 2012c *US Patent Specification* 8238988

Stautner E W 2013a *Patent application* WO2013066558A1

Stautner E W 2013b *US Patent Application* 2013/0109574A1

Stautner E W, Amm K, Laskaris E T, Xu M and Huang X 2007 A new cooling technology for the cooling of HTS magnets *IEEE Trans. Appl. Supercond.* **17** 2196

Stautner E W, Xu M and Mine S 2013 Hydrogen cooling options for MgB_2 based superconducting systems *Cryogenic Engineering Conf. CEC (Anchorage, Alaska)* Preprint 2EPoB3-01

Stautner E W *et al* 2011 The cryogenics of a thermosiphon-cooled HTS MRI magnet—assembly and component testing *IEEE Trans. Appl. Supercond.* **21** 2096–8

Steinmeyer F and Kramer H 2000 Apparatus for delivering current to a cooled electrical device *US Patent* 6112527

Steinmeyer F, Retz P W, White K, Lang A, Stautner E W, Smith P N and Gilgrass G 2002 Towards the invisible cryogenic system for magnetic resonance imaging *Adv. Cryog. Eng.* **47** 1659–66

Stenvall A, Korpela A, Mikkonen R and Grasso G 2006 Stability considerations of multifilamentary MgB_2 tape 2006 *Supercond. Sci. Technol.* **19** 184–9

Sugawara A 2002 Superconductivity: beneficial effect of solid nitrogen on a BSCCO-2223/Ag composite tape subjected to local heating *Physica* C **372–376** 1443–6

Sumitomo Heavy Industries—Product Catalogue, Ltd *Osaki 2-Chome (Tokyo)* p 1

Superpower 2012 private communication

Tachikawa K 2013 Progress of metallic superconductors in Japan *Physica* C **484** 125–9

Takahashi M, Tanaka K, Okada M, Kitaguchi H and Kumakura H 2006 Relaxation of trapped high magnetic field in 100 m long class MgB_2 solenoid coil in persistent current mode operation *IEEE Trans. Appl. Supercond.* **16** 1431

Tenbrink F, Aubele A, Glücklich V, Sailer B and Schlenga K 2010 Verfahren zur Verbindung von zwei oder mehr MgB_2-Supraleiterdrähten über einen Presskörper aus HTS-Pulver und supraleitende Verbindungsstelle von zwei oder mehr dieser Drähte *German Patent Specification* 102009010011B3

Terao Y and Sekino M 2012 Electromagnetic design of 10 MW class fully superconducting wind turbine generators *IEEE Trans. Appl. Supercond.* **22** (3) 5201904

Tomsic M, Rindfleisch M, Yue J, McFadden K, Phillips J, Sumption M D, Bhatia M, Bohnenstiehl S and Collings E W 2007 Overview of MgB_2 superconductor applications *Int. J. Appl. Ceram. Technol.* **4** 250–9

Tomsic M J 2004 Method for manufacturing MgB_2 intermetallic superconductor wires *US Patent Specification* 6687975

Turowski P and Schneider Th 1989 A 20 T superconducting magnet system *Physica* B **155** 87–90

Turowski P and Schneider Th 1990 Design and operation of a 20 T superconducting magnet system and future prospects *Physica* B **164** 3–8

Turowski P *et al* 1980 Die Entwicklung eines supraleitenden 13.5 T-magnetsystems für Mößbauer-Experimente *KfK Report* 3093

UCSF Website 2010 www.ucsf.edu/news/2010/11/5846/new-prostate-cancer-imaging-shows-real-time-tumor-metabolism

Urbahn J *et al* 2009 A closed cycle helium sorption pump system and its use in making hyperpolarized compounds for MRI imaging *ICEC: Proc. 22nd Int. Cryogenic Engineering Conf.* **22** 589–94

van Hasselt P 2006 Superconducting device having cryosystem and superconducting switch *US Patent Specification* 2006135370 A1

van Hasselt P 2007 Superconductor device having superconductive magnet and refrigeration unit *US Patent Specification* 7260941

van Oort J M, Laskaris E T, Thompson P S, Dorri B and Herd K G 1998 A cryogen-free 0.5 T MRI magnet for head imaging *Adv. Cryog. Eng.* **43** 139–47

van Sciver S W 1978 Kapitza conductance of aluminum and heat transport from a flat surface through a large-diameter tube to saturated helium II *Adv. Cryog. Eng.* **23** 340–8

van Sciver S W 2002 Developments in He II heat transfer and applications to superconducting magnets *Adv. Cryog. Eng.* **27** 375–98

van Sciver S W 2012 *Helium Cryogenics* (*International Cryogenic Monograph Series*) (New York: Springer)

Vedrine P *et al* 2010 Iseult/INUMAC whole body 11.7 T MRI magnet status *IEEE Trans. Appl. Supercond.* **20** 696–701

Vedrine P *et al* 2012 Latest progress on the Iseult/INUMAC whole body 11.7 T MRI magnet *IEEE Trans. Appl. Supercond.* **22** 4400804

Vermilyea M E and Dorri B 1994 Demountable conduction cooled current leads for refrigerated superconducting magnets *US Patent Specification* 5317296A

ViewRay 2010 Images from web site www.viewray.com—product overview

Wada H, Sekino M, Ohsaki H, Hisatsune T, Ikehira H and Kiyoshi T 2010 Prospect of high-filed MRI *IEEE Trans. Appl. Supercond.* **20** 115–22

Wang C 2009 A helium re-liquefier for recovering and liquefying helium vapor from cryostat *AIP Conf. Proc.* **1218** 687–94 and Wang C (private communication)

Wang Q *et al* 2010 Development of conduction cooled superconducting magnet for baby imaging *IEEE Trans. Appl. Supercond.* **20** 726–31

Wang Q *et al* 2012 A superconducting magnet system for whole-body metabolism imaging *IEEE Trans. Appl. Supercond.* **22** 4400905

Warner R 2008 Advances in high field magnets *ISMRM Workshop on High-Field Systems and Applications (Rome, 15–17 Oct. 2008)*

Warner R 2010 MRI Magnet Design 2020 *ISMRM-2010 (Stockholm, May 2010)*

Westphal M 2012 Bruker, private communication

White K and Steinmeyer F 2005 Cryogenic assembly *US Patent Specification* 20050204751 A1

Wilks J 1967 *The Properties of Liquid and Solid Helium* (New York: Oxford University Press)

Williams J E 1984 Superconducting magnets for MRI *IEEE Trans. Nucl. Sci.* **31** 994–1005

Williams J E *et al* 1981 Magnet system of the 500 MHz NMR spectrometer at the Francis Bitter National Laboratory: I. Design and development of the magnet *Rev. Sci. Instrum.* **52** 649–56

Wilson M 1982 *Superconducting Magnets* 2nd edn (Oxford: Oxford Science Publications) p 91

Wilson M N 2012 100 years of superconductivity and 50 years of superconducting magnets *IEEE Trans. Appl. Supercond.* **22** (3) 3800212

Woolf L D 1987 High heat capacity composites for a superconductor *US Patent Specification* 4647888

Xie Y Y *et al* 2009 Second-generation HTS conductor design and engineering for electrical power applications *IEEE Trans. Appl. Supercond.* **19** 3009

Xu H, Conolly S M, Scott G C and Macovski A 2000 Homogeneous magnet design using linear programming *IEEE Trans. Magn.* **36** 476–83

Xu M, Laskaris E T, Budesheim E, Conte G, Huang X, Stautner E W and Amm K 2010 BSCCO MRI magnet winding and testing at LN2 temperature *IEEE Trans. Appl. Supercond.* **20** 769–72

Yao W, Bascuñán J, Hahn S and Iwasa Y 2009 A superconducting joint technique for MgB_2 round wires *IEEE Trans. Appl. Supercond.* **19** 2261

Yao W, Bascuñán J, Kim W-S, Hahn S, Lee H and Iwasa Y 2008 A solid nitrogen cooled MgB_2 demonstration coil for MRI applications *IEEE Trans. Appl. Supercond.* **18** 912–5

Ye L, Majoros M, Campbell A M, Coombs T, Harrison S, Sargent P, Haslett M and Husband M 2007 MgB_2 sample tests for possible applications of superconducting fault current limiters *IEEE Trans. Appl. Supercond.* **17** 2826–9

Yoshito G, Ichiro T, Keiji O and Hideki N 1993 Superconducting device *Patent* JP5003120 A

Zhang T, deBock P, Stautner E W, Deng T and Immer C 2012 Demonstration of liquid nitrogen wicking using a multi-layer metallic wire cloth laminate *Cryogenics* **52** 301–5